Magnetic skyrmions in in-plane magnets

Stability, current dynamics and excitations

Doctoral thesis

Venkata Krishna Bharadwaj

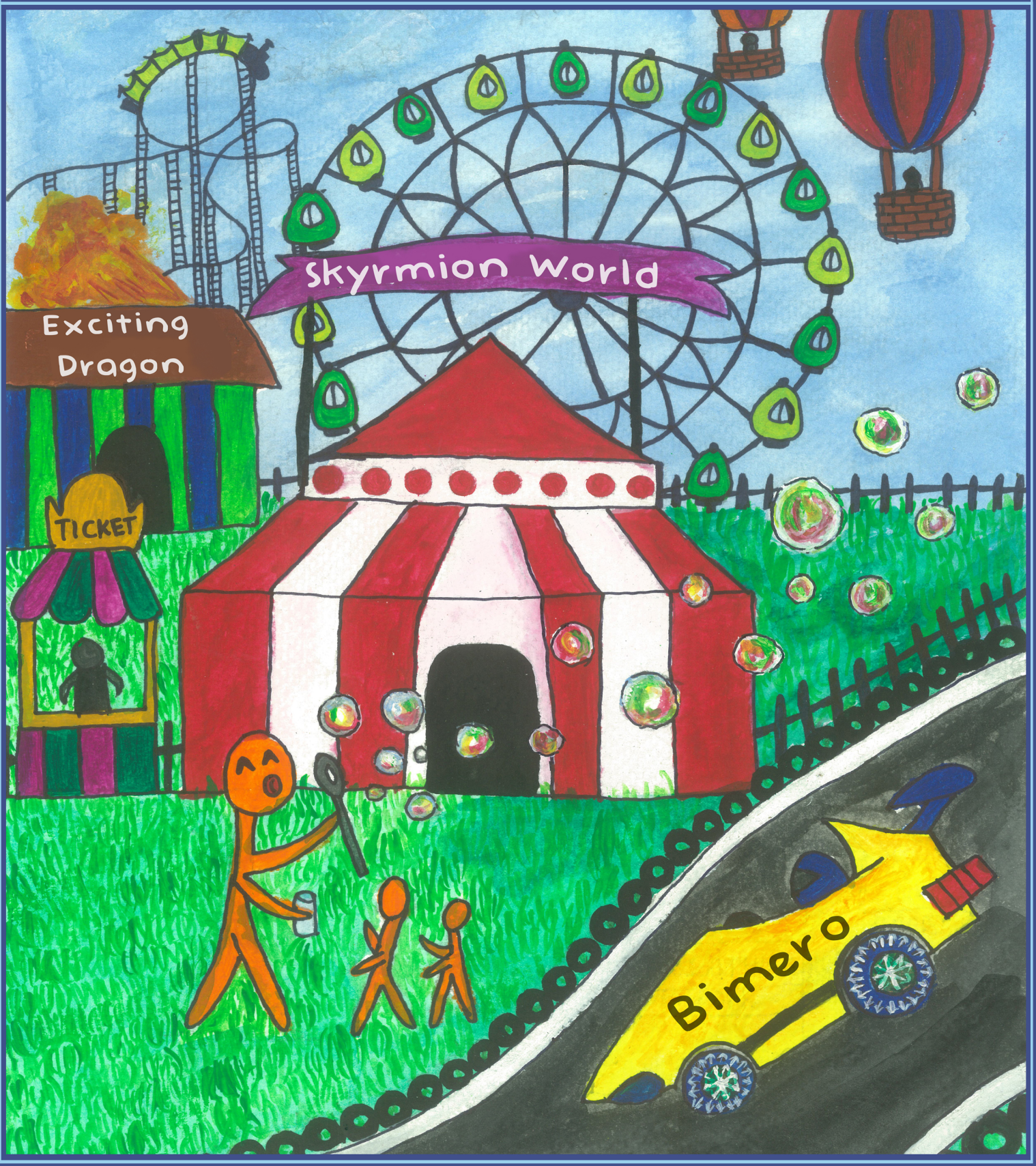

Magnetic skyrmions in in-plane magnets

Stability, current-induced dynamics and excitations

Dissertation

zur Erlangung des Grades
"Doktor
der Naturwissenschaften"
am Fachbereich Physik, Mathematik und Informatik
der Johannes Gutenberg-Universität
in Mainz

Venkata Krishna Bharadwaj

Mainz, den November 6, 2023

ಹುಲ್ಲಾಗು ಬೆಟ್ಟದಡಿ, ಮನೆಗೆ ಮಲ್ಲಿಗೆಯಾಗು |
ಕಲ್ಲಾಗು ಕಷ್ಟಗಳ ಮಳೆಯ ವಿಧಿ ಸುರಿಯೆ ||
ಬೆಲ್ಲ ಸಕ್ಕರೆಯಾಗು ದೀನ ದುರ್ಬಲರಿಂಗೆ |
ಎಲ್ಲರೊಳಗೊಂದಾಗು ಮಂಕುತಿಮ್ಮ ||

"*Be a (gentle) blade of grass at the foot of mountain, and jasmine flower at home,*
Be (strong) like a rock when fate pours (torrential) rains of difficulties on you,
Be sweet like sugar and jaggery to the poor and weak,
Be one among all, Mankuthimma."

- D. V. Gundappa
  (Kannada poet)

Abstract

The invention of transistors and microchips has revolutionized information storage. Technological progress has led to the miniaturization of microelectronics, resulting in higher energy consumption and heat production, which presents difficulties for microprocessor manufacturers. Therefore, there is a need for new computing and information technology approaches. Spintronics, which utilizes both electron spin and charge, shows great promise in overcoming the limitations of semiconductor technology and enhancing data storage capabilities. It offers increased functionality to devices and addresses current data storage constraints. An encouraging prospect among these options is the use of domain walls in racetrack memory device, enabling efficient and speedy storage of data in a non-volatile manner. Nonetheless, they encounter challenges such as the pinning of domain walls at the edges and the need for a high current density to relocate them.

Skyrmionics, a new protagonist in the field of spintronics, has recently gained significant attention. Magnetic skyrmions, nanoscale windings of the spin configuration in certain magnetic materials, exhibit nontrivial topology and have the potential to replace domain walls in racetrack memories. Room-temperature observations have fueled research into skyrmion-like quasiparticles, showing lower current-driven motion (compared to domain walls) mediated by both spin-transfer and spin-orbit torques. This offers potential for racetrack memory devices, where skyrmions encode the units of information. However, the topological nature of ferromagnetic skyrmions leads to the skyrmion Hall effect, which pushes them towards the racetrack's edge, thereby causing data loss. Efficient skyrmion-based spintronic memories require the suppression of the skyrmion Hall effect and, in turn, to explore other topological spin textures.

Recent studies have indicated the presence of skyrmion analogues known

as in-plane skyrmions or bimerons in chiral magnet thin films with in-plane anisotropy. This thesis focuses on investigating these in-plane skyrmions in thin-film in-plane magnets. A minimal in-plane micromagnetic model is considered to assess their stability, followed by analyzing the symmetries of the Dzyaloshinskii-Moriya interaction and suggesting potential materials to host in-plane skyrmions. Furthermore, we investigate the stability of in-plane skyrmions in the monoclinic system with mirror symmetry. The thesis also explores two methods for generating in-plane skyrmions: creating magnetic bubbles through geometric constriction and releasing skyrmions from magnetic inhomogeneities. Additionally, a proof-of-concept for a racetrack utilizing in-plane skyrmions is presented. Lastly, the thesis examines the current-driven motion of in-plane skyrmions, highlighting the advantages they offer compared to Néel skyrmions through Thiele analysis and micromagnetic simulations.

Kurzzusammenfassung

Die Erfindung von Transistoren und Mikrochips hat die Informationsspeicherung revolutioniert. Unser Leben ist mittlerweile mit der digitalen Welt verschmolzen. Jedoch hat der technologische Fortschritt zur Miniaturisierung der Mikroelektronik geführt, was einen höheren Energieverbrauch und eine höhere Wärmeentwicklung zur Folge hat. Dies stellt die Hersteller von Mikroprozessoren vor Schwierigkeiten. Daher ist man auf der Suche nach neuen Ansätzen in der Computer- und Informationstechnologie. Die Spintronik, bei der sowohl der Elektronenspin als auch die elektrische Ladung genutzt werden, ist ein vielversprechender Ansatz, um die Grenzen der Halbleitertechnologie zu überwinden und die Datenspeicherung zu verbessern. Sie bietet den Geräten eine höhere Funktionalität und adressiert die derzeitigen Beschränkungen bei der Datenspeicherung.

Die Skyrmionik, ein Teilgebiet der Spintronik, hat in letzter Zeit große Aufmerksamkeit erlangt. Magnetische Skyrmionen, Windungen in der Spinkonfiguration bestimmter magnetischer Materialien im Nanometerbereich, weisen eine nicht-triviale Topologie auf und haben das Potenzial, die kleinsten magnetischen Texturen zu sein. Experimente, durchgeführt bei Raumtemperatur, haben die Erforschung skyrmionartiger Quasiteilchen vorangetrieben und gezeigt, dass sie sich im Vergleich zu Domänenwänden mit geringeren elektrischen Strömen bewegen, indem sie Spindreh- und Spinbahnmomente nutzen. Dies bietet die Möglichkeit, Informationen in Form von Skyrmionen als einsen und nullen zu kodieren. Die topologische Beschaffenheit der Skyrmionen führt jedoch zum Skyrmion-Hall-Effekt, der sie an den Rand der Leiterbahn drängt und zu Datenverlust führen kann. Ein effizienter spintronischer Speicher auf Skyrmionenbasis erfordert die Unterdrückung von Skyrmion-Hall-Effektes. Daher benötigt es die Erforschung alternativer topologischer Spinstrukturen.

Jüngste Studien haben die Existenz von besonderen Skyrmion, die als in-plane-

Skyrmionen (in der Ebene) oder Bimeronen bekannt sind, in chiralen Magnetdünnschichten mit in-plane-Anisotropie gezeigt. Diese Arbeit konzentriert sich auf die Untersuchung dieser in-plane-Skyrmionen in Dünnschichtfilmen von in-plane-Magneten. Ein minimales in-plane mikromagnetisches Modell wird verwendet, um ihre Stabilität zu bewerten, gefolgt von einer Analyse der Symmetrien der Dzyaloshinskii-Moriya-Wechselwirkung und Vorschlägen für potentielle Materialien, die in-plane-Skyrmionen beherbergen können. Darüber hinaus wird in der Studie die Stabilität von in-plane Skyrmionen im monoklinen System mit Spiegelsymmetrie untersucht. Des Weiteren werden in dieser Arbeit zwei Methoden zur Erzeugung von in-plane-Skyrmionen untersucht: die Erzeugung von magnetischen Blasen durch geometrische Einschnürung und die Freisetzung von Skyrmionen aus magnetischen Inhomogenitäten. Zusätzlich wird ein konzeptioneller Beweiß für eine Leiterbahn mit in-plane-Skyrmionen vorgestellt. Schließlich wird in dieser Arbeit die stromgetriebene Bewegung von Skyrmionen in der Ebene untersucht, wobei ihre Vorteile im Vergleich zu Néel-Skyrmionen durch Thiele-Analyse und mikromagnetische Simulationen hervorgehoben werden. [1]

[1] DeepL was utilized to assist in translating the English version of the Abstract into German. [1]

Contents

Chapter 1

Introduction

> *Greek philosopher Socrates believed that written words forced a reader to follow an argument rather than participate in one, and, hence was a proponent of not recording his thoughts. He was unsettled by the fact that an author's words could be misconstrued and never be argued out of position after his passing. Ironically, his philosophy is known today only because his friend Plato took it upon himself to write down his words on parchment scrolls for us to read today. [2]*

Preserving information and passing it on to future generations has been a challenge since time immemorial. The evolution of the transfer of information and knowledge from oral tradition and cave paintings to written form was one the most significant turning point in human history. Since the invention of paper in China around the 1st century, books were the main source of information storage until the era of transistors. Only in the late 21st century, when the world entered the digital age, did we achieve another milestone in the storage of information which has paved the way for the creation and consumption of a lot of data.

1.1 Tsunami of data

The invention of transistors and microchips has changed our capability to store information to an unprecedented limit [3]. Today our lives are deeply entrenched in the digital universe. With the advent of the internet, social media,

robotics, virtual reality, online video streaming, and artificial intelligence, we have been hit with a tsunami of data. In the last decade (2010-2020), we have seen an exponential growth with a factor of six times in the amount of data produced. It was estimated that the total amount of data generated at the dawn of 2020 alone was ∼64 zettabytes, which will only keep growing to ∼180 zettabytes in the next half-decade [4, 5]. Fig. 1.1 illustrates the cumulative data usage from 2010 to 2018, as well as the projected (marked by *) total amount of data generated, captured, copied, and consumed worldwide until 2025.

Covid-19: Big data redefined

We cannot overlook the effects of the 2020-21 global pandemic on the digital world. The sudden surge in the number of people working from home as a result of the COVID-19 pandemic has resulted in a staggering consumption of data in the form of video communications, downloaded and streamed video

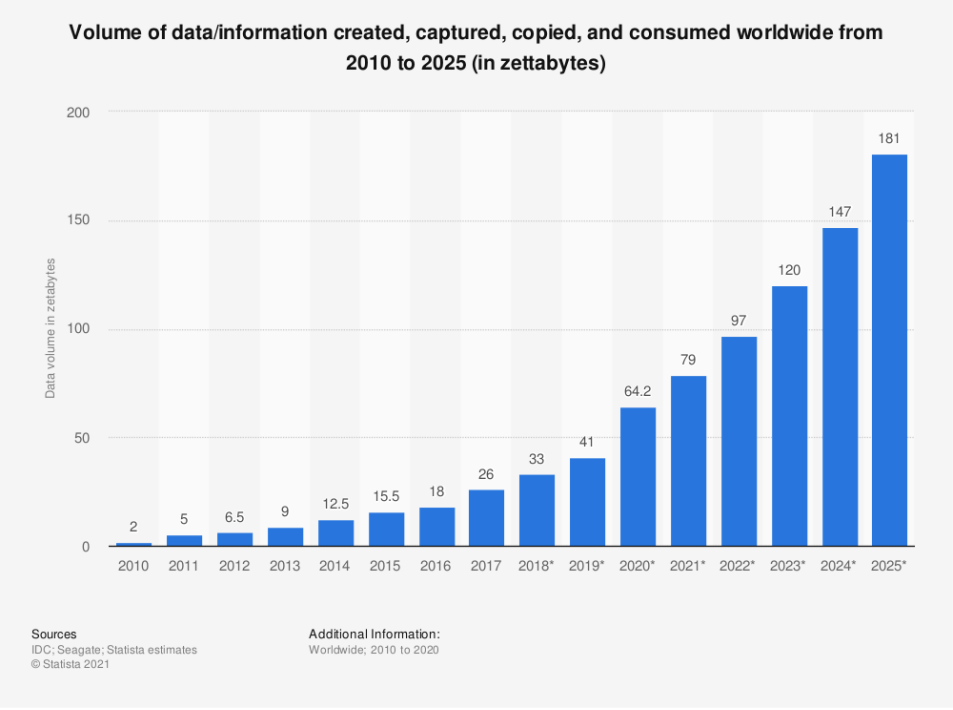

Figure 1.1: The total estimate of the amount of data created, captured, copied, and consumed globally from 2010-2020. This figure was taken from [5].

services like Netflix, YouTube, Amazon, etc., social media, and online email and message services. According to a recent update from International Data Corporation [6], it is estimated that more data will be generated over the next three years than in the last thirty years.

1.2 Charge-based memory technology

The shift in information storage from analog to digital media has changed the way we perceive, store, and, most importantly, manipulate data. With the ever-expanding demand for the Internet of Things (IoT) over the last decade, *data has become the new oil* [7].

Most of these modern technologies are electronic, which means that whenever you turn on an electronic device like your smartphone, TV, car, or laptop, the electrons start moving through the tiny transistors in the integrated circuits (IC) of your devices. The prominent types of memory microelectronic devices in the market today are dynamic random access memory (DRAM), static RAM (SRAM), and flash memory. These types of memory cells store data in a charge state. As the technology evolved over the last few decades, the semiconductor industry continued to follow Moore's Law, which predicted that the number of transistors on an IC would double about every two years. Thus we were able to pack more and more transistors into IC systems, thereby producing increasingly powerful microprocessors that respond to the demands of the digital world. Quite recently, TSMC (Taiwan Semiconductor Manufacturing Company, Limited), the world's leading manufacturer of semiconductor chips, produced chips (M1 Max [8]) for Apple Inc containing 57 billion transistors using 5nm fabrication technology [9, 10].

The elephant in the room

The down-scaling of microelectronics has resulted in a very sharp increase in energy consumption and heat generation, which has become an enormous thorn for microprocessor manufacturers [11–13]. It was mentioned by *Fortune* that when the music video "Despacito" hit the Internet, it earned a record by having 5 billion views on YouTube in April 2018 [14]. In doing so, it burned as much energy as 40,000 U.S. homes use in a year. By 2025, according to

Swedish researcher Anders Andrae [15, 16], communications technology alone could consume around one-fifth of global electricity. Fig. 1.1 illustrates the share of global electricity consumption by Internet, communications technology (ICT). This over-consumption of electricity is increasing the energy footprint of the digital economy and thus thwarting any effort to meet climate change goals.

Even though conventional electronics is based on the movement of electrons and mainly use their property of electric charge; they bear yet another intrinsic quantum-physical property called "spin," which can be used to store, encode, and transmit information. Augmenting the role of charge with the spin degree of freedom offers devices greater functionality and a further step towards solving the current limits of data storage. Finding successors to today's semiconductor silicon microchips takes years of research and exploration into solid-state physics and materials sciences.

1.3 Spintronics: Electronics of the future

Currently, the field of spintronics is one of the most promising candidates for solving many of the future challenges and limitations of semiconductor technology [17–20]. Spintronics, also known as spin-electronics, is the study of spin property of electrons and their associated magnetic moment in solid-state physics. Over the last two decades, there has been a tremendous amount of interest in investigating potential applications in memory storage devices that leverage spin properties rather than or in addition to charge degrees of freedom.

The field of spintronics has emerged from discoveries and innovations of the last century. F. Mott proposed the concept of spin dependent conduction in 1936 [21] which was later confirmed by P. Tedrow and R. Meservey using tunneling experiments between ferromagnetic metals and superconductor [22, 23]. A breakthrough in spintronics occurred with the discovery of the giant magneto-resistant effect (GMR) in 1988 by two physicists A. Fert and P. A. Grünberg at the same time [24, 25], who were awarded the 2007 Nobel Prize in Physics for this discovery [26–28]. The GMR effect refers to a change in the resistance of two ferromagnetic layers (FM) separated by a non-

magnetic spacer as their relative orientation of the magnetization changes. Fert and Grünberg found that the resistance is lower in the case of the magnetization in the two FM layers being parallel than when they are antiparallel. This increased resistance means that GMR can be used to make extremely sensitive magnetic sensors. This new physics has had an enormous impact on our technology since this led to miniaturizing hard disk drives (HDDs) with smaller bits. As such, GMR soon caught the attention of researchers and industry alike. Grünberg, who recognized the potential of this phenomenon, said [28]:

> *At the time of the discovery of GMR, it was well known that leading computer companies planned to develop Anisotropic magnetoresistance (AMR) so it could be used for read heads in hard disk drives (HDDs). The comparison between AMR and the new effect (later, the term GMR was widely accepted) encouraged us to file a patent for using GMR in HDD.*
>
> Nobel Lecture 2007, Peter A. Grünberg

A few years later, Stuart Parkin, a physicist at IBM, demonstrated that the GMR effect could be achieved using much faster, cheaper methods that paved the way for the commercialization of this physics phenomenon. Parkin discovered the existence of GMR in multilayers of Fe/Cr, Co/Ru, and Co/Cr, which were prepared using a simpler technique of sputtering deposition which can be scaled for industrial purposes [29, 30]. By 1996, the technology of GMR heads for the HDDs had become standard use across the electronics industry.

Another milestone in spintronics came with the advent of tunnel magnetoresistance (TMR) experiments. TMR refers to a case of two FM layers separated by an insulator, also known as a magnetic tunnel junction (MTJ). Even though the TMR effect was first reported in 1975 by Jullière [31], it was not until 1995 that it was verified by Moodera and Miyasaki's groups [32, 33]. The TMR effect was discovered to be much larger than the previously discovered GMR, thus improving the sensitivity of sensor heads and reducing the power consumption in HDDs, which is used widely in today's memory storage devices [34]. The first commercial application of TMR heads was introduced

by Seagate in 2004 [35, 36]. Thus, by being able to reap the fruits of spintronics applications early on, it has given enormous potential to new directions of electronics.

As HDD began to become the industry norm for non-volatile storage, a novel idea for data storage was proposed by Stuart Parkin called Racetrack memory [37]. It contains a series of magnetic domains, separated by domain walls in a nanowire, and data is encoded in those tiny domains that can be read by magnetic sensors [38, 39], (see Fig 1.2). This principle of moving magnetic domain walls by means of current pulses was first proposed in 1978 by Berger and demonstrated in the Permalloy wires by Parkin's group. In contrast to HDD, the racetrack memory device does not need a mechanical arm to read and write information; instead, the bits of information are moved back and forth along the nanowire like a shift register. Moreover, the writing speed is of the order of nanoseconds as opposed to the millisecond on a traditional hard disk, thus allowing for high-speed (by six orders of magnitude) read/write access to massive amounts of information.

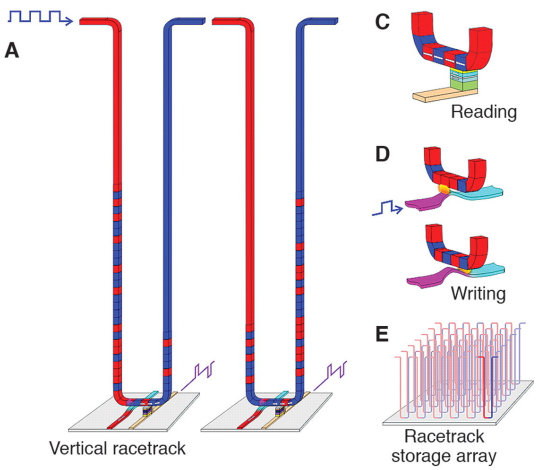

Figure 1.2: The domain wall racetrack memory proposed by Stuart Parkin (only a part of the figure shown from Ref [39]). A) A U-shaped nanowire divided into a sequence of magnetic domains. C) Reading function achieved by a TMR of a MTJ attached to the racetrack device. D) The writing element to write new data into the device, which can be accomplished by various schemes. E) Using the 3D arrangement of racetracks on a memory chip to achieve high-density storage devices.

1.4 Skyrmionics: A new protagonist

In recent years a subbranch of spintronics called skyrmionics has emerged and attracted immense interest from researchers. A magnetic skyrmion is a localized, chiral spin texture with the whirling of the magnetization, as depicted in Fig 1.3(a). The magnetization varies smoothly along the radial direction, with magnetization pointing in $-\hat{z}$ direction at the center to $+\hat{z}$ direction far away from the skyrmion [40].

These magnetic skyrmions have topological stability, as in, how a doughnut cannot be transformed into a solid sphere smoothly, and these textures cannot be deformed smoothly into any of the other topologically trivial ground states (ferromagnetic, helical, conical). Even though skyrmions were predicted three decades ago [41, 42], they began receiving attention since their first observation at low temperatures in 2009 in bulk materials [40]. Recently they were also observed at room temperatures [43–45] which gave a boost to research into the field of skyrmion-like quasiparticles, viz. antiskyrmions [46–48], antiferromagnetic skyrmions [49–51], biskyrmions [52, 53], skyrmion bags [54], skyrmionium, merons [55, 56], and antiferromagnetic merons [57, 58].

Experimental investigations in the last decade have revealed that the size of the skyrmions can range from 1 nm up to 100 nm [59, 60]. It was shown that these magnetic skyrmions could be moved with much lower electric currents than domain walls [61] using spin transfer and spin-orbit torques. Later theoretical and experimental studies demonstrated numerous ways for the creation, manipulation, and annihilation of isolated skyrmions stabilized by Dzyaloshinskii-Moriya interactions in perpendicularly magnetized thin magnetic films [44, 62–69]. Later, a skyrmion race track memory device was proposed [70], where skyrmions are used to encode bits of information with the presence or absence of a skyrmion representing 1 or 0, respectively. These bits of information (skyrmions) can be moved along the racetrack by applying a spin-polarized current on the nano strip [70–73](see Fig 1.3(c)).

These exciting findings over the last decade have hinted at skyrmions overcoming the drawbacks of domain walls and being a high potential for low-

energy, nonvolatile, ultra-dense memory devices [72, 74–76]. In addition to the stability, the topological property of skyrmions leads to interesting effects with current-driven dynamics, i.e. Skyrmion Hall effect (SkHE)[73, 77]. When driven by currents, in addition to motion along the direction of current, SkHE induces an additional transverse deflection of skyrmions. As a result, when skyrmions are driven across a race track using currents, they are also pushed toward the edge of the racetrack leading to a loss of data. Hence, to be able to efficiently use skyrmions for spintronic memory applications, finding ways to suppress SkHE is essential, as is looking beyond the conventional skyrmions to alternate topological spin textures and contrasting their current-driven behaviour with those of skyrmions.

Recent reports have suggested the existence of skyrmion analogues in chiral magnet thin films with in-plane anisotropy [78–81]. In-plane skyrmions, also known as bimerons, are composed of two merons which can be attained by rotating the Néel skyrmion by $\pi/2$ along $\hat{y}$ as depicted in Fig 1.3(b). Now, in contrast to the Néel skyrmions, it is the in-plane component of the magnetization which is radially symmetric about its center, with magnetization at the center being aligned along the in-plane anisotropy direction and along opposite direction at the outer region of the in-plane skyrmion. The primary focus of this thesis is on in-plane skyrmions and their nucleation, stability in materials, current-driven dynamics, and excitations.

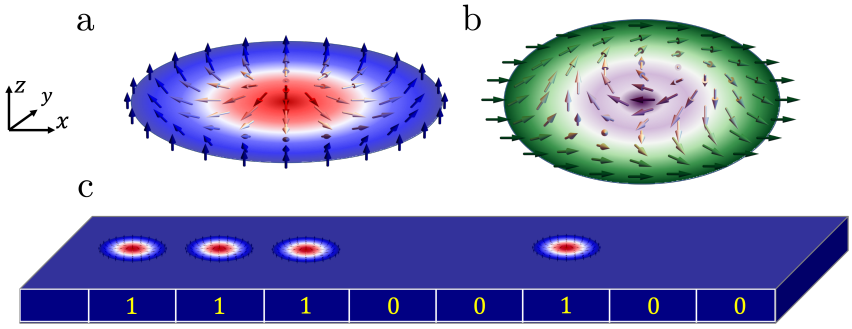

Figure 1.3: Schematic representation of magnetic skyrmions. a) A Néel skyrmion b) In-plane skyrmion. c) Schematic of a skyrmion racetrack memory device. The binary information is encoded on a ferromagnetic thin track in the form of presence or absence of magnetic skyrmions.

1.5 Outline of the thesis

The thesis comprises five primary chapters, a concluding chapter, and an appendix. Chapters 3, 4, and 5 present the key findings of the research work, which have been published [82]. The manuscript is organized as follows:

Chapter 2: Fundamental theoretical models and numerical methods — The chapter starts with an introduction to micromagnetism, which provides the framework for the rest of the work described in the thesis. A brief primer on the different interactions contributing to the energy functional (Sec. 2.1.1) is followed by an introduction to magnetization dynamics described by the Landau-Lifshitz-Gilbert equation. The first part ends with a description of current-induced magnetization dynamics (Sec. 2.2). The second part of the chapter focuses on introducing magnetic skyrmions, starting with a brief theoretical description of skyrmions (Sec.2.3), followed by recent experimental observations (2.3.2). The chapter concludes with the current-induced dynamics of skyrmions.

Chapter 3: Stability of in-plane skyrmions — This chapter presents the study of magnetic skyrmions in thin-film in-plane magnets. The numerical results explaining the structure of in-plane skyrmions and the effect of stray fields are shown (Sec. 3.3). A biaxial anisotropy model is used to analytically model the complex effect of stray fields in in-plane magnets (Sec. 3.3). This is followed by the description of symmetries of the Dzyaloshinskii-Moriya interaction and a proposal for potential material candidates to host in-plane skyrmions (Sec. 3.6). Finally, the stability of the in-plane skyrmions in the monoclinic system with mirror symmetry is analysed, and a phase diagram is provided (Sec. 3.7).

Chapter 4: Production of in-plane skyrmions — This chapter describes two different mechanisms for the production of in-plane skyrmions, viz. blowing magnetic bubbles through a geometric constriction (Sec. 4.2) and shedding skyrmions from a magnetic inhomogeneity (Sec. 4.3). Recent experimental studies about the production of Néel skyrmions by means of the first method are discussed, and its implementation to produce in-plane skyrmions in thin-film in-plane magnets is shown via micromagnetic simulations. The second mechanism is discussed as well, and a proof of concept for the racetrack

of in-plane skyrmions is presented (Sec. 4.3.2).

Chapter 5: Current-driven dynamics of in-plane skyrmions — This chapter contains the study of the current-driven motion of in-plane skyrmions in an ultra-thin Pt/Co/MgO film at room temperature. The experimental results, including the observation of the current-driven skyrmion motion and characterisation of the magnetic film properties, are first presented. These results are then discussed and interpreted in the light of the collective variable approach (Thiele equation) and micromagnetic simulations.

Summary and perspectives — In this final chapter the main findings of this thesis, presented in the three previous chapters, are briefly summarised. Future prospects of this work are also discussed.

Chapter 2

Fundamental theoretical models and numerical methods

This chapter introduces relevant fundamental concepts required to understand the work done in this thesis. We shall start by introducing the micromagnetic framework and an overview of the different magnetic energy contributions within this formalism. Different types of chiral magnetic ground states in the ferromagnet will be described with a focus on the main objective of the thesis, magnetic skyrmions. Furthermore, we will describe the Landau-Lifshitz-Gilbert equation (LLG), which represents the dynamics of the magnetization at time scales of an order greater than a nanosecond. The LLG will then be extended to include the effects of electrical currents and their driven dynamics of magnetic textures.

2.1 Micromagnetic framework

The phenomenon of magnetism can be studied at different length scales ranging from the Angstrom scale, where the magnetic moments of electron spins play a role, all the way to the formation of magnetic domains and hysteresis phenomena on the macroscopic scale. It is important to choose the time and length scale that is significant for the phenomenon under consideration. The common paradigms for the theoretical description of magnetic skyrmions are atomistic and micromagnetic models. The atomistic simulations cannot be efficiently scaled to systems larger than a few nanometers, and consequently, we shall use the micromagnetic model throughout this thesis to study the in-plane skyrmions and their dynamics. Micromagnetic theory describes phenomena in the range of a few nanometers to micrometers length scale such that it is able to explain phenomena between the range of discrete atomistic spins to magnetic domains. It has been successful in explaining the formation and shape of domain walls (DW), magnetic skyrmions, and hopfions, which makes it suitable for the present work.

The key assumption of micromagnetism is that the order parameter of the magnetic material varies smoothly in space on length scales larger than that of inter-atomic distances. In ferromagnets, magnetization being the order parameter, it can be described by a smoothly varying vector field $\boldsymbol{M}(\boldsymbol{r}, \boldsymbol{t})$, which makes the theory a continuum theory of magnetization. At temperatures well below the Curie point, the length of the magnetization vector is fixed and is equal to the saturation magnetization M_s. Hence, we can introduce the normalized magnetization field $\boldsymbol{m}(\boldsymbol{r}, \boldsymbol{t})$, which indicates the local direction of the magnetization,

$$\boldsymbol{M}(\boldsymbol{r}, \boldsymbol{t}) = M_s \, \boldsymbol{m}(\boldsymbol{r}, \boldsymbol{t}), \qquad |\boldsymbol{m}| = 1. \tag{2.1}$$

2.1.1 Micromagnetic energy functional

The different stable states of the magnetic system and their stability depend on the different interactions contributing to the free energy of the system. The magnetic free energy of a ferromagnet is a functional of the magnetization $\boldsymbol{m}(\boldsymbol{r}, \boldsymbol{t})$ and its spatial derivatives. The total energy $E[\boldsymbol{m}]$ is obtained by

integrating the energy density $\mathcal{E}[\boldsymbol{m}]$ over the magnetic system,

$$E[\boldsymbol{m}] = \int_V \mathcal{E}[\boldsymbol{m}] \; d^3r. \tag{2.2}$$

The equilibrium configuration of the magnetic system depends on the nature of different magnetic interactions contributing to the free energy. The different ground states can be obtained by minimizing the energy functional with respect to the magnetization. This can be done by imposing that the first variation of the energy functional vanishes;

$$\delta E[\boldsymbol{m}] = 0. \tag{2.3}$$

It is important to note here that, the ground states are obtained by comparing the energies of different extremal solutions, which apriori could be minimum, maximum, or saddle points. Thus, it is important to look at these different magnetic interactions in more detail to understand the nature of the system and its different magnetization patterns.

Exchange interaction

The exchange interaction is a quantum mechanical effect resulting from the Coulomb repulsion between different electrons and Pauli's exclusion principle. This interaction is responsible for ferromagnets as it favors parallel alignment of spins and is isotropic, i.e., it is independent of the orientation of the magnetic moments w.r.t crystal lattice. The simplest model for explaining the exchange interaction is the Heisenberg exchange interaction, and its energy is given by,

$$E_{ex} = -\sum_{i,j} J_{ij} \; \boldsymbol{S}_i \cdot \boldsymbol{S}_j, \tag{2.4}$$

where J_{ij} is the strength of the exchange interaction between two neighbouring spins $\boldsymbol{S}_i$ and $\boldsymbol{S}_j$. One can see from Eq. (2.4) that a positive sign of J_{ij} results in a ferromagnetic ordering, and a negative J_{ij} results in anti-ferromagnetic ordering in the magnetic material. In the micromagnetic framework, the ex-

change energy density for a ferromagnet can be written using continuum limit approximation as

$$\mathcal{E}_{ex} = A\left(\nabla \boldsymbol{m}\right)^2, \tag{2.5}$$

where, A is the exchange stiffness constant and $\left(\nabla \boldsymbol{m}\right)^2$ stands for $\left(\nabla m_x\right)^2 + \left(\nabla m_y\right)^2 + \left(\nabla m_z\right)^2$. It is more evident from Eq. (2.5) that whenever the spins are not aligned, the free energy of the system increases for a ferromagnet.

Magnetic anisotropy

The exchange interaction is isotropic (see Eq. (2.5)), i.e., the direction of the magnetization has no preferred spatial direction. However, often in magnetic materials, the magnetization prefers certain directions (easy axes) or certain planes (easy planes) perpendicular to certain axes along which it is aligned. This preference arises as a result of coupling between the spin and orbital motion of electrons in the crystal lattice, also known as spin-orbit coupling (SOC). The anisotropic energy contribution to the magnetic energy depends on the relative orientation of the magnetization with respect to crystallographic axes. In this thesis, we will only focus on one type, namely, uniaxial anisotropy, which is the simplest case with only one preferred direction in the crystal. The energy density contribution of the uniaxial anisotropy is given by

$$\mathcal{E}_{anis} = K_u\left(1 - \left(\boldsymbol{m}\cdot\boldsymbol{u}\right)^2\right), \tag{2.6}$$

where $\boldsymbol{u}$ is the preferred axis, and K_u is the anisotropy constant. Note that the anisotropy energy is minimal when the magnetization direction is out of plane (fully up or down) and maximal when the magnetization lies in the plane. The higher-order terms ($\mathcal{O}(\boldsymbol{m})^4$) are generally small and are neglected, and only the second-order term is considered here. Note that when $K_u > 0$, the anisotropy energy is minimized with the magnetization aligned parallel to the anisotropy direction u, and when $K_u < 0$, the magnetization prefers to align in the plane perpendicular to the anisotropy axis to minimize the energy, and hence the name hard-axis or easy-plane.

Dzyaloshinskii-Moriya interaction

The spin-orbit coupling describes the relativistic interaction between the spin of an electron and its orbital angular momentum. In magnetic materials, the SOC gives rise to a wide variety of emergent phenomena such as the perpendicular magnetic anisotropy (PMA), the spin Hall effect, the Rashba-Edelstein effect, and the Dzyaloshinskii-Moriya interaction (DMI) [83]. DMI was first discovered in antiferromagnets (AFM) in 1958 by Dzyaloshinskii as the origin of the phenomenon called "weak ferromagnetism" [84]. Based on phenomenological considerations and using symmetry arguments, he explained the canted antiferromagnetism observed in hematite. Shortly after, in 1960, Moriya found a microscopic mechanism and pointed out that the combination of spin-orbit interaction and broken inversion symmetry could give rise to canting of magnetic moments, and a small non-zero magnetization is observed even in the absence of external magnetic fields, thus losing the perfect antiferromagnetic order in the material [85, 86].

In this section, we shall describe the DMI, an antisymmetric exchange interaction that occurs in systems lacking inversion symmetry (non-centrosymmetric crystal structures) [40, 87, 88] and at interfaces between a magnetic film layer and heavy-metal (HM) layer with strong SOC [89, 90]. DMI tends to rotate the spins, which competes with isotropic exchange interaction and magnetic anisotropy. This interplay of interactions gives way to the stabilization of a rich variety of chiral magnetic textures, such as chiral domain walls, spin spirals, and magnetic skyrmions. [40, 91–93].

Within the micromagnetic framework, the DMI can be expressed by inhomogeneous variants, that are linear w.r.t first spatial derivatives of the magnetization of type [94, 95]

$$\mathcal{L}_{ij}^{k} = m_i \frac{\partial m_j}{\partial m_k} - m_j \frac{\partial m_i}{\partial m_k}, \tag{2.7}$$

where i, j, k are spatial variables, and $\mathcal{L}_{ij}^{k}$ is a Lifshitz invariant. Such Lifshitz invariants were first introduced in the theory of phase transitions [96]. The form of the Lifshitz invariants depends on the crystallographic symmetry and results in corresponding profiles of modulated magnetic textures. The general

form of the Lifshitz invariants and their structure in different symmetry classes will be discussed later in Sec 3.6.

Bulk DMI

In noncentrosymmetric crystal structures such as MnSi [40], FeGe [87], and [97], the inversion symmetry is broken intrinsically and gives rise to bulk DMI. In the continuum approximation, this bulk-DMI energy density is expressed as

$$\mathcal{E}_{bulk} = D_{bulk}\ \boldsymbol{m} \cdot (\nabla \times \boldsymbol{m})\,, \tag{2.8}$$

where D_{bulk} is the bulk-DMI strength with units of Jm^{-2}. The spin spirals and skyrmions resulting from this type of DMI are of Bloch type, where the magnetization rotates such that there is a non-zero component orthogonal to the spiral direction 2.1(a).

Néel DMI

DMI arises at interfaces when the inversion symmetry is naturally broken when a FM layer is placed on a HM-layer with strong SOC, such as Fe/Ir [98], CoFe/Pt, and CoFe/Ta [99], or multilayer systems where a FM layer is sandwiched between two HM layers like Pt/Co/Ru, Pt/Co/Ir [100] and Ir/Fe/-Co/Pt [101]. The resulting DMI is hence referred to as interfacial DMI, and this type of DMI stabilizes Néel spirals and skyrmions, where the magnetization rotates in the plane of spiral direction and homogeneous magnetization direction 2.1(b). The expression of the interfacially-DMI energy density is given by

$$\mathcal{E}_{\text{Néel}} = D_{\text{Néel}}\ \big[\,(\boldsymbol{m} \cdot \nabla)\, m_z - m_z\,(\nabla \cdot \boldsymbol{m})\,\big], \tag{2.9}$$

where $D_{\text{Néel}}$ is the interfacial-DMI strength with units of Jm^{-2}. In the present work, we shall investigate the modulated magnetic textures in in-plane magnets and the relevant DMI in those systems. To avoid any confusion, we shall refer to interfacial DMI as Néel-DMI from here on further.

Zeeman energy

The magnetic moments interact with the externally applied magnetic field via Zeeman interaction, which tends to align the magnetization in the same direction as the applied magnetic field. The energy density is expressed as

$$\mathcal{E}_{ext} = -\mu_0 M_s \boldsymbol{m} \cdot \boldsymbol{H}_{ext}, \tag{2.10}$$

where, $\mu_0 = 4\pi \times 10^{-7}$ Tm/A is the vacuum permeability.

Demagnetization energy

The demagnetization field is created by the magnetic moments within the magnetic body. From Maxwell equations the total magnetic field $\boldsymbol{B}$ can be written as,

$$\boldsymbol{B} = \mu_0 \left(\boldsymbol{H_d} + \boldsymbol{M} \right), \tag{2.11}$$

where, $\boldsymbol{M}$ is the total magnetization and $\boldsymbol{H}_d$ is the stray field. As the total magnetic field $\boldsymbol{B}$ is conserved, according to Gauss law,

$$\nabla \cdot \boldsymbol{B} = 0, \tag{2.12}$$

the stray field $\boldsymbol{H}_d$ can be obtained from the magnetic scalar potential Φ in the form $\boldsymbol{H}_d = -\nabla\Phi$. This results in a Poisson equation for Φ,

$$\nabla^2 \Phi = \nabla \cdot \boldsymbol{M}. \tag{2.13}$$

The general solution of this Poisson equation is given by

$$\Phi = \int dV' \frac{\rho(\boldsymbol{r'})}{4\pi|\boldsymbol{r} - \boldsymbol{r'}|} + \int dS' \frac{\sigma(\boldsymbol{r'})}{4\pi|\boldsymbol{r} - \boldsymbol{r'}|}, \tag{2.14}$$

where $\rho(\boldsymbol{r}) = -\nabla \cdot \boldsymbol{M}(\boldsymbol{r})$ and $\sigma(\boldsymbol{r}) = \boldsymbol{M}(\boldsymbol{r}) \cdot \boldsymbol{n}(\boldsymbol{r})$ are the volume and surface charge densities, respectively. The stray field therefore reads

$$\boldsymbol{H}_d(\boldsymbol{r}) = -\nabla \left[\int dV' \frac{\rho(\boldsymbol{r}')}{4\pi|\boldsymbol{r} - \boldsymbol{r}'|} + \int dS' \frac{\sigma(\boldsymbol{r}')}{4\pi|\boldsymbol{r} - \boldsymbol{r}'|} \right]. \tag{2.15}$$

Furthermore, the demagnetization energy density can be cast in the following Zeeman-like form:

$$\mathcal{E}_{demag} = -\frac{\mu_0}{2} M_s \boldsymbol{m} \cdot \boldsymbol{H}_d. \tag{2.16}$$

In summary, the calculation of demagnetization fields involves the use of Maxwell equations to solve for the magnetic field generated by the magnetization distribution, which becomes very demanding both analytically and numerically. However, one can calculate explicitly the demagnetization energy in some simple cases.

The demagnetization field of a uniformly magnetized body can be expressed in terms of a demagnetization tensor [102]. For example, the demagnetization field of an uniformly magnetized ellipsoid is linearly related to the magnetization $\boldsymbol{M}$ by the demagnetization tensor $\mathcal{N}$ [103]

$$\boldsymbol{H}_d = M_s \left(\mathcal{N} \cdot \boldsymbol{m} \right). \tag{2.17}$$

Assuming (a,b,c), the principal axes of the ellipsoid are pointing along $\hat{x}, \hat{y}, \hat{z}$ axes of the 3D coordinate system, the demagnetization tensor assumes a diagonal form with $(\mathcal{N}_x, \mathcal{N}_y, \mathcal{N}_z)$ as the demagnetization factors. The sum of three demagnetization factors is always equal to one, which means only two of them are independent. For simple geometries, the demagnetization factors can be deduced by symmetry. In a sphere (ellipsoid with equal principal axes, $a = b = c$) that is uniformly magnetized, symmetry dictates that the demagnetization factors are all equal to 1/3 [104].

In cases of non-uniform geometries like cylindrical and rectangular magnetized bodies, the demagnetization fields are not uniform, even if the samples are assumed to be uniformly magnetized. Thin film magnetic materials can

be treated as flattened oblate ellipsoids where the thickness of the film is very small relative to lateral dimensions [102]. For an infinite thin film with a magnetization direction normal to the plane, the demagnetization factor is $(0, 0, 1)$, and hence its demagnetization energy density takes the form [104]

$$\begin{aligned}\mathcal{E}_{demag}^{film} &= -\frac{\mu_0}{2} M_s \boldsymbol{m} \cdot \boldsymbol{H}_d \\ &= -\frac{\mu_0}{2} M_s^2 m_z^2. \end{aligned} \tag{2.18}$$

which has a form similar to that of an uniaxial anisotropy [see Eq. (2.6)]. This approximation can be used for magnetization distributions with cylindrically symmetric skyrmions (having very thin domain wall widths) [42]. However, when the magnetization varies along the x and y directions, this approximation for demagnetization energy no longer holds, and a different scheme must be implemented. This will be discussed in detail when dealing with in-plane magnetized films and their relevant skyrmions in section 3.5.

Domain walls in films with PMA

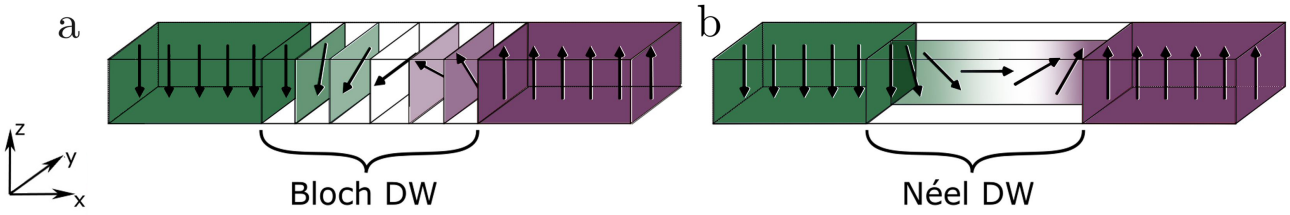

Figure 2.1: Schematic representation of DW in a ferromagnetic thin film with PMA. (a) Bloch wall and (b) Néel wall. The difference between the two DW configurations is in the direction of rotation of the magnetization from one domain to the other. See text for details.

In ferromagnetic thin films with PMA, if the film is uniformly magnetized out-of-plane, magnetic charges appear at the opposite edges, thus increasing the total demagnetizing energy. To minimize this energy, domains with opposite magnetization directions are formed. The boundary between two domains is called a domain wall (DW). Inside the DW, the magnetization gradually rotates from pointing in the direction of one domain to the other. The DW

width is determined by the competition between the exchange and anisotropy energies on the one hand and the demagnetizing energy on the other hand. Two different DW configurations are possible in a magnetic thin film with PMA, viz, Bloch and Néel types, as shown in Fig. (2.1).

In a Bloch DW, the magnetization rotates gradually from up ($-\hat{z}$) to down ($+\hat{z}$) in the DW plane (yz plane in Fig. (2.1), while it rotates within the perpendicular to the DW plane (xz plane in Fig. (2.1) in a Néel case. In both cases, the magnetization component normal to the wall plane (along $\hat{x}$ for Bloch wall and along $\hat{y}$ for Néel wall) remains zero.

In ferromagnetic thin films with PMA, Bloch DW minimizes the magnetostatic energy. The higher energetical stability of the Bloch wall, when compared with the Néel wall, stems from the nature of the magnetic charges from these walls. In the Néel wall, magnetization aligned normal to the wall plane ($\hat{x}$) creates magnetic charges on both sides of the DW, which generate a demagnetizing field in the opposite ($-\hat{x}$) direction. However, when the width of the film reduces, the demagnetizing energy of the Bloch wall increases due to surface charges in the $\hat{y}$-direction. Eventually, the Néel wall becomes more stable. The transition between Bloch and Néel DWs has been observed in nanostrips of Co/Ni multilayer thin films using spin-transfer toques [105, 106].

Let us now consider the presence of Néel DMI arises in thin films when the inversion symmetry is naturally broken 2.1.1. In the presence of such DMI, there is an energy gain that can outweigh the demagnetizing energy contribution and stabilize a Néel DW [99, 107]. The DW energy with DMI is given by [93, 108]:

$$\sigma_{DW} = 4\sqrt{AK} - \pi D. \tag{2.19}$$

From Eq (2.19), we can see that the exchange interaction and the magnetic anisotropy yield a positive contribution to the domain wall energy, whereas the DMI yields a negative contribution. At a critical value of the DMI, $D_c = 4\sqrt{AK}/\pi$, the energy of the domain wall is exactly zero. For low DMI strengths ($D < D_c$), the domain wall energy is positive, which leads to a chiral DW being

a local minimum over the ferromagnetic state ground state. However, when DMI is large ($D > D_c$), the energy of the domain wall is negative, and the ground state is a series of many parallel domain walls called the spin spiral state.

2.1.2 Magnetization dynamics

Based on the phenomenological approach, in 1935, Landau & Lifshitz proposed a dynamical equation for magnetization [109]. Later in 1954, Gilbert introduced an alternative form for including the damping interaction in the system [110], and the combined form is known as the Landau-Lifshitz-Gilbert equation (LLG). The LLG equation thus determines the spatial and temporal evolution of the magnetization and reads

$$\partial_t \boldsymbol{m} = -\gamma \left(\boldsymbol{m} \times \boldsymbol{H}_{\text{eff}}\right) + \alpha \left(\boldsymbol{m} \times \partial_t \boldsymbol{m}\right). \tag{2.20}$$

The first term on the right-hand side of Eq. (2.20) represents the precessional motion of the magnetization around the effective field. When the magnetization is not aligned with the field $\boldsymbol{H}_{\text{eff}}$, it is subjected to a torque causing a precessional motion with precession frequency $f = \gamma \left|\boldsymbol{H}_{\text{eff}}\right| / 2\pi$. This precessional motion would continue forever if not for various energy dissipation processes, leading to another term in the Eq. (2.20).
The second term in Eq. (2.20) captures the phenomenological damping describing the dissipation of energy, which results in aligning the magnetization with the effective field. The dissipation torque $\boldsymbol{m} \times \partial_t \boldsymbol{m}$ is perpendicular to the precessional torque, pointing towards the effective field $\boldsymbol{H}_{\text{eff}}$. These two torques are represented in Fig. 2.2. γ and α represent the gyromagnetic ratio and dimensionless Gilbert damping factor, respectively. Typical values of the damping factor are of the order of 10^{-2} - 10^{-3} [104].

2.1.3 Numerical micromagnetics

The LLG equation has had enormous success in static domain structures and dynamics of magnetization switching. But, it is a nonlinear partial differential equation and can be solved analytically only for a few cases. The natural way to proceed is to use a numerical approach and perform micromagnetic simula-

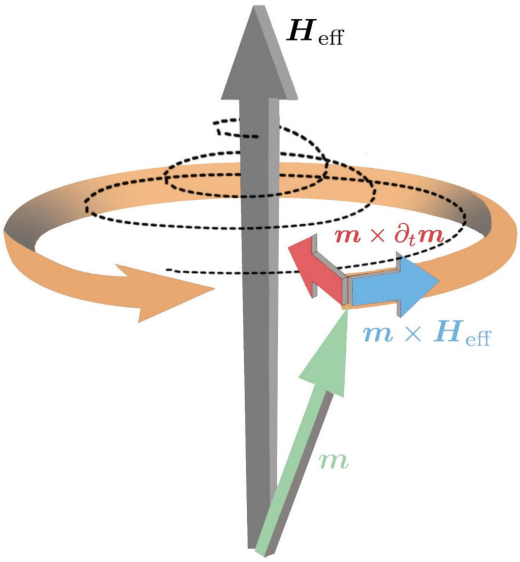

Figure 2.2: Magnetization dynamics described by the LLG equation. The field-like torque, $\boldsymbol{m} \times \boldsymbol{H}_{\text{eff}}$ (blue arrow), due to the effective field $\boldsymbol{H}_{\text{eff}}$ (grey), leads to a continuous precessional motion of the magnetization $\boldsymbol{m}$ (green). The damping-like torque $\boldsymbol{m} \times \partial_t \boldsymbol{m}$ (red) slowly aligns the magnetization along the direction of the effective field. This magnetization trajectory of the combined torques is represented by the dotted black spiral in the figure.

tions to determine the static and dynamic behavior of the magnetization.

The numerical solution to the LLG is calculated by solving the differential equation iteratively. To this end, we use well-developed scientific packages to do the necessary simulations. Among the several open-source packages in the micromagnetic community, MicroMagnum [111] and mumax3 [112] are used in this thesis based on specific requirements and efficacies. The Mumax3 software package developed by the DyNaMat group of the University of Ghent runs on NVIDIA's graphical processing units (GPUs), making them one of the fastest codes and having very low computation time. However, the current-driven dynamics in this package [1] do not account for the geometry, meaning there is no Laplace equation solver to accurately calculate the current density in

[1] latest version of the open source code available

different geometric shapes. This particular feature is developed in Micromagnum, is easily extensible, and runs on both CPU and GPUs. Both of these are finite-difference-based micromagnetic software packages and are chosen based on the problem at hand.

Before we proceed further, it is worth discussing a few challenges to the numerical approach due to the micromagnetic equations' complexity and nonlinearity. Since the micromagnetic framework relies on the magnetization varying smoothly, the spatial discretization of the LLG equation should be smaller than the exchange length, which is usually a few nanometers. This would result in $\mathcal{O}(10^4 - 10^6)$ discretization cells for a system of $(100 - 1000)$nm in 2D alone. Second, as discussed before (see Sec.2.1.1), the stray field interaction is a non-local, long-rage interaction. Thus the computation of stray field energy should be calculated between all spatial cells, which makes the computation very expensive. Micromagnetic numerical simulation packages like Mumax3 [112], Micromagnum [111], and OOMMF [113] reduce this computational complexity by employing fast Fourier transform methods. Upon a finite difference discretization, the computation of the stray field reduces to evaluating a convolution of the magnetization with a demagnetizing kernel. Hence, this discrete convolution in Fourier space is just a point-wise tensor-vector multiplication that lowers the computation cost from $\mathcal{O}(N^2)$ for a direct implementation to $\mathcal{O}(N\ log(N))$ when using the fast Fourier transform methods. This can be further sped up efficiently by parallelizing the numerical computation on CPU/GPUs. Finally, to determine the accurate time evolution dynamics, usually in the order of a few femto to picoseconds, time integration routines require a considerable amount of time steps creating another bottleneck to solving the LLG equation.

2.2 Current-induced spin torques

The ability to manipulate magnetic textures and understand their dynamic behavior holds a key role in the success of spintronics. One can influence the magnetic textures via spin torques induced by spin-polarized currents or electric currents in the system [114]. Understanding the mechanism of how

magnetization couples to current could reveal new pathways to develop new spin-based technology applications. Depending on the nature of their origin, there are different types of current-induced spin torques. In this section, we are going to introduce two different types of current-induced spin torques: (i) Spin-transfer toque (STT), (ii) Spin-orbit torque (SOT), whose effects are very often investigated for magnetic skyrmions [115]. The detailed investigations of these torques on magnetic skyrmions will be discussed in chapters (4 & 5).

2.2.1 Spin-transfer torque

In 1996, Berger [116] and Sloncwezski [117] independently predicted that when a spin-polarized electric current flows through a magnetic material, there is an exchange of angular momentum between the itinerant electrons and the localized electrons (here responsible for magnetization in the material). This leads to a torque applied on the local magnetization by the conduction electrons, hence the name spin-transfer torque [118, 119]. STT has been observed in MTJs [120, 121] and on magnetic domain walls [122, 123], and depending on how the spin texture changes, STT can be adiabatic or non-adiabatic, whose effects on the DW motion are discussed below.

Adiabatic spin-transfer torque

The adiabatic STT proposed earlier historically describes the case when the conduction electrons flow through the DW adiabatically, as shown schematically in the Fig. 2.3. If the domain wall is wide enough, i.e., when the magnetic moments within the domain wall rotate gradually from the direction of one domain to the other domain, spins of the conduction electrons can perfectly follow the local magnetic moments inside the DW adiabatically, and the direction of conduction electrons spin changes. However, the conservation of spin angular momentum dictates that this torque on the conduction electrons leads to another torque on the magnetic moments inside the DW. This torque exerted on the magnetic moments of the DW by the conduction electrons is known as adiabatic STT and has the following form.

$$\boldsymbol{\tau}_{ad}^{STT} = \zeta \Big[\boldsymbol{m} \times (\boldsymbol{j} \cdot \boldsymbol{\nabla}) \boldsymbol{m} \Big] \tag{2.21}$$

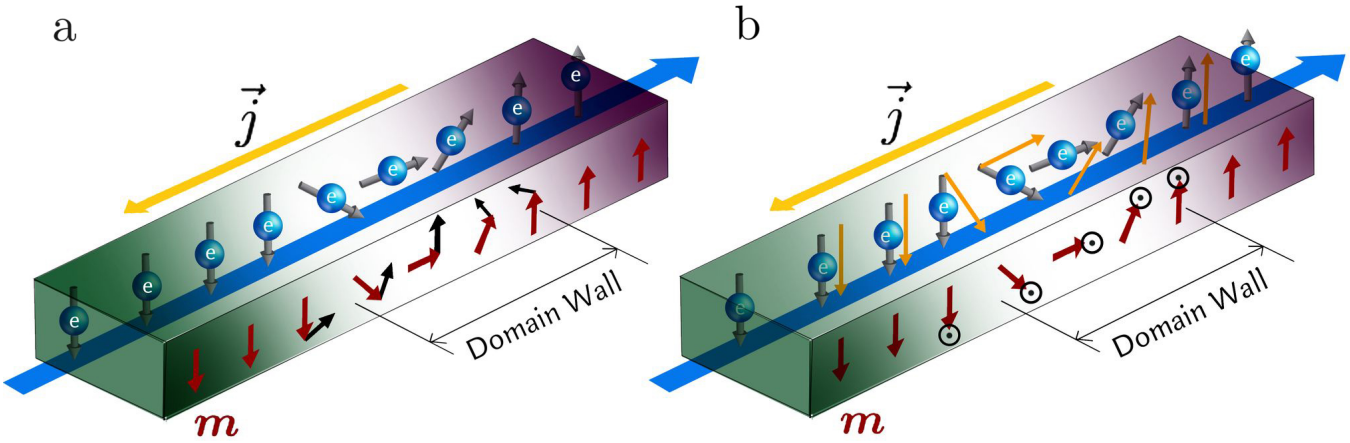

Figure 2.3: Schematic description of the adiabatic and non-adiabatic STT for the DW motion. (a) In the case of adiabatic STT, the spin-polarized conduction electrons (grey arrows) will orient in the direction of the local magnetic moments (red arrows) in the DW adiabatically. This results in a torque (shown in black arrows) exerted on the magnetic moments, which moves the DW along the direction of electron flow (blue arrow). (b) When the DW becomes narrower, there is a spatial mistracking of spins between conduction electrons and the magnetic moments in the DW. In this case, non-adiabatic STT (shown in black circles) is applied on the spins of the DW, which is perpendicular to adiabatic STT.

Here, $\zeta = \gamma P\hbar/2eM_s$ is the charge-to-spin conversion factor in the adiabatic regime, P represents the electron spin polarization, $\hbar$ is the reduced Planck constant, and e is the electron charge. This results in a DW motion along the direction of electron flow.

Non adiabatic spin-transfer torque

Non-adiabatic spin-transfer torque was introduced to explain the discrepancies in the experimental results with that predicted by adiabatic STT. The velocities of the DWs measured were much smaller than the ones expected using solely the adiabatic term [123–127]. When the DW is narrower, the adiabatic approximation fails as the angle between adjacent spins in the DW is larger. In such a case, the conduction electron spins cannot follow the local magne-

tization perfectly, leading to spatial mistracking of spins between conduction electrons and the magnetic moments in the DW. Thus, they are reflected at the DW, resulting in momentum transfer, and by conservation of angular momentum, the DW is pushed in the direction of electron flow. The non-adiabatic STT is orthogonal to the adiabatic STT and has the following form [128]

$$\boldsymbol{\tau}_{non-ad}^{STT} = -\zeta\beta\, \boldsymbol{m} \times (\boldsymbol{m} \times (\boldsymbol{j} \cdot \boldsymbol{\nabla})\boldsymbol{m})\,. \tag{2.22}$$

Here β parameterizes the strength of the non-adiabatic torque. Current-driven DWs will be affected by both contributions (adiabatic and non-adiabatic STT). However, depending on the thickness of the DW, one of these contributions can overshadow the other: For very wide DWs, the adiabatic STT will dominate the DW motion, and in the limit of very thin DWs the momentum transfer will dominate. Thus the interaction between the spin-polarized currents and the magnetic texture can be modelled by taking into account both the adiabatic and non-adiabatic STT to the LLG equation (2.20) [128]

$$\begin{aligned}\partial_t \boldsymbol{m} = -\gamma\ (\boldsymbol{m} \times \boldsymbol{H}_{\text{eff}})\ +\ \alpha\ (\boldsymbol{m} \times \partial_t \boldsymbol{m})\ +\ \underbrace{\zeta \boldsymbol{m} \times (\boldsymbol{j} \cdot \boldsymbol{\nabla})\boldsymbol{m}}_{\text{adiabatic STT}} \\ -\ \underbrace{\zeta\beta\, \boldsymbol{m} \times (\boldsymbol{m} \times (\boldsymbol{j} \cdot \boldsymbol{\nabla})\boldsymbol{m})}_{\text{non-adiabatic STT}}\,.\end{aligned} \tag{2.23}$$

Here the first two terms represent the precession and damping terms as described before (Sec. 2.1.2),

2.2.2 Spin-orbit torque

Recently, an alternative way to produce spin torques has been introduced using spin-orbit coupling in inversion asymmetric heavy metals. This new field of spin-orbitronics focuses on spin torques arising from spin-orbit interaction to control magnetization dynamics [129–132].

We consider a bilayer consisting of a chiral magnet on top of a heavy-metal layer, as shown in Fig 2.4. When the current flow in the heavy-metal (HM) layer is along the $+\hat{x}$ direction (green arrow in the figure), due to the Spin-Hall effect a spin current with its polarisation $\boldsymbol{\sigma}$ (yellow arrow in the figure) along the $+\hat{y}$ direction would flow along the $+\hat{z}$ direction. This spin current induces

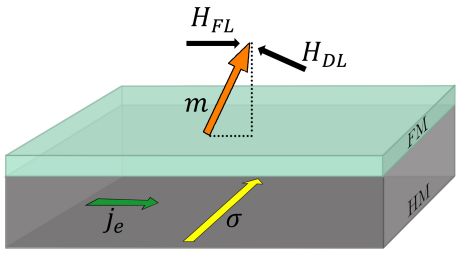

Figure 2.4: Geometry considered for spin-orbit torque. The bottom layer in grey represents the heavy metal (HM) layer, and the top layer, shaded in green, represents the ferromagnetic (FM) layer. The green arrow and yellow arrow indicate the electric current j_e, and the polarization of the spin current σ with its polarization in the HM. The orange arrow represents the magnetization $\boldsymbol{m}$, the two black arrows are the fields $H_{\mathrm{FL}}, H_{\mathrm{DL}}$ corresponding to field and damping like SOT torques.

field-like and damping-like torques on the magnetization (orange arrow in the figure) in the ferromagnetic layer (FM). This SOT-driven dynamics of the magnetization $\boldsymbol{m}$ can be described by the LLG equation taking into account the adiabatic and non-adiabatic torque components [132–134],

$$\partial_t \boldsymbol{m} = \underbrace{-\gamma\,(\boldsymbol{m}\times\boldsymbol{H}_{\mathrm{eff}})}_{\text{precession}} + \underbrace{\alpha\,(\boldsymbol{m}\times\partial_t\boldsymbol{m})}_{\text{damping}} + \underbrace{\tau_{\mathrm{FL}}\,(\hat{z}\times\boldsymbol{j})\times\boldsymbol{m}}_{\text{field-like SOT}} + \underbrace{\tau_{\mathrm{DL}}\,\boldsymbol{m}\times(\hat{z}\times\boldsymbol{j})\times\boldsymbol{m}}_{\text{damping-like SOT}}, \tag{2.24}$$

where again the first two terms represent the precession and damping terms, and the third and fourth terms represent the fieldlike and damping-like SOTs respectively. Here, the spin polarisation $\boldsymbol{\sigma} = (\hat{z}\times\boldsymbol{j})$ is along the $+\hat{y}$ direction. τ_{FL} and τ_{DL} parametrize the field-like and damping-like strengths of the SOT, respectively.

2.3 Magnetic skyrmions: An overview

In the previous section, we saw an overview of different interactions in magnetic materials and their description within the micromagnetic framework. The competition between these interactions leads to a variety of stable magnetic

configurations. In this section, we will briefly review magnetic skyrmions and certain key aspects regarding their stability, creation, current-driven dynamics, and excitations.

Skyrmions are named after British nuclear physicist Tony H. R. Skyrme. The theory of skyrmions originates from his pioneering works published in the early 1960s [135, 136]. He proposed a non-linear field theory of pions whose static, topologically stable particle-like solutions describe baryons (like protons and neutrons). Today Skyrme's theory has found applications beyond particle physics, such as liquid crystals [137, 138], Bose-Einstein condensates [139–141], quantum Hall ferromagnets [142, 143], and magnetic systems with broken inversion symmetry [40, 45, 88, 98, 144].

As introduced in the previous chapter (1.4), magnetic skyrmions are chiral textures with a whirlpool-like winding of magnetization. The presence of DMI lowers the energy by canting the magnetization (see Sec. 2.1.1), which helps to stabilize skyrmions. The 2D magnetization texture of a skyrmion in a chiral thin film is represented in Fig. 1.3. The non-trivial topology of a magnetic skyrmion can be characterized by topological charge (or winding number), $\mathcal{Q}$ [145], defined by:

$$\mathcal{Q} = \frac{1}{4\pi} \iint dxdy \; \boldsymbol{m} \cdot \left(\frac{\partial \boldsymbol{m}}{\partial x} \times \frac{\partial \boldsymbol{m}}{\partial y} \right). \tag{2.25}$$

The topological charge calculates the number of times the magnetization wraps around the unit sphere. For the FM saturated state, $\partial_x \boldsymbol{m} = \partial_y \boldsymbol{m} = 0$ (since spins are all parallel) and hence $\mathcal{Q} = 0$, making it a topologically trivial state. Also, any magnetic texture that can be continuously deformed into the FM state is topologically trivial as well. To calculate the topological charge of a skyrmion in an uniformly magnetized background, it is convenient to parameterize two-dimensional plane in cylindrical coordinates $\boldsymbol{r} = (\rho\cos\phi,\ \rho\sin\phi)$, and the magnetization can be written as,

$$\boldsymbol{m}(\boldsymbol{r}) = \big(\cos\Phi(\phi)\sin\Theta(\rho),\ \sin\Phi(\phi)\sin\Theta(\rho),\ \cos\Theta(\rho)\big). \tag{2.26}$$

By substituting Eq. (2.26) into Eq. (2.26), the topological charge is computed as follows:

$$\begin{aligned}\mathcal{Q}_{Sk} &= \frac{1}{4\pi}\int_0^{\infty} d\rho \int_0^{2\pi} d\phi \left(\sin\Theta(\rho)\frac{d\Theta(\rho)}{d\rho}\frac{d\Phi(\phi)}{d\phi}\right) \\ &= \frac{1}{4\pi}\left[-\cos\Theta(\rho)\right]_{\rho=0}^{\rho=\infty}\left[\Phi(\phi)\right]_{\phi=0}^{\phi=2\pi}. \end{aligned} \tag{2.27}$$

Since there are several possibilities for the texture of a magnetic skyrmion, we define the vorticity m and the helicity γ to characterize the skyrmion as follows:

$$\begin{aligned}\Phi(\phi) &= m\phi + \gamma \\ m &= \frac{1}{2\pi}\left(\Phi(2\pi) - \Phi(2\pi)\right). \end{aligned} \tag{2.28}$$

Now, if $\boldsymbol{m}$ points in the $-\hat{z}$ direction at the origin and along $+\hat{z}$ at infinity, then the boundary conditions on $\Theta(\rho)$ are,

$$\Theta(0) = \pi, \qquad \Theta(\infty) = 0. \tag{2.29}$$

Using Eq. (2.29) and (2.28), we get $Q = -m$. A magnetic skyrmion is described by $m = 1$, and thus its topological charge is $\mathcal{Q} = -1$. An antiskyrmion corresponds to a spin configuration with $m = -1$ and its corresponding topological charge being $\mathcal{Q} = 1$.

If $\boldsymbol{m}$ points in the $\hat{z}$ direction at the origin and along $-\hat{z}$ at infinity, then boundary conditions on $\Theta(\rho)$ are modified to $\Theta(0) = 0$, $\Theta(\infty) = \pi$. This would yield $\mathcal{Q} = m$, and a magnetic skyrmion (antiskyrmion) would have a topological charge of $1(-1)$.

Depending on the nature of the DMI, magnetic skyrmions stabilized in the system have well-defined vorticity m and helicity γ. In systems with Bulk DMI the most stable state is a Bloch skyrmion with $\gamma = \pm\pi/2$ and, the most stable state in systems with interfacial (Néel) DMI are the Néel skyrmions which have $\gamma = 0, \pi$. A classification of magnetic skyrmions corresponding to their vorticity $m = \pm 1$ and helicity $\gamma = 0, \pm\pi/2$ are depicted in Fig. 2.5.

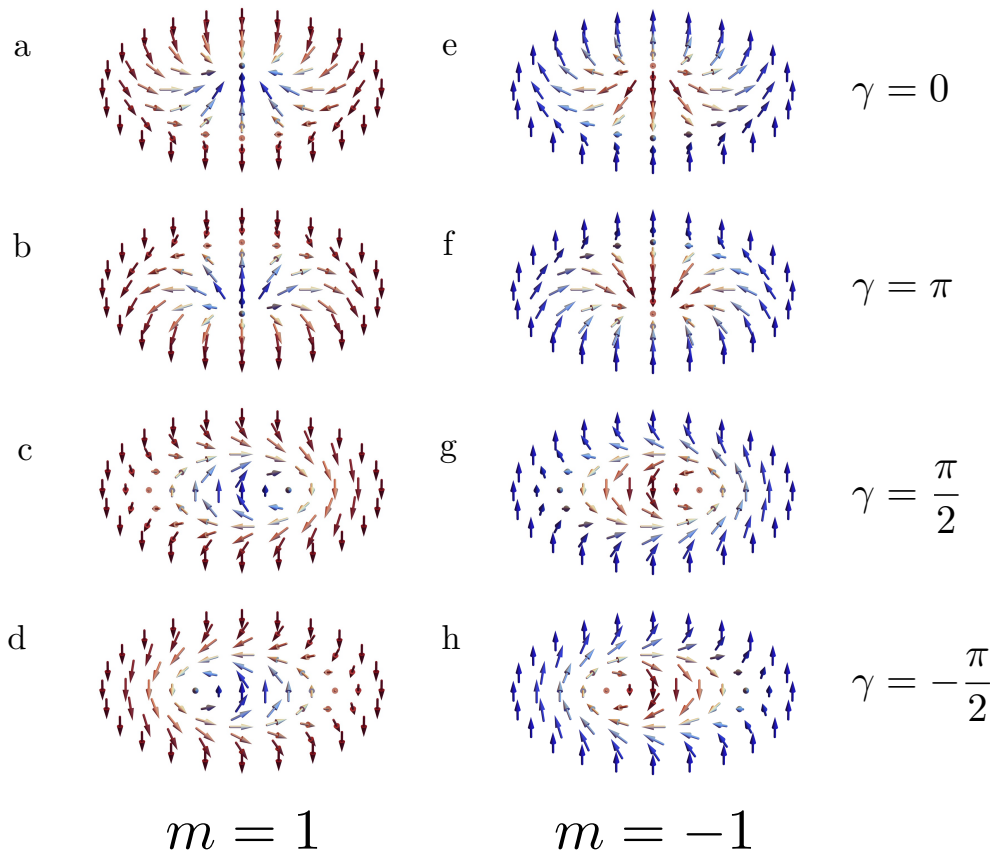

Figure 2.5: Classification of magnetic skyrmions. This figure depicts the spin configuration of skyrmion for $m = 1$ (left column **a-d**) and -1 (right column **e-h**) and different values of γ.

2.3.1 Observations of magnetic skyrmions

Skyrmions in magnetic materials were first predicted to appear as stable structures in chiral magnets theoretically [41, 42]. The breakthrough came with the first experimental observation of skyrmions in bulk non-centrosymmetric crystals of MnSi [40, 146]. Since then, a lot of new materials have been reported to host skyrmions of different types ranging from Bloch to Néel skyrmions [144]. We shall discuss the advent of magnetic skyrmions in both cases separately.

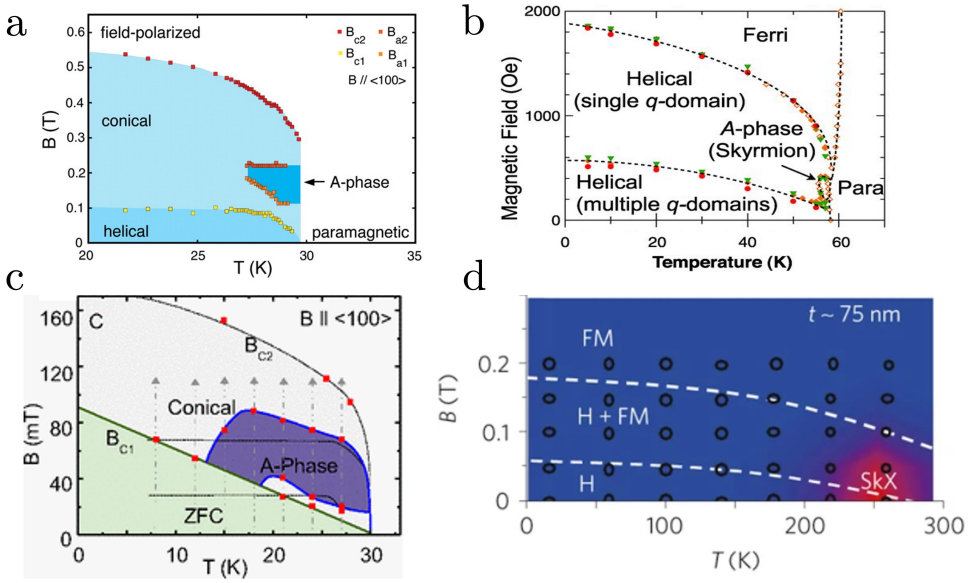

Figure 2.6: Magnetic phase diagrams of (a) MnSi [40], (b) FeGe [88], (c) $Fe_{1-x}Co_xSi$ [87, 147, 148] and (d) Cu_2OSeO_3 [149].

Skyrmions in bulk systems with broken inversion symmetry

Magnetic skyrmions were observed in the form of skyrmion lattices in MnSi. Since then, they have reported found in other materials like $Fe_{1-x}Co_xSi$ [87, 147, 148], FeGe [88, 150], and Cu_2OSeO_3 [149, 151, 152]. The magnetic phase diagram for the temperature versus external field in bulk chiral magnets shares qualitative features as shown in Fig. (2.6). The ground state at zero applied field is a helix, where the magnetization twists around helix pitch, denoted by a wavevector q. The magnitude of the pitch of the helix is given by Q=D/J, and the cubic anisotropy of the material determines its direction. The helical state transforms into the conical state as the applied field increases. In the conical state, the wave vector is parallel to the applied field leading to a non-zero magnetization pointing towards the applied field and rotation in the plane perpendicular to the applied field, resembling a conical shape as shown in Fig. 2.6(a). With a further increase in the applied magnetic field, the conical state gets narrower and transforms into a ferromagnetic state. These long-range magnetic orders exist only below the Curie temperature, and for temperatures above the Curie temperature, the system is paramagnetic, with

magnetization pointing in arbitrary directions and zero total magnetization. The skyrmion lattice (SkL) appears in a narrow pocket in the phase diagram close to Curie temperature. This phase was first observed using small-angle neutron scattering experiments in MnSi. As the DMI in these materials is bulk DMI, the magnetic textures in these materials are of Bloch type.

Skyrmions in thin films with interfacial DMI

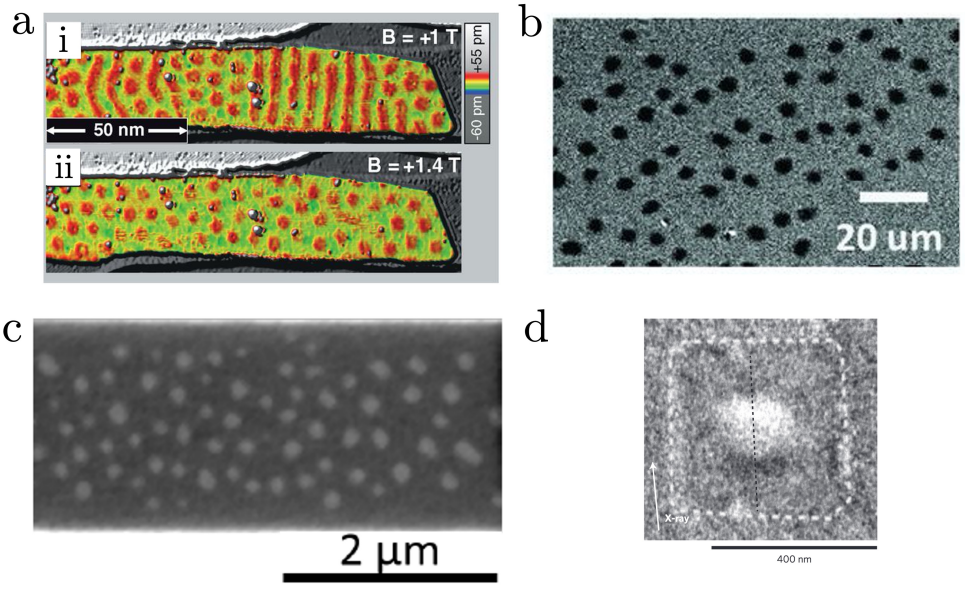

Figure 2.7: Observations of magnetic skyrmions. (a) Nanometer scale Skyrmions observed in an PdFe bilayer grown on Ir(111). The transition from (i) stripe phase to (ii) skyrmions happen with increasing external fields [153]. Magnetic skyrmions in HM/FM/NM layers observed at room temperature (b) $Ta/Fe_{60}Co_{20}B_{20}/TaO_x$ using polar magneto-optical Kerr effect (MOKE) microscopy [44], (c) in $Pt/Co_{60}Fe_{20}B_{20}/MgO$ by scanning transmission X-ray microscopy STXM [45] and, (d) Pt/Co/MgO at zero external fields using XMCD-PEEM method [154].

As introduced in Section 2.1.1, DMI arising at interfaces can stabilize chiral structures in multilayer thin films. Skyrmions in thin-film systems were first observed in monolayers of Fe [98] and bilayers of PdFe [153] epitaxially grown on Ir(111) surface [153]. In these systems, DMI contribution comes from the strong spin-orbit coupling of the heavy metal Ir. The skyrmion lat-

tice stabilized in PdFe/Ir system had a square symmetry and a lattice period of only 1 nm. It was demonstrated that different phases could be stabilized by controlling the external magnetic fields (Fig. 2.7a). However, their stabilization required large external magnetic fields as well as very low temperatures. Quite recently, room temperature skyrmions were observed in HM/FM/NM multilayers. Jiang et al [44] demonstrated the formation of skyrmion bubbles in $Ta/Fe_{60}Co_{20}B_{20}/TaO_x$ trilayer at room temperatures using spatially divergent current-induced SOTs (Fig. 2.7b). They further demonstrated that the skyrmions varied in size between 700 nm and 2 μm depending on the strength of the external magnetic field. Woo et al., [45] reported the presence of Néel skyrmions lattices in ultrathin Pt/Co/Ta and Pt/CoFeB/MgO stacks at zero applied field and room temperature (Fig. 2.7c). Boulle et al., [154] demonstrated thermally stable Skyrmions in Pt/Co/MgO films at zero applied magnetic fields and at room temperatures. The observed skyrmions were of size 120 nm and were stable and reversible with respect to perturbations at zero external magnetic fields (Fig. 2.7d).

2.3.2 Current-driven skyrmion dynamics

Skyrmion Hall effect

Spin structures, like DWs, can be moved using spin-polarized currents, as was described in the previous section. A current-induced rotation of the skyrmion lattice was discovered in MnSi early on following the experimental discovery of skyrmions [61] and was described theoretically in the works below [155–157]. An interesting result of a skyrmion's topology manifests itself in its current-driven dynamics. Here, the motion along the applied current's direction coexists with transverse motion. This transverse motion is caused by the gyrotropic forces. This effect is described as the Skyrmion Hall effect (SkHE). Recently, magnetic multilayers were used to illustrate the SkHE [45, 158].

2.3.3 Conclusions

In this chapter, we saw the description of magnetism on nanometer to micrometer length scales using micromagnetic theory. The different contributions to the energy functional were introduced to describe various magnetic configurations such as domain walls, helices, and magnetic skyrmions. The theoretical

description of magnetic skyrmions, their experimental discovery and later observation in different materials, and the Skyrmion Hall effect were then briefly discussed. These concepts will be put into practice in the following chapter when we investigate the stability of magnetic skyrmions in in-plane magnets and address the key aspects of their symmetries.

Chapter 3

Stability of in-plane skyrmions

This chapter presents the study of magnetic skyrmions in thin film in-plane magnets. We shall first introduce the micromagnetic model for in-plane magnetized thin films, followed by the description of in-planes skyrmions and their spin structure. Then we shall present the numerical results showing the effect of DMI on the size of in-plane skyrmions and the effect of dipolar-dipolar interactions on them. Later, the Biaxial anisotropy model is introduced to analytically explain the complex effect of dipolar-dipolar interactions in in-plane magnets. Then, a brief discussion on the symmetries of the Dzyaloshinskii-Moriya interaction is presented, and potential material candidates to host in-plane skyrmions are proposed. Finally, the stability of the in-plane skyrmions in the monoclinic system with mirror symmetry is analysed a phase diagram is provided.

3.1 Introduction

In the previous chapter 1, we saw that a magnetic in-plane skyrmion could be considered as a PMA skyrmion whose magnetic moments have been rotated around an in-plane axis (in this case 90° y-axis) as shown in Fig. 3.1. In a Néel skyrmion, the out-of-plane component of the magnetization is radially symmetric about its center. In contrast, in an in-plane skyrmion, the in-plane component of the magnetization is now radially symmetric about its center. The magnetization at the center of an in-plane skyrmion is aligned with the in-plane anisotropy direction and far away from the center along the opposite direction. In theory, in-plane skyrmions have the topological characteristics of Néel skyrmions.

In-plane skyrmions have been observed in epitaxial MnSi/Si(111) thin films [78, 79]. A two-dimensional square lattice of merons and antimerons was reported in $Co_8Zn_9Mn_3$ [159], and more recently, isolated pairs of meron–antimeron have been stabilized in Permalloy film via magnetic imprinting [160]. In recent years, in-plane skyrmions are gaining a lot of traction and have been predicted theoretically to be a stable solution in ferromagnets [80, 82], antiferromagnets [57, 161], and frustrated magnetic systems [162, 163]. In the next section, we shall investigate the micromagnetic model and the interactions that stabilise in-plane skyrmions in thin films.

3.2 In-plane micromagnetic model

In ferromagnetic thin films, the interaction between the various magnetic energy contributions—exchange, anisotropy, DMI, Zeeman, and dipolar-dipolar interactions—leads to the stability of the magnetic skyrmions. In order to understand this stability, we shall use the micromagnetic model introduced in the last chapter 2. Let us begin by considering a chiral ferromagnetic thin film deposited on a heavy metal layer uniformly magnetized along the z-axis. The

micromagnetic energy functional is given by,

$$\mathcal{E}_{\text{PMA}}[\boldsymbol{m}] = \int_{\mathcal{S}} d^2\boldsymbol{r} \left\{ \frac{A}{2} \left(\nabla \boldsymbol{m}\right)^2 + K\left(1 - m_z^2\right) + D_{\text{Néel}} \mathcal{L}_{\text{Néel}}[\boldsymbol{m}] - \boldsymbol{m} \cdot \left(\boldsymbol{H} + \boldsymbol{H}_d\right) \right\}, \tag{3.1}$$

where $\boldsymbol{m}$ denotes the unit magnetization vector (normalized by the saturation magnetization M_s, $|\boldsymbol{m}| = 1$), A, $D_{\text{Néel}}$, and K are the exchange stiffness, Dzyaloshinskii, and on-site anisotropy constants of the system respectively. $\boldsymbol{H}$ and $\boldsymbol{H}_d$ are the normalized (normalized by M_s) external and dipolar magnetic fields, respectively. $\mathcal{L}_{\text{Néel}}[\boldsymbol{m}]$ is a Lifshitz invariant that models the DMI interaction in terms of the spatial variations of the magnetization,

$$\mathcal{L}_{\text{Néel}}[\boldsymbol{m}] = m_z \partial_x m_x - m_x \partial_x m_z + m_z \partial_y m_y - m_y \partial_y m_z. \tag{3.2}$$

Now, the energy functional stabilising an in-plane skyrmion can be obtained by applying a rotation in spin space of angle $\pi/2$ along the y-axis to Eq. (3.1), which would yield

$$\mathcal{E}_{\text{in-pl}}[\boldsymbol{m}] = \int_{\mathcal{S}} d^2\vec{r} \left\{ \frac{A}{2} \left(\nabla \boldsymbol{m}\right)^2 + K\left(1 - m_x^2\right) + D_{\text{ip}} \mathcal{L}_{\text{in-pl}}[\boldsymbol{m}] - \boldsymbol{m} \cdot \left(\boldsymbol{H} + \boldsymbol{H}_d\right) \right\}, \tag{3.3}$$

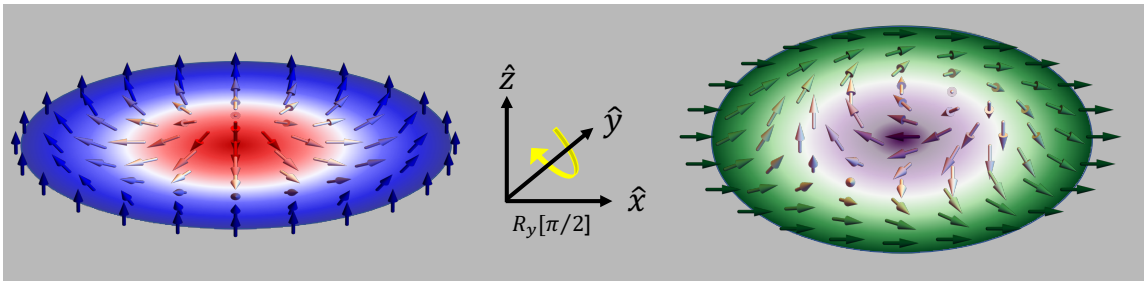

Figure 3.1: An in-plane skyrmion (green) can be obtained by rotating an Néel skyrmion (blue) by 90° around an $\hat{y}$-axis. The magnetization at the centre rotates from $-z$ to -x direction, and similarly, the uniform background smoothly deforms from out-of-plane (z) to in-plane (x) direction.

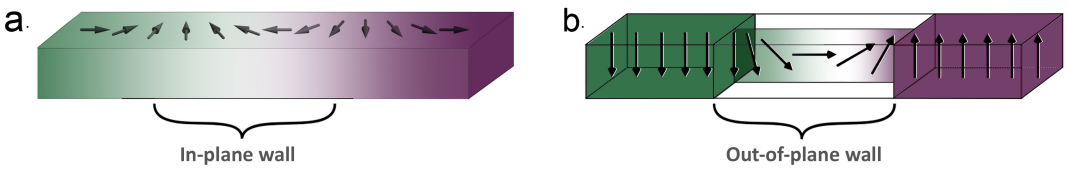

Figure 3.2: Schematic representation of in-plane DW in a ferromagnetic thin film. The magnetization rotates gradually from pointing right to left in the plane of the thin film.

where the uni-axial anisotropy direction is along x-axis, and the stray field is pointing outwards from the edges of the thin film. The exchange stiffness term remains unchanged on account of being the gradient square of the magnetization. However, the functional form of the Lifshitz invariant is transformed as follows,

$$\mathcal{L}_{\text{in-pl}}[\boldsymbol{m}] = m_z\partial_x m_x - m_x\partial_x m_z + m_x\partial_y m_y - m_y\partial_y m_x, \tag{3.4}$$

Comparing Eqs. (3.2) and (3.4), we can see that the nature of rotation of the magnetization has changed from a PMA film to an in-plane film. The $\mathcal{L}_{\text{in-pl}}[\boldsymbol{m}]$ causes rotations in $z-x$ and $x-y$ planes (see Fig. 3.2) in contrast to $\mathcal{L}_{\text{Néel}}[\boldsymbol{m}]$, which causes rotations in $z-x$ and $z-y$ planes. The consequences of this striking difference in skyrmions will be discussed in the next Sec. (3.3).

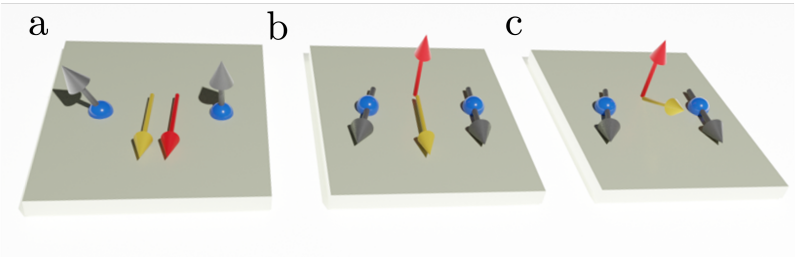

Figure 3.3: Schematic representation of the geometry of magnetic atoms (blue) and the DMI vector (yellow) for different magnetization configurations [(a) out-of-plane, (b),(c) in-plane]. The magnetization vector, the cross product ($\boldsymbol{m}_i \times \boldsymbol{m}_j$) and the DMI vector are denoted by grey, red and yellow arrow respectively.

It is important to note the key symmetry distinctions between the bulk, Néel, and in-plane DMI here. In the previous chapter (2.1.1), we examined two types of DMI, viz. Bulk DMI, which is present in crystals with broken inversion symmetry like B20 crystallographic structures, and Néel DMI, which arises at interfaces in thin-film multilayer systems. The symmetry of DMI determines the type of structure formed. In thin films with PMA and broken inversion symmetry at the interface, the DMI vector (yellow arrows in Fig. 3.3a) lies in the plane perpendicular to the vector between two spins (black arrows in Fig. 3.3a), resulting in a non-zero contribution to the energy. However, in in-plane magnetized systems, the DMI vector lies in the same plane as the magnetization with no net chiral energy contribution (Fig. 3.3b). Hence the chiral structures stabilized by the DMI in an in-plane magnetized film are less common. Realizing chiral spin textures in thin films with in-plane anisotropy requires a form of DMI whose out-of-plane component is non-zero (Fig. 3.3c). The in-plane DMI in Eq. (3.4) qualifies this criterion and stabilises both in-plane and out-of-plane domain walls as shown in Fig. 3.2. Recently, out-of-

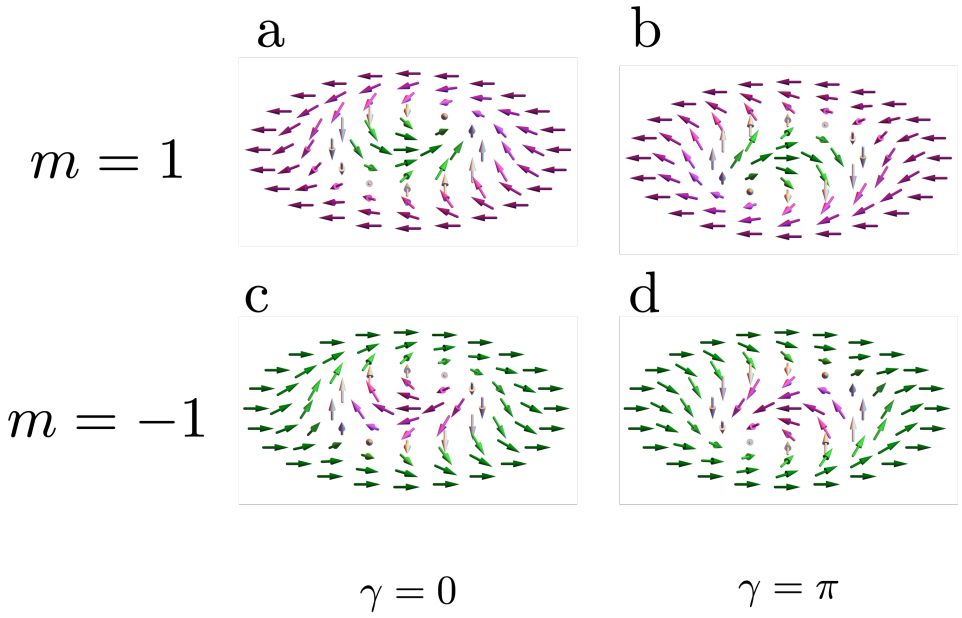

Figure 3.4: Classification of in-plane skyrmions. This figure depicts the spin configuration of skyrmion for $m = 1$ (top row **a,b**) and -1 (bottom row **c,d**) and values of $\gamma = 0, \pi$.

plane chiral spin structures were reported in an in-plane magnetized ultrathin film system consisting of Fe/Ni bilayers grown on a W(110) crystal [164]. Here the chirality is introduced by the interplay of in-plane uniaxial anisotropy, a perpendicular anisotropy, and interfacial DMI contributions. The symmetry of the in-plane DMI will be further examined in the Sec. 3.6, along with potential crystal classes that could support this type of DMI. Similar to Néel skyrmions in PMA magnets,in-plane skyrmions can be stabilized with a well-defined vorticity m and helicity γ that have the symmetries given by the in-plane DMI mentioned in Eq. 3.4. A classification of in-plane skyrmions corresponding to their vorticity $m = \pm 1$ and helicity $\gamma = 0, \pm\pi/2$ are depicted in Fig. 3.4.

3.3 Structure of in-plane skyrmions

In the previous section, we discussed the in-plane micromagnetic model and the corresponding in-plane DMI that stabilizes in-plane skyrmions. Let us now analyze the influence of the DMI strength on the stability and the size of both Néel and in-plane skyrmions.

Micromagnetic simulations were performed to obtain the relaxed equilibrium configuration. The micromagnetic parameters for exchange, anisotropy, saturation magnetization, and Gilbert damping are given in the Table 3.1. The reduced DMI parameter $g = \pi D/4\sqrt{AK}$ is varied between 0.7 and 1.0. The simulation geometry was a square geometry with 128 nm lateral size and thickness of 1 nm with the discretization of 1 cell per cubic nanometer and, periodic boundary conditions were employed. The size of the simulation geometry was chosen such that the skyrmion size was always less than 50% of the simulation edge.

A (J/m)	K (J/m^3)	α	M_s (A/m)	g
$1.5 \cdot 10^{-11}$	$5.0 \cdot 10^5$	0.15	$5.8 \cdot 10^5$	0.7-0.99

Table 3.1: Values of the micromagnetic parameters utilized in the simulations of skyrmion relaxation for the skyrmion radius plots in Fig.3.6.

For Néel skyrmions, the radius of the skyrmions is defined as the distance

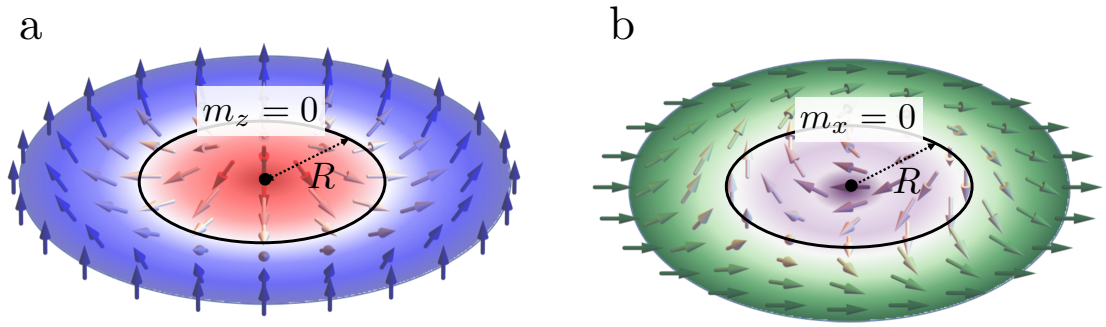

Figure 3.5: Schematic representation of the definition of radius for (a) Néel skyrmions and (b) in-plane skyrmions respectively, with the radius as defined by the Eq. (3.5).

between the center of the skyrmion to the circle where the z-component of magnetization goes to zero (3.5a) (magnetization is in-plane). Similarly, for the case of in-plane skyrmion, the radius is defined as the distance between the center of the skyrmion to the circle where the x-component of magnetization goes to zero (3.5b). The schematic representation of the skyrmion radius definition is illustrated in Fig. 3.5.

$$m_z(R) = 0, \quad \text{for Néel skyrmions} \tag{3.5a}$$

$$m_x(R) = 0, \quad \text{for in-plane skyrmions} \tag{3.5b}$$

The radius of these skyrmions calculated as a function of DMI is shown in Fig. 3.6a. First, we can see that in the absence of stray fields, the radius of an in-plane and Néel skyrmion (blue and magenta curves) are precisely the same. This stems from the fact that two energy functions are related by a rotational mapping in the spin space (see Sec.3.2). The skyrmion radius increases monotonically with increasing DMI for both of these skyrmions. When g tends toward 1 ($D \to D_c$), the skyrmion radius diverges. This can be understood from the contribution of A, K, and D to the energy of a chiral DW (2.19). For large skyrmions, we can assume that the circular domain wall of a Néel/in-plane has the same profile as an isolated relaxed domain wall [93].

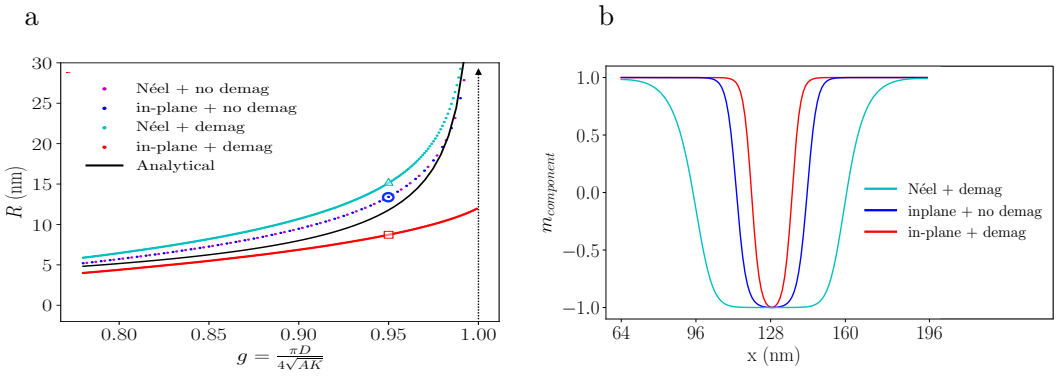

Figure 3.6: (a) Radius of Néel and in-plane skyrmions in the absence (blue and magenta curves) and presence (cyan and red curves) of stray fields (demag). The black solid curve denotes the associated g value. analytical dependence on the reduced DMI parameter as proposed in [165]. (b) Radial magnetization profile m_x (red) and m_z (cyan) in the presence of stray fields for Néel and in-plane skyrmions, respectively. The blue curve corresponds to radius profile in the absence of stray fields for in-plane skyrmions. The corresponding value of g and radius are marked by □, △ and ◯ respectively in (a). This figure and caption are adapted from our work [82].

With such an approximation, we can see that larger A and K result in a higher DW energy (2.19), favoring smaller DWs, and, therefore, smaller skyrmions. As g increases, DW energy decreases, resulting in larger skyrmions. When g tends toward 1 ($D \to D_c$), the skyrmion energy approaches zero, and correspondingly the skyrmion radius diverges, leading to the formation of spin spirals. The analytical solution to the radius of the skyrmions as a function of the DMI strength calculated in Ref [165] is given by $R_{Sk} = \sqrt{2}|g|/\sqrt{1-2g^2}$ (black curve in the Fig. 3.6).

3.4 Effect of dipolar interactions

In Sec. 2.1.1, we saw that the effect of magnetostatic interactions is non-trivial, and the calculations of stray field energies are the most computationally intensive due to their nonlocal nature. In this section, we will compare their impact on in-plane skyrmions and Néel while qualitatively describing their influence. We shall address the stray field effects in detail in Sec. 3.5 using an analytical model and micromagnetic simulations. Here, The effect of stray fields on

the stability of skyrmions has been investigated by performing micromagnetic simulations in Mumax3 and Micromagnum.

In Fig. 3.6a, we see that the radius of Néel skyrmions (cyan curve) increases in the presence of stray fields. In a PMA magnet, in order to lower the total energy, stray fields increase the width of the domain wall and thereby increasing the radius of the Néel skyrmions. However, the radius of the in-plane skyrmion (red curve) is decreased in the presence of stray fields. The magnetization profile in each case is shown in Fig. 3.6b for the value of $g = 0.95$. It can be seen that the size of the skyrmion core varies in each case. This contrast-

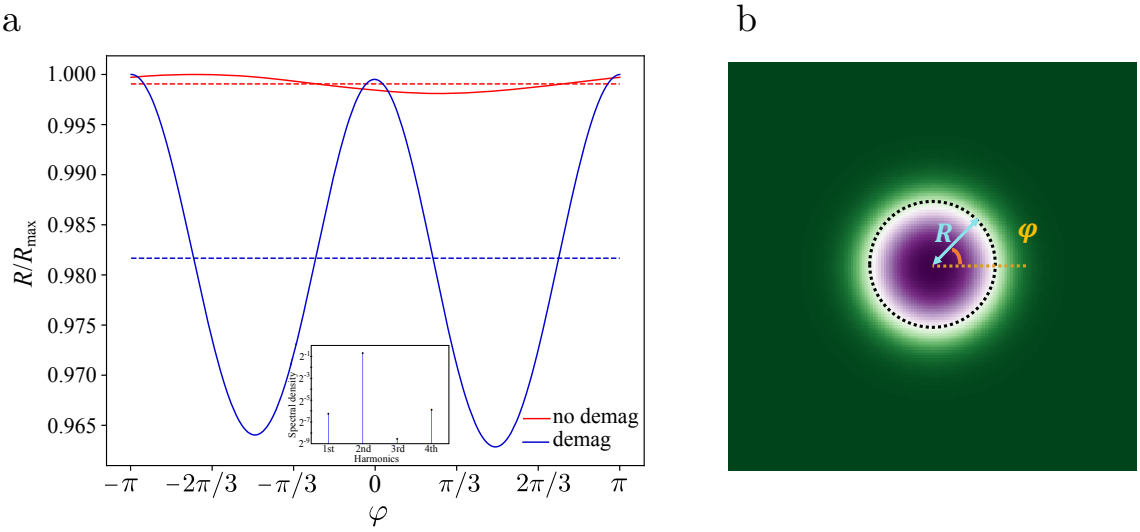

Figure 3.7: (a) The dependence of the radius of in-plane skyrmions on the azimuthal angle φ is examined in two scenarios: with the presence of stray fields (depicted in blue) and without them (depicted in red). The dashed lines represent the angular average or mean radius. To facilitate comparison, the radii are normalized by the maximum observed radius, R_{max}, for the skyrmion. It should be noted that the numerical estimation of the radius is influenced by finite size effects on the scale of the cell size ($\sim$ 1 nm), hence the red curve represents the average. Additionally, the inset shows the spectral density corresponding to the angular dependence mentioned earlier in the case of the stray-field scenario. (b) Schematic representation of the radius measured as a function of azimuthal angle φ. For each value of φ. the radius (R) is defined as the distance between the center of the skyrmion to the contour where the x-component of magnetization goes to zero.

ing behaviour originates from the different nature of stray fields in PMA and in-plane polarised magnetic thin films. In a uniformly magnetized infinite thin film with PMA, the demagnetization factor is (0, 0, 1), and the surface charges accumulate on top and bottom surfaces. In an in-plane magnetized film, the magnetic charges are now on the edges of the thin film while still having the demagnetization factor (0, 0, 1) because of its infinite thin film shape.

Another significant effect of the stray fields is the deformation of in-plane skyrmions. Fig. 3.7 shows the angular dependence of the size of the in-plane skyrmion in the presence and absence of stray fields. For each value of the azimuthal angle φ, the size of the skyrmion is defined as the distance between the center of the skyrmion to the circle where the x-component of magnetization goes to zero (see Fig. 3.7b). In the absence of stray fields, the fluctuations of the radius of the skyrmion is less than 0.2%, which appears due to spatial discretization in the simulations. In the presence of stray fields, the skyrmion size varies from a maximum to a minimum in the range $[0, \pi/2]$. This can be understood by looking at the magnetization profile along $\varphi = 0$ and $\varphi = \pi/2$ directions. The DW along $\varphi = 0$ is a Néel wall with magnetization rotating in $x - z$ plane, and the presence of stray fields increases the width of the DW. However, along $\varphi = \pi/2$ direction, it is an in-plane DW with the rotation of the magnetization along $x - y$ plane, and the stray fields have the opposite effect and reduces the width of DW and thus the size of the skyrmion along this direction. The spectral decomposition of the variation $R(\varphi)$ reveals harmonic terms of the second order being the dominant ones and smaller fourth order contributions in the natural frequency $\omega_\varphi = 1$ as shown in the inset of Fig. 3.7a.

Thus, the stray fields acting on an in-plane skyrmion break the cylindrical symmetry leading to different nature of magnetization profile along different φ direction. This φ dependent DW profile stems from the very nature of in-plane DMI. In the next section, we shall analyse the symmetries of the DMI and their consequences on the structure of the in-plane skyrmions.

3.5 Biaxial anisotropy

For an infinite thin film with uniform magnetization perpendicular to the film, the magnetic dipolar energy can be recast as a effective anisotropy term. As a result, the effective anisotropy constant of the magnet becomes $K_{\text{eff}} = K - 0.5\ \mu_0 M_s^2$, the second contribution being rooted in the presence of stray fields [103]. This anisotropy-like approximation was shown to be valid also for axial-symmetric modulated structures in thin films with uniform background pointing normal to the film (like Néel skyrmions) [42]. However, this approach fails in the case of an in-plane magnetized film, so that special care must be taken when considering the effect of stray fields. In this section, we consider a biaxial anisotropy model to account for the magnetic dipolar energy in in-plane magnetized films. This idea is motivated by the fact that the demagnetization tensor in ultra-thin films reduces to $\text{diag}(0, 0, N_{zz})$, where the z axis points along the normal to the magnetic film.

3.5.1 The model

We consider an ultra-thin ferromagnetic film with an in-plane uniaxial anisotropy, where chiral magnetic modulations are stabilized by an in-plane DMI. The magnetic dipolar energy will be modeled by an additional out-of-plane uniaxial anisotropy. The long-wavelength free-energy functional for the magnetization $\boldsymbol{m}$ is given by

$$\mathcal{E}[\boldsymbol{m}] = \int_{\mathcal{S}} d^2\boldsymbol{r} \left\{ \frac{A}{2}(\nabla \boldsymbol{m})^2 + D\mathcal{L}_{\text{in-pl}}[\boldsymbol{m}] - \boldsymbol{m}\cdot\boldsymbol{H} \right. \\ \left. + K_x[1-(\boldsymbol{m}_x)^2] + K_z[1-(\boldsymbol{m}_z)^2] \right\}, \tag{3.6}$$

where K_x, K_z denote the in-plane and out-of-plane anisotropy constants, respectively. Here, A, D and H are the exchange stiffness, the Dzyaloshinskii-Moriya strength and the external magnetic field, respectively. In addition, $\mathcal{L}_{\text{in-pl}}[\boldsymbol{m}]$ is a Lifshitz invariant defined as

$$\mathcal{L}_{\text{in-pl}}[\boldsymbol{m}] = \boldsymbol{m}_z\partial_x\boldsymbol{m}_x - \boldsymbol{m}_x\partial_x\boldsymbol{m}_z + \boldsymbol{m}_x\partial_y\boldsymbol{m}_y - \boldsymbol{m}_y\partial_y\boldsymbol{m}_x \tag{3.7}$$

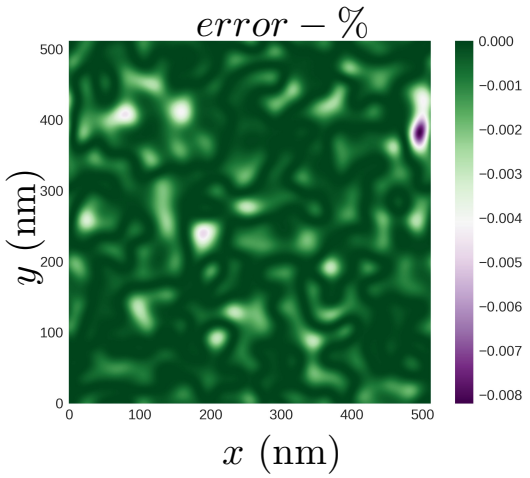

Figure 3.8: Comparison of the magnetization results obtained between the proposed biaxial model with Mumax3's native calculation. The spatial distribution of the error percentage of the thin film of dimensions $(512 \times 512 \times 1)\text{nm}^3$ is calculated. The error percentage is measured with respect to Mumax3's demagnetization kernel calculations.

This form of the Lifshitz invariant induces chiral spin spiral rotations in $x - z$ and $x - y$ planes in the system.

3.5.2 Validity of the model

To verify our proposed effective model for the demagnetizing field, we compare it to its direct evaluation by means of the demagnetization kernel calculator of MuMax3: we consider a thin film with a square geometry of lateral size 512 nm and thickness 1 nm, with cell size $1 \times 1 \times 1$ nm^3, which is homogeneously magnetized along x-direction and we determine the ground state magnetization by using both approaches. The relative error is defined as $\delta m_{ijk} = \left(m_{ijk}^{bi-axial} - m_{ijk}^{Mumax3}\right)/m_{ijk}^{Mumax3}$. The results are shown in Fig. 3.8. We note that the relaxed magnetization state is in agreement with Mumax3's demagnetization field calculations within an error less than 0.01%. The simulations were repeated for different dimensions, with the square length varying from 128 nm to 2048 nm, and similar results were obtained.

3.5.3 Effect of Biaxial anisotropy on in-plane skyrmions

In the previous section (Sec. 3.4), we saw that the in the presence of stray fields, the cylindrical symmetry of the in-plane skyrmion is broken, leading to an asymmetric radial profile. We performed Mumax3 simulations using the effective biaxial model for different values of $K_{\text{ratio}} = \frac{K_z}{K_x}$ keeping K_x fixed, and the resulting magnetization profiles are shown in Fig. 3.10(a).

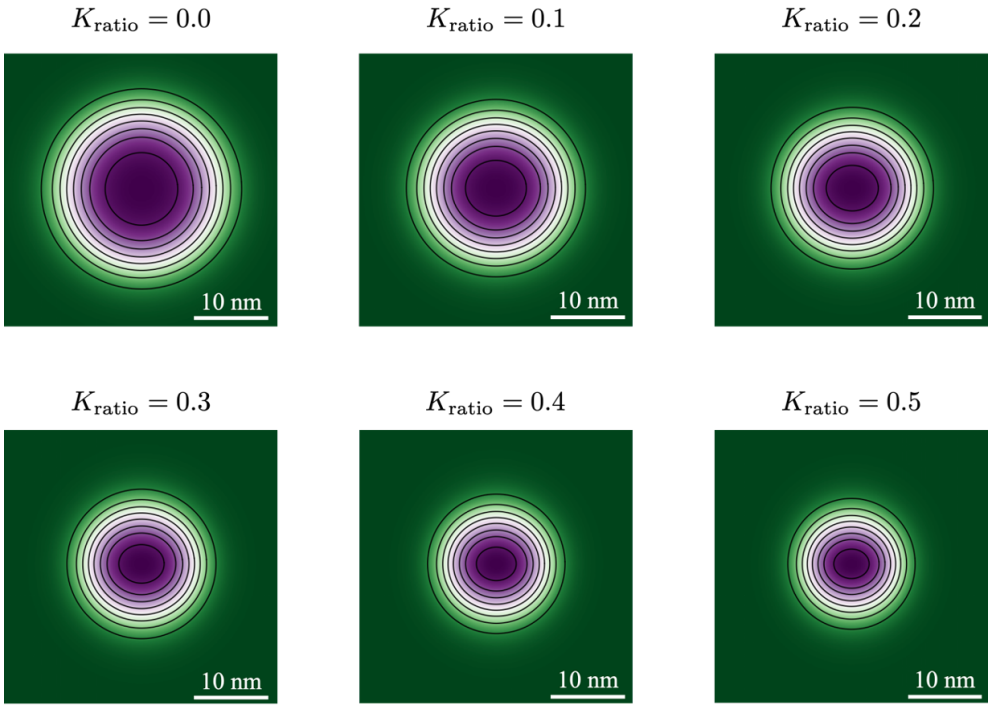

Figure 3.9: Magnetization density plots for different values of K_{ratio} for a fixed value of $K_x = 1\times16^6$ Jm^{-3}. The in-plane skyrmions shown here were stabilized within the biaxial model (Eq. (3.6)). It can be seen from the contours that the cylindrical symmetry is broken for nonzero values of K_{ratio}.

The comparison of the skyrmions stabilized with account of the biaxial model and of the full demagnetization calculation in Mumax3 is shown in Fig. 3.10(a). The size of the skyrmions decreases as K_z increases. Also, the cylindrical symmetry is broken for all values of K_{ratio}, such that the maximum (minimum) size occurs along the parallel (perpendicular) direction to the in-plane (x) easy axis. The radial profile from the biaxial model matches to the

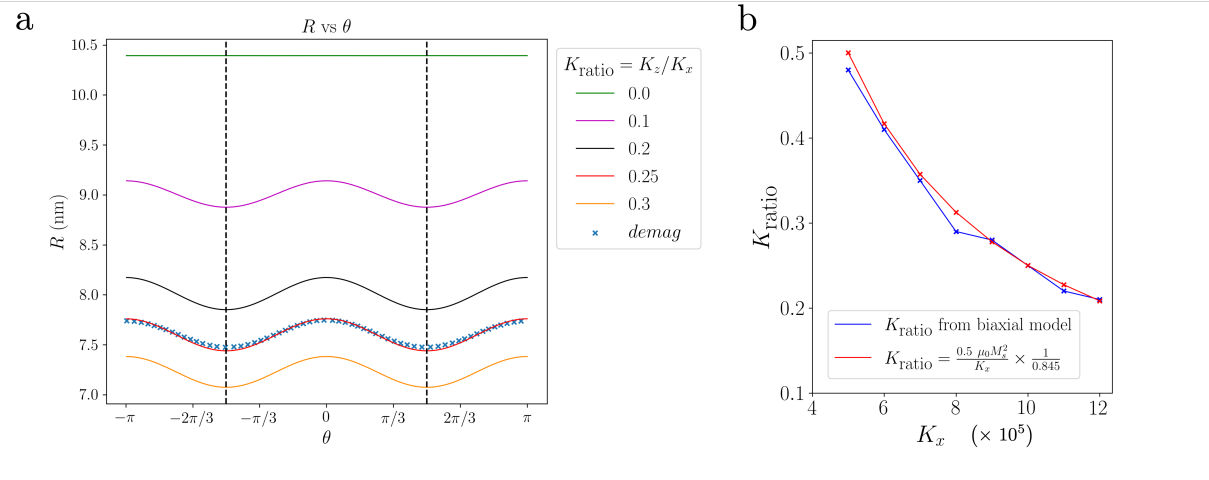

Figure 3.10: Comparison between the biaxial model and the Mumax3 full demagnetization calculation. (a) Size of the in-plane skyrmion as a function of the azimuthal angle φ for different values of K_{ratio}. The skyrmions are stabilised within the biaxial model (Eq. (3.6)). The size of the skyrmion obtained with account of Mumax3's full demagnetizing field calculation is shown in blue ($\times$). Note that the profiles from the two approaches match for $K_{\text{ratio}} = 0.25$. (b) The value of K_{ratio} at which the biaxial model and Mumax3's demagnetization field calculation match is shown as a function of the in-plane anisotropy K_x (blue curve). The red curve represents the value of K_{ratio} obtained via the expression $\frac{0.5\ \mu_0 M_s^2}{K_x} \times \frac{1}{0.845}$.

one obtained from MuMax3's full demagnetization field calculation for $K_{\text{ratio}} = 0.25$, which is equal to $\frac{0.5\ \mu_0 M_s^2}{K_x} \times \frac{1}{0.845}$. We note that the numerical factor 0.845 arises from 1) the demagnetizing factor of the finite sized cuboid shape of the thin film and 2) the nonuniform nature of the skyrmion magnetization field. To check the consistency of these results, the value of K_{ratio} that reproduces the effect of the demagnetizing field was calculated as a function of in-plane anisotropy (K_x), and the results are shown in Fig. 3.10(b).

3.6 Symmetries of Dzyaloshinskii-Moriya interaction

In ferromagnets (FMs), in the continuum limit, DMI is described by so-called Lifshitz invariants, which are linear w.r.t first spatial derivatives of the magnetization (see Eq. (2.7)), which was briefly addressed in chapter 2. In this section, the symmetries of the different types of DMI are addressed, and in particular, the in-plane DMI responsible for stabilizing bimerons. Through symmetry analysis, we demonstrate the necessary crystal symmetry to host in-plane DMI in a ferromagnet even in the absence of interfacial effects and also propose a few potential material candidates where we would observe the same.

3.6.1 DMI tensor form

In the most general form, the DMI contribution to the free energy can be written as

$$\mathcal{E}_{DM}[\boldsymbol{m}] = D_{ijk} m_i \partial_j m_k, \tag{3.8}$$

where $\hat{D}$ is a third-rank antisymmetric polar tensor.[166]. The $\mathcal{E}_{DM}$ is linear with respect to the first spatial derivatives of $\boldsymbol{m}$, but is not necessarily expressed in terms of Lifshitz invariants. [1].

The question that we want to address is, "What is the relationship between the symmetry of the crystal structure and the physical effect on the crystal due to a specific physical cause?" The answer lies in an old article by Neumann from 1833. According to Neumann's principle[167], if a crystal is invariant with respect to certain symmetry operations, any of its physical properties must also be invariant with respect to the same symmetry operations, i.e., $\hat{D}$ tensor must be invariant under the action of all symmetry operations of the point group of the crystal.

A third rank tensor has the form of a 9×3 matrix divided into three

[1] In ferromagnets, DMI can be described in the continuum limit by so-called Lifshitz invariants[166], i.e., $\mathcal{L}_{ij}^{(k)}[\boldsymbol{m}] = m_i \partial_k m_j - m_j \partial_k m_i$

matrices of dimensions 3×3,

$$\begin{pmatrix} D_{xxx} & D_{xyx} & D_{xzx} \\ D_{xxy} & D_{xyy} & D_{xzy} \\ D_{xxz} & D_{xyz} & D_{xzz} \\ \\ D_{yxx} & D_{yyx} & D_{yzx} \\ D_{yxy} & D_{yyy} & D_{yzy} \\ D_{yxz} & D_{yyz} & D_{yzz} \\ \\ D_{zxx} & D_{zyx} & D_{zzx} \\ D_{zxy} & D_{zyy} & D_{zzy} \\ D_{zxz} & D_{zyz} & D_{zzz} \end{pmatrix}. \tag{3.9}$$

Under a symmetry operation R of a crystal point group, the components of the DMI tensor transforms as,

$$D_{i'j'k'} = R_{i'i} R_{j'j} R_{k'k} D_{ijk}. \tag{3.10}$$

Since, $\mathcal{R} \in \mathcal{G}$ crystal's point group, the tensor must be invariant under the transformation $\left(D'_{ijk} = D_{ijk}\right)$. This helps us in determining vanishing and non-vanishing elements of the tensor $\hat{D}$

3.6.2 Symmetry analysis

Now let us discuss how the nature of crystal symmetry determines the structure of the DMI tensor, in particular Néel and in-plane DMIs.

Owing to the antisymmetric nature of the DMI tensor, see Eq. 2.7, we obtain $D_{iii} = 0$ $(i = j = k)$ and $D_{iji} = 0$ $(i = k)$. With account of these identities, the 3rd rank DMI tensor has the form

$$\begin{pmatrix} 0 & 0 & 0 \\ D_{xxy} & D_{xyy} & D_{xzy} \\ D_{xxz} & D_{xyz} & D_{xzz} \\ \\ -D_{xyy} & -D_{xyy} & -D_{xzy} \\ 0 & 0 & 0 \\ D_{yxz} & D_{yyz} & D_{yzz} \\ \\ -D_{xxz} & -D_{xyz} & -D_{xzz} \\ -D_{yxz} & -D_{yyz} & -D_{yzz} \\ 0 & 0 & 0 \end{pmatrix} . \tag{3.11}$$

Mirror-plane symmetry

We shall now consider a specific example of crystal symmetry and determine the non-vanishing elements of the DMI tensor corresponding to that symmetry operation alone. Consider a mirror plane $\mathbf{m_y}$, normal to the $\hat{y}$ axis. The matrix representing this symmetry transformation can be written as

$$\mathcal{R}_{m_y} = \begin{pmatrix} 1 & 0 & 0 \\ 0 & -1 & 0 \\ 0 & 0 & 1 \end{pmatrix} . \tag{3.12}$$

The DMI tensor must be invariant under this symmetry transformation. Consideration of Eqs. (3.10) and (3.12) yields the following conclusions:

- Since $\mathcal{R}_{m_y}$ is diagonal, $\mathcal{R}_{ip} = \mathcal{R}_{jq} = \mathcal{R}_{kr} = 0$ when $i \neq p$, $j \neq q$, $k \neq r$. Hence: *D_{ijk} vanishes when $i \neq p$ or $j \neq q$ or $k \neq r$.*

- $\mathcal{R}_{ii}\mathcal{R}_{jj}\mathcal{R}_{kk} = -1$, when y appears an odd number of times in the indices (ijk), which implies $D_{ijk} = -D_{ijk}$, and therefore these coefficients must vanish. Thus:
  D_{ijk} vanishes when y appears an odd number of times in the indices (ijk).

- Assuming a thin film with thickness less than the exchange length, we

can assume uniform magnetization along the normal to the film ($\hat{z}$ axis), which implies $\partial_z m_i = 0$. Hence we have $D_{zzx} = D_{xzz} = 0$.

As a result, the only non-vanishing components of the DMI tensor are

$$D_{xxz} = -D_{zxx}, \quad -D_{zyy} = D_{yyz}, \quad D_{xyy} = -D_{yyx}.$$

Similar symmetry arguments can be made for the different symmetry operations belonging to all the 32 crystallographic point groups. Table. 3.2 gives the form of DMI tensor for all possible symmetries.

symmetry	LI-type terms
C_1	$\mathcal{L}^x_{xy}, \mathcal{L}^y_{xy}, \mathcal{L}^z_{xy}, \mathcal{L}^x_{zx}, \mathcal{L}^y_{zx}, \mathcal{L}^z_{zx}, \mathcal{L}^x_{yz}, \mathcal{L}^y_{yz}, \mathcal{L}^z_{yz}$
C_2	$\mathcal{L}^x_{xy}, \mathcal{L}^z_{xy}, \mathcal{L}^y_{zx}, \mathcal{L}^x_{yz}, \mathcal{L}^z_{yz}$
C_S	$\mathcal{L}^y_{xy}, \mathcal{L}^x_{zx}, \mathcal{L}^y_{yz}, \mathcal{L}^z_{zx}$
D_2	$\mathcal{L}^z_{xy}, \mathcal{L}^y_{zx}, \mathcal{L}^x_{yz}$
C_3, C_4, C_6	$\mathcal{L}^z_{xy}, \mathcal{L}^x_{zx}, \mathcal{L}^y_{zx}, \mathcal{L}^x_{yz}, \mathcal{L}^y_{yz}$
S_4	$\mathcal{L}^x_{zx}, \mathcal{L}^y_{zx}, \mathcal{L}^x_{yz}, \mathcal{L}^y_{yz}$
D_4, D_6	$\mathcal{L}^z_{xy}, \mathcal{L}^y_{zx}, \mathcal{L}^x_{yz}$
C_{2v}, C_{3v}, C_{4v}, C_{6v}, D_3	$\mathcal{L}^x_{zx}, \mathcal{L}^y_{yz}$
D_{2d}	$\mathcal{L}^y_{zx}, \mathcal{L}^x_{yz}$
T, O	$\mathcal{L}^y_{zx}, \mathcal{L}^z_{xy}, \mathcal{L}^x_{yz}$

Table 3.2: Lifshitz invariant terms allowed by the point group symmetries. Here $\mathcal{L}^k_{ij} = m_i \frac{\partial m_j}{\partial m_k} - m_j \frac{\partial m_i}{\partial m_k}$. For the point groups C_i, C_{2h}, D_{2h}, C_{4h}, D_{4h}, C_{3i}, D_{3d}, C_{3h}, C_{6h}, D_{3h}, D_{6h}, T_h, T_d, O_h, all the elements of the DMI tensor vanish. Hence its not possible to stabilize chiral textures in these systems by means of DMI. The complete tensor forms for each of these point group symmetries is given in Appendix. C

3.6.3 Monoclinic point group m

The point group m belonging to the monoclinic space group Cm contains a mirror symmetry m whose plane is normal to the unique axis b ($|a| = |c| \neq |b|$).

The structure of the DMI tensor for this symmetry was determined in Sec.3.6.2,

$$\begin{pmatrix} 0 & 0 & 0 \\ 0 & D_{xyy} & 0 \\ D_{xxz} & 0 & D_{xzz} \\ 0 & -D_{xyy} & 0 \\ 0 & 0 & 0 \\ 0 & D_{yyz} & 0 \\ -D_{xxz} & 0 & -D_{xzz} \\ 0 & -D_{yyz} & 0 \\ 0 & 0 & 0 \end{pmatrix}, \tag{3.13}$$

and the corresponding energy density can be written as

$$\begin{aligned} \mathcal{E}_{DMI}^{Cm} = & D_{xyy}\left(-m_y\partial_y m_x + m_x\partial_y m_y\right) + D_{zxx}\left(m_z\partial_x m_x - m_x\partial_x m_z\right) \\ & + D_{yyz}\left(-m_z\partial_y m_y + m_y\partial_y m_z\right) + D_{zzx}\left(m_z\partial_z m_x - m_x\partial_z m_z\right). \end{aligned} \tag{3.14}$$

If the thickness of the thin film, grown along the direction of the unique axis b, is of the order of the exchange length, we can assume that the magnetization is uniform along this direction. In what follows, we adjust the crystallographic frame of reference so that the z direction points towards the unique axis. Hence, the DMI energy density for this point group, $\mathcal{E}_{DMI}^{m}$, reads

$$\begin{aligned} \mathcal{E}_{DMI}^{m} = & D_{xyy}\left(-m_y\partial_y m_x + m_x\partial_y m_y\right) + D_{zxx}\left(m_z\partial_x m_x - m_x\partial_x m_z\right) \\ & + D_{yyz}\left(-m_z\partial_y m_y + m_y\partial_y m_z\right) \qquad (3.15) \\ = & \quad D_{xyy}\mathcal{L}_{xy}^{y} + D_{zxx}\mathcal{L}_{zx}^{x} + D_{yyz}.\mathcal{L}_{yz}^{y} \qquad (3.16) \end{aligned}$$

We note in passing that the expressions Eqs. (3.2) and (3.4) for the Néel and in-plane DMI energy densities, respectively, can be rewritten in terms of Lifshitz invariants as,

$$\begin{aligned} \mathcal{L}_{\text{Néel}}[\boldsymbol{m}] &= D_{zxx}\mathcal{L}_{zx}^{x} + D_{yyz}\mathcal{L}_{yz}^{y} \\ \mathcal{L}_{\text{in-pl}}[\boldsymbol{m}] &= D_{zxx}\mathcal{L}_{zx}^{x} + D_{xyy}\mathcal{L}_{xy}^{y}. \end{aligned} \tag{3.17}$$

Comparison of Eqs. (3.16) and (3.17) allow us to conclude that the monoclinic point group m hosts both Néel and in-plane DMI in the system. In particular, the first two and the last two terms in Eq. (3.16) stabilize in-plane skyrmions and Néel skyrmions, respectively.

Based on *ab initio* calculations [168], the following materials are predicted to exhibit the Cm space group symmetry.

- $Fe(BRh_2)_3$,$Co(BRh_2)_3$
- $Al_{18}Co_5Ni_3$
- $Rb_6Fe_2O_5$
- La_4TaCo_{33}
- $Co_{25}Cu_{11}O_{48}$
- $FeLa_3S_6$
- $Ta_{12}Co_3Pt_3Se_{32}$
- $Li_4Fe_3Ni_3(TeO_8)_2$

Among these, $FeLa_3S_6$ [169] and $Rb_6Fe_2O_5$ [170] have been previously reported to be synthesized in bulk systems and are the most promising platforms for observing in-plane skyrmions. One could stabilize in-plane skyrmions in the materials mentioned above. Therefore, it is crucial to 1) investigate the stability of in-plane skyrmions in magnetic systems within the point group m and 2) understand the effects of the competing DMI interactions that emerge in these materials.

3.7 The Cm Model

The symmetry analysis in Sec. (3.6) revealed that in-plane skyrmions could be stabilized in a crystal with Cm symmetry. In this section, we now explore the energetics and stability of the in-plane skyrmions in above said symmetry. Rewriting the micromagnetic energy functional (Eq. (3.1)) for this system, which accommodates both DMI interactions ($D_{\text{Néel}},\ D_{\text{in-plane}}$) stabilizing an in-plane skyrmion,

$$\mathcal{E}_{\text{Cm}}[\boldsymbol{m}] = \int_{\mathcal{S}} d^2\boldsymbol{r}\ \left\{ \frac{A}{2}\left(\nabla \boldsymbol{m}\right)^2 + K\left(1 - m_z^2\right) + D_{Cm}\ \mathcal{L}_{Cm}[\boldsymbol{m}] - \boldsymbol{m}\cdot\left(\boldsymbol{H} + \boldsymbol{H}_d\right) \right\}, \tag{3.18}$$

where $\mathcal{L}_{\text{Néel}}[\boldsymbol{m}]$ and $\mathcal{L}_{\text{in-pl}}[\boldsymbol{m}]$ are the Lifshitz invariants that models the Néel and in-plane DMI interactions, respectively, and are defined in Eqs. (3.2) and (3.4), respectively, in terms of the spatial variations of the magnetization.

The nonzero coefficients of the DMI tensor for Cm symmetry[2] are $D_{xxz} = -D_{zxx}$, $D_{yyz} = -D_{zyy}$, and $D_{yyx} = -D_{xyy}$. Hence, the DMI energy contribution in Eq. (3.4) can be cast in the form,

$$\mathcal{E}_{\text{DMI}}[\boldsymbol{m}] = \left\{ D_{xyy}\ \mathcal{L}_{\text{Néel}}[\boldsymbol{m}] +\ D_{xyy}\ \mathcal{L}_{\text{in-pl}}[\boldsymbol{m}] +\ D_3(m_z\partial_x m_x - m_x\partial_z m_z) \right\}, \tag{3.19}$$

where $D_3 = D_{zxx} - D_{xyy}D_{zyy}$. To understand the physical consequences of having two competing DMIs, let us consider the nature of the domain wall in Néel and in-plane skyrmions. In a Néel skyrmion [Fig. (3.2b)], taking the cross-section of magnetization along any radial direction $\hat{r}$ indicates a domain wall in which the magnetization rotates in the $\hat{r} - \hat{z}$ plane (Néel domain wall). However, in an in-plane skyrmion the nature of the domain varies as we go along the circumference of the skyrmion. The domain along the $\hat{x}$ and $\hat{y}$-directions have magnetization varying along $\hat{x}-\hat{z}$ and $\hat{x}-\hat{y}$ planes, respectively (see Fig. 3.2), and along any radial direction in $\hat{x}-\hat{y}$ plane, the magnetization is of Bloch nature (has rotation out of the plane of propagation). This already

[2] see Sec. (3.6) for details of this tensor evaluation.

gives an initial picture as to how the symmetries are different in the two cases. Now when we consider a Cm system having competing Néel and in-plane DM interactions, the cylindrical symmetry of the skyrmion is broken. The degree of asymmetry depends on the ratio of the strengths of the two DM interactions. This gives rise to interesting new features in current-driven dynamics and also magnonic excitations of in-plane skyrmions in Cm crystal. We shall describe these in detail in the following sections.

3.7.1 Axial asymmetry in Cm model

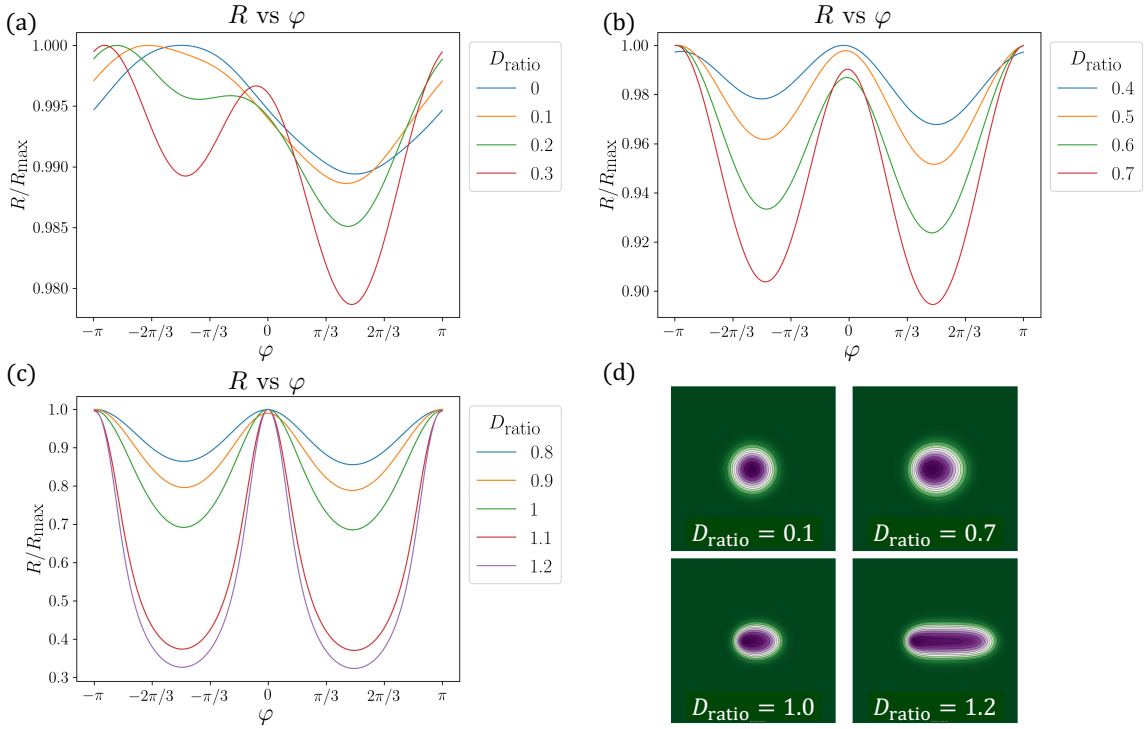

Figure 3.11: Axial asymmetry in Cm model. (a-c) Size of the in-plane skyrmion as a function of the azimuthal angle φ for different values of D_{ratio}. The skyrmions are stabilised within the Cm model hosting two DMI interactions. (Eq. (3.18)). The asymmetry in the skyrmion radius profile becomes more pronounced as the strength of Néel DMI increases. (d) Magnetization density plots for different values of D_{ratio} for a fixed value of $D_{\text{in-pl}}$. It can be seen from the contours that the cylindrical symmetry is broken for nonzero values of D_{ratio}. The magnetization density profiles for each D_{ratio} values in (a-c) are presented in the Appendix.. A.

Now that we have obtained a physical intuition for axial asymmetry in Cm model, let us describe it quantitatively and also study the effect of asymmetry on shape of skyrmions. The effective fields due to different DMI contributions can be written as follows,

$$\boldsymbol{B}_{Cm} = -\frac{2}{M_s}\begin{pmatrix} (D_{\text{Néel}} + D_{\text{in-pl}})(\partial_x m_z) - D_{\text{in-pl}}(\partial_y m_y) \\ -D_{\text{Néel}}(\partial_y m_z) - D_{\text{in-pl}}(\partial_y m_x) \\ (D_{\text{Néel}} + D_{\text{in-pl}})(\partial_x m_x) + D_{\text{Néel}}(\partial_y m_y) \end{pmatrix}. \tag{3.20}$$

It is evident from the above expression for the DMI field that, the presence of Néel DMI in the in-plane system adds additional rotation of the magnetization in $\hat{r} - \hat{z}$ plane. This breaks the cylindrical symmetry in the plane leading to the deformation of the skyrmion shape.
We observe this deformation by plotting the angular dependence of the radius of the in-plane skyrmion as a function of $D_{\text{Néel}}$ (see Fig. 3.11), where the radius $R(\varphi)$ being defined by the condition $m_x[R(\varphi), \varphi] = 0$ (i.e., the position at which m_x vanishes) and φ denoting the azimuthal angle. In Fig. 3.11(a), the variation in the radius for the case of $D_{\text{ratio}} = 0$ is arising due to discretisation of the lattice during simulations, and as such, we see that the variation is less than 0.1%. As we increase the relative strength of the DM interaction, D_{ratio} (we define the relative strength as the ratio of the two DMIs, i,e., $D_{\text{ratio}} = D_{\text{Néel}}/D_{\text{in-pl}}$), we observe oscillations in R when φ is swept within the range $[0, 2\pi]$. The variation of radius of the in-plane skyrmion is such that it goes from a maximum to a minimum value as φ zero to $\pi/2$. This is due to the extra twisting we attain in the $\hat{x} - \hat{z}$ plane, which we can see from the extra term D_3 in DM energy contribution[Eq. (3.19)]. When the relative strength D_{ratio} goes beyond value 1, the terms with D_3 in Eq. (3.19) are very dominating, thereby leading to the elliptical deformation of in-plane skyrmions.(as shown in Fig. 3.11(c,d))

3.7.2 In-plane skyrmions stability

The basic properties of isolated Néel skyrmions in PMA magnets have been investigated thoroughly in a number of earlier contributions [95, 165, 171, 172]. However, there are not many investigations into the properties of isolated

in-plane skyrmions, which are fundamental to understanding their physics and applications in potential spintronic devices. The symmetry analysis from Sec. 3.6.2 revealed that the monoclinic system Cm is the only space group compatible with the symmetries to host in-plane skyrmions (see Table. 3.2). In this section, we will study different magnetic phases in Cm model parameterized by the two Dzyaloshinskii coupling constants D^y_{xy} and D^y_{zy} followed by which we shall construct a mean-field phase diagram and study the stability of in-plane skyrmions as meta-stable states over the ferromagnetic background.

First off, let us start by rewriting the Eq. (3.20) in a reduced unit system by introducing a dimensionless variable $\vec{\rho} = \vec{r}/\sqrt{A/K}$, which yields

$$\mathcal{E}_{\mathrm{Cm}}[\boldsymbol{m}] = A\int_{\mathcal{S}} d^2\vec{\rho}\Big\{\frac{1}{2}(\vec{\nabla}_\rho \boldsymbol{m})^2 + [1-(m_x)^2] + \frac{4g_1}{\pi}\mathcal{L}_{\text{in-pl},\rho}[\boldsymbol{m}] + \frac{4g_2}{\pi}\mathcal{L}_{\text{Néel},\rho}[\boldsymbol{m}]\Big\}, \tag{3.21}$$

where $g_1 = \pi D_{xyy}/4\sqrt{AK}$ and $g_2 = \pi D_{zyy}/4\sqrt{AK}$ are the two dimensionless reduced Dzyaloshinskii coupling constants, and the subscript 'ρ' indicates partial derivation with respect to $\vec{\rho}$. The advantage of working in the reduced system of units is that now, we have only two dimensionless coupling constants that parameterize the stability of chiral structures in the Cm model. The dimensionless variable $\vec{\rho}$ rescales the space by 1D domain wall width $\sqrt{A/K}$, which results in the reduced coupling constants infront of two DMI terms. In the case of a single DMI in the model (Eqs. 3.1, 3.3), this rescaling of units could also be performed by the spin spiral length $2A/D$ giving us a single reduced anisotropy constant $2AK/D$ in the reduced system.

Let us consider a spin frame of reference spanned by the basis vectors $\{\hat{\boldsymbol{e}}_1, \hat{\boldsymbol{e}}_2, \hat{\boldsymbol{e}}_3\}$ such that the normal to the plane of the helix is defined as,

$$\hat{\boldsymbol{e}}_3 \equiv \vec{n} = (\cos\phi\sin\theta, \sin\phi\sin\theta, \cos\theta)^\top, \tag{3.22}$$

and the pitch vector $\vec{q} \neq \vec{0}$, as shown in Fig. 3.12. Now we can write the generic helical ansatz in real space by casting the magnetization field in the

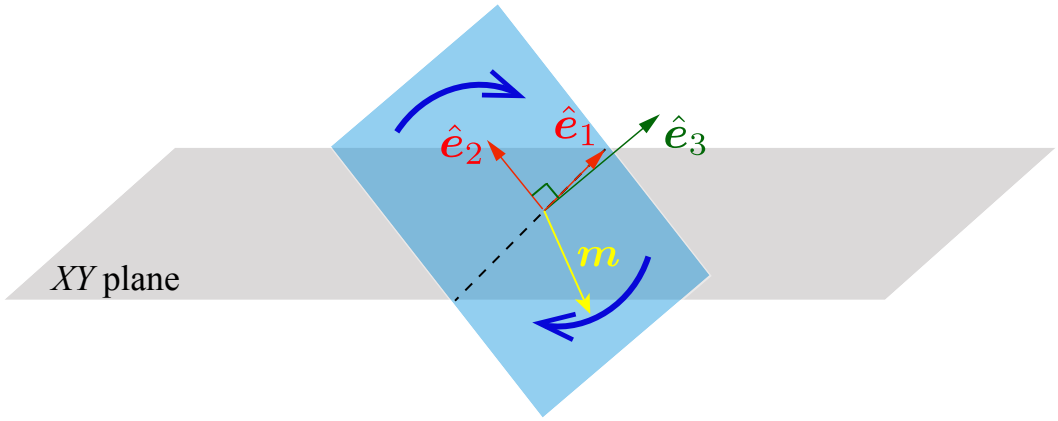

Figure 3.12: Figure illustrating the spin frame of reference spanned by the basis vectors $\{\hat{\boldsymbol{e}}_1, \hat{\boldsymbol{e}}_2, \hat{\boldsymbol{e}}_3\}$. In this spin space geometry, the vector $\hat{\boldsymbol{e}}_3$ is aligned parallel to the normal of the plane containing the generic helix.

above defined spin frame of reference adjusted to the normal to the plane, $\vec{n}$,

$$\boldsymbol{m}(\vec{r}) = \cos(\vec{q}\cdot\vec{r})\hat{\boldsymbol{e}}_1 + \sin(\vec{q}\cdot\vec{r})\hat{\boldsymbol{e}}_2 + m_0\hat{\boldsymbol{e}}_3, \tag{3.23}$$

where m_0 denotes the out-of-plane projection of the magnetization. This projection distinguishes between pure helical phase and conical phases, which shall be shown later. By plugging the ansatz Eq. (3.23) into Eq. (3.21), we obtain the following expression for the total energy density:

$$\begin{aligned}\varepsilon\big[\boldsymbol{m}(\vec{r})\big] = &\frac{1}{2}\frac{\vec{q}^{\,2}}{1+m_0^2} + \frac{4}{\pi}\frac{g_1}{1+m_0^2}\left(q_y\cos\theta + q_x\sin\theta\sin\phi\right)\\ &+ \frac{4}{\pi}\frac{g_2}{1+m_0^2}\left(q_x\sin\theta\sin\phi - q_y\sin\theta\cos\phi\right)\\ &+ \frac{\frac{1}{2}+m_0^2}{1+m_0^2} + \frac{\frac{1}{2}-m_0^2}{1+m_0^2}\sin^2\theta\cos^2\phi.\end{aligned} \tag{3.24}$$

The energy density is parameterised by variables $\{\theta, \phi, \vec{q}, m_0\}$. The different ground states can be obtained by extremalization of the energy density functional (3.24) w.r.t these parameters. Extremalization of the energy density functional (3.24) yields the equations for the pitch vector ($\vec{q}$) and the value

(m_0) for the out-of-plane magnetization.

$$q_x = -\frac{4}{\pi}(g_1 + g_2)\sin\theta\sin\phi, \tag{3.25}$$

$$q_y = \frac{4}{\pi}\left(g_2\sin\theta\cos\phi - g_1\cos\theta\right), \tag{3.26}$$

$$m_0 = 0. \tag{3.27}$$

Extremalization of the energy density functional w.r.t the polar angle (θ) yields the following conditions

$$\theta = 0, \pi \qquad \text{or} \tag{3.28}$$

$$\delta g_1 g_2\left[2g_1g_2 - \frac{16}{\pi^2}\delta^2\right]\cos 2\theta\cot\theta - \delta^3\cot\theta + g_1^2 g_2^3(2g_1 + g_2)\sin 2\theta = 0, \tag{3.29}$$

where $\delta \equiv g_1^2 + 2g_1g_2 + \pi^2/16$.

In the case when $\theta = 0, \pi$, using Eqs. (3.25 - 3.27) the resultant magnetic texture can be written as,

$$\boldsymbol{m}(\vec{r}) = \pm\left(\cos[4g_1y/\pi], -\sin[4g_1y/\pi], 0\right)^\top, \tag{3.30}$$

which represents purely a helical phase with pitch vector along y-axis in the XY plane (see Fig. 3.12). The corresponding total energy density becomes,

$$\varepsilon = \frac{1}{2}\left[1 - \frac{16g_1^2}{\pi^2}\right]. \tag{3.31}$$

In the case of other extrema (Eq. (3.29)), the following condition for the azimuthal angle is obtained.,

$$\cos\phi = -\frac{g_1^2 + 2g_1g_2 + \pi^2/16}{g_1g_2}\cot\theta. \tag{3.32}$$

The resulting magnetization field is now parameterized by the polar and azimuthal angles obtained from the solutions of Eqs. (3.29, & 3.32) from which from which the corresponding total energy density can be calculated by means

of Eq. (3.24). This solution represents a mixture of helical and conical phases. Whether any of these solutions correspond to the ground state of the system can be determined by comparing their energy density (3.24) to that of the uniform magnetic state ($\varepsilon\big[\boldsymbol{m}_u(\vec{r})\big] = 0$).

The phase diagram of a thin monoclinic Cm system is constructed as a function of the two reduced Dzyaloshinskii coupling constants g_1 and g_2, by calculating the minimum energy solution in each case. The resultant phase diagram is shown in Fig. 3.13. We observe that three notable phases, viz., a ferromagnetic phase, a helical phase, and within the ferromagnetic phase, a region where single in-plane skyrmions exist as metastable states. It should be noted here that only the ferromagnetic phase and helical phases are the minimum energy solutions, and isolated in-plane skyrmions always emerge as low-energy excitations on the uniform magnetic background. The two phases (helical and ferromagnetic) are separated by a linear boundary which has been calculated analytically from the minimum energy solutions of the energy functional. In obtaining the analytical solutions, the term proportional to D_3 has been disregarded in our analysis since it is only responsible for the elliptical shape deformation of the Cm skyrmions. The stability of the in-plane skyrmions as metastable states depends on the interplay between Néel and in-plane DM stabilizers.

The blue region shaded in the phase diagram (Fig. 3.13) was obtained by Micromagnetic simulations performed in Mumax3[112] in a square geometry of lateral size 256 nm and thickness 1 nm, with cell size $1\times1\times1$ nm^3 disregarding dipolar interactions. The skyrmion phase was calculated by sweeping g_1 and g_2 within the range $0-0.7$ and checking whether an initial single in-plane skyrmion configuration relaxed towards the uniform state or not. The limited span of the skyrmion phase inside the ferromagnetic phase is a computational limitation due to the fact that at low g_1 values, the in-plane skyrmion size is not more than a few discretisation cells, and the relaxation algorithm collapses into a uniform state. The values for the micromagnetic parameters are given in Table 3.3.

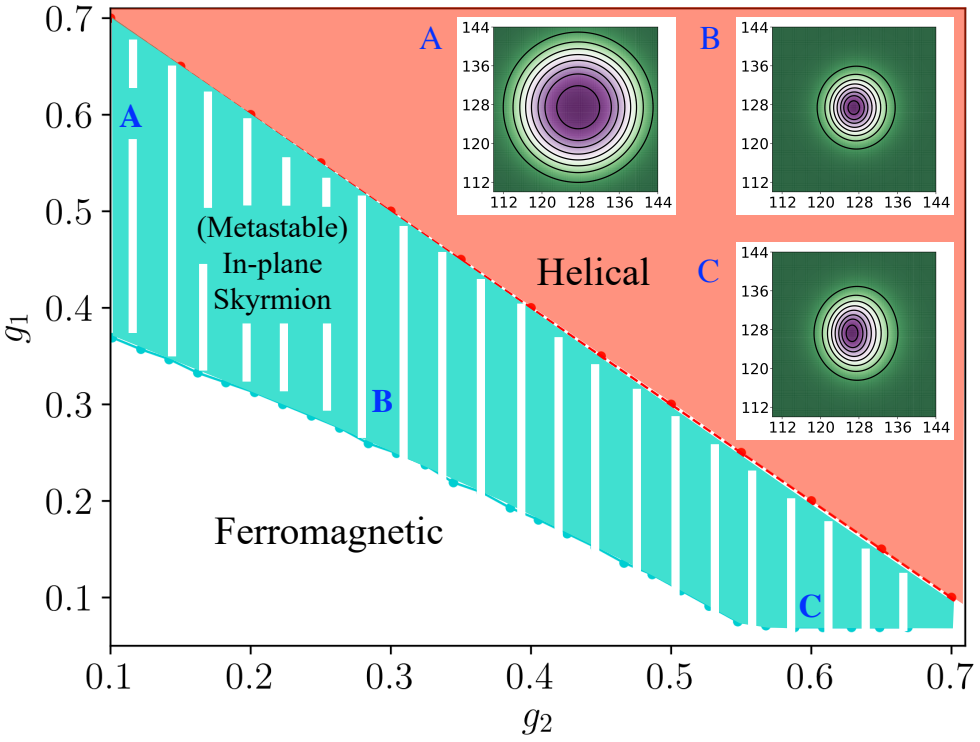

Figure 3.13: Phase diagram of a monoclinic Cm magnet as a function of the in-plane (g_1) and interfacial (g_2) reduced Dzyaloshinskii coupling constants. The boundary between the ferromagnetic phase and the helical phase is indicated by a red dashed line. Within the ferromagnetic phase, there exists a region where metastable isolated in-plane skyrmions can be found, marked in light blue. Insets corresponding to points A, B, and C in the phase diagram showcase examples of skyrmion shapes. Additionally, it is observed that increasing the strength of the interfacial Dzyaloshinskii coupling constant deforms the skyrmion. [Figure and caption adapted from [82].]

A (J/m)	K (J/m^3)	α	M_s (A/m)	g_1	g_2
$1.5 \cdot 10^{-11}$	$5.0 \cdot 10^5$	0.15	$5.8 \cdot 10^5$	variable	variable

Table 3.3: Values of the micromagnetic parameters utilized in the simulations of skyrmion relaxation for the phase diagram.

3.7.3 Conclusion

In this chapter, we introduced the in-plane micromagnetic model to describe the in-plane skyrmions and did a comparative study with Néel skyrmions. Through micromagnetic simulations, we analyze the equivalence of in-plane and Néel skyrmions in the absence of stray fields and their differences in the presence of stray fields. Furthermore, we perform symmetry analysis, look at the compatible crystallographic space groups to host in-plane DMI, and propose material candidates for their observations. Following the results of the symmetry analysis, we studied the stability of in-plane skyrmions in a monoclinic system Cm in a wide range of the phase diagram parameterized by the two DMI constants.

Chapter 4

Production of in-plane skyrmions [1]

Magnetic skyrmions have promising potential for future spintronic applications as non-volatile information carriers in magnetic media at ultra-low currents. As such, a method for efficient creation (writing) and destruction (deleting) of skyrmions is required for any skyrmion-based applications. In this chapter, we demonstrate that in-plane skyrmions can be created on a thin-film in-plane magnet by using two different methods, namely blowing magnetic bubbles method and shedding skyrmions via an inhomogeneity. These methods have already been established for conventional Néel skyrmions and work very well for in-plane skyrmions as well. Blowing magnetic bubbles involves the production of skyrmions by blowing a domain-wall pair through a geometric constriction using an in-plane current. The second method involves a controlled shedding of skyrmions from a spatially local magnetic inhomogeneity using spin-transfer torques.

[1] Adapted from: R. Zarzuela, V. K. Bharadwaj, K-W. Kim , J. Sinova, and K. Everschor-Sitte, Phys. Rev. B. **101** 054405 (2020).

4.1 Introduction

Skyrmion based devices require efficient and reliable methods for the creation and destruction of skyrmions. For instance, information can be encoded in the distance between skyrmions moving along a nanostrip in future magnetic data storage devices [70]. Hence it is important to establish methods that can create (destroy) skyrmions within an intended area for successful binary storage applications. Over the last decade, a plethora of theoretical models and experiments have been reported for the creation of skyrmions using several kinds of external stimuli, viz. magnetic field [98, 173–175], spin-polarized electric current [67, 71, 134, 176, 177], ultrafast laser pulses [178–180]. The current status and challenges in writing, deleting, and reading magnetic skyrmions research can be found in recent reviews [115, 181, 182]. In this work, we focus on two methods to demonstrate the creation of in-plane skyrmions namely, (blowing magnetic bubbles [44] and shedding skyrmions via an inhomogeneity [66]). The former method relies on the formation of skyrmions when a DW pair exits a narrow constriction and while the latter uses spin polarized electric currents induced instability locally at an inhomogeneity for the creation of in-plane skyrmions. These two methods have been previously demonstrated for Néel skyrmion in thin films with perpendicular magnetic anisotropy.

4.2 Blowing in-plane skyrmions

The current induced motion of domain walls using spin-transfer torques or spin–orbit torques has been studied extensively. Novel ideas that use spin-polarized electric currents as a driving force for magnetization dynamics have been proposed theoretically and realized experimentally for high-efficiency and low-dissipation spintronic memory devices, such as magnetic racetrack memory [38, 39]. Conventionally, magnetic race track memory proposed by Parkin *et al.*, [39] relies on controlled DW movement using spin-polarized currents. It is well understood that spin polarized currents can also move skyrmions. As a consequence, skyrmion based race track memory devices can be realized as an alternative [70, 75].

Zhou *et al.*, [177] proposed a conversion mechanism to create skyrmions from

DW pair at a constriction geometry [177]. Later in 2015, Jiang *et al.*, [44] reported observation of skyrmions in a magnetic trilayer ($Ta/Co_{20}Fe_{60}B_{20}/TaO_x$) using inhomogeneous spin-orbit torques at the geometric constriction (Fig. 4.1). The experiment shows (using MOKE) the formation of skyrmions upon moving a stripe domain through a geometrical constriction. A spin-polarised electric current was used to set the stripe domain into motion along the narrow constriction. This demonstration draws an intriguing analogy with the formation of soap bubbles when a soap film pinched off upon blowing air through a straw or a bubble wand [44]. The divergent current distribution at the geometrical constriction generates inhomogeneous spin hall forces on the stripe domains causing them to expand radially. Consequently, as the stripe domains exit the constriction, surface tension in the DWs of stripe domains breaks the stripes into skyrmion bubbles. It should be noted that the mechanism of skyrmion formation in the experiment differs from Zhou *et al.*, [177]. Following Jiang *et al.*, [44], Heinonen *et al.*, [63] , Lin *et al.*, [183], and Liu *et al.*, [158] independently investigated the mechanism of creation of skyrmion bubbles using inhomogeneous spin hall torques. The results were shown to be consistent with the experimental observations. Motivated by blowing skyrmion bubbles experiments [44], in this section, we investigate the production of in-plane skyrmions in a similar manner to that of Néel skyrmions.

4.2.1 Simulation setup

The constriction geometry used in micromagnetic simulations, as shown in Fig. 4.2 consists of a thin magnetic film of dimensions $800\times100\times1$ nm^3 with a narrow constriction of dimensions $128\times32\times1$ nm^3 at its center. The width of the constriction, which affects the generation of skyrmions, will be discussed later. Two gold strips of dimensions $4\times32\times1$ nm^3 located at the edges of the thin film serve as metal contacts for applied voltage. The material parameters used for the simulations: the saturation magnetization $M_s = 5.8\times10^5$A/m, the exchange constant $A = 3.0\times10^{-11}$J/m, the perpendicular anisotropy constant $K = 3.0\times10^5$J/m^3 and the DMI constant $D = 2.5\times10^{-3}$J/m^2. It should be noted that the anisotropy is along the $\hat{x}$-axis to favor in-plane orientation of the magnetization. The geometry is discretized into $(1\times1\times1)$nm^3 mesh. The micromagnetic simulations have been performed using Micromagnum with

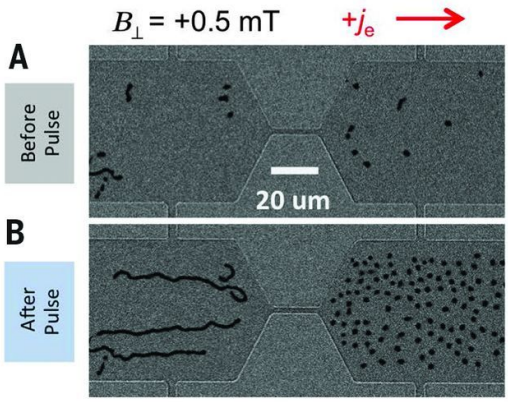

Figure 4.1: **Experimental generation of magnetic skyrmions**. (A) Sparse irregular domain structures are observed at both sides of the device at a perpendicular magnetic field. (B) Upon passing a current of through $j_e = 5 \times 10^5 \mathrm{A/cm}^2$ the device, the left side of the device develops predominantly elongated stripe domains, whereas the right side converts into dense skyrmion bubbles. The disordered stripe domains are forced to pass through the constriction and are eventually converted into skyrmions at the right side of the device

current-solver extensions to directly solve for the current flow, taking into account the geometry and magnetization in the sample [111].

4.2.2 In-plane skyrmions generation

The initial magnetization is set to a DW pair inside the constriction, which was allowed to relax freely with Gilbert damping constant $\alpha = 0.3$ (see Fig. 4.2). We then apply a voltage U across the gold contacts, and the charge-current density is calculated self-consistently based on an Anisotropic magnetoresistance effect (AMR) module [184]. [2] [3] The current density $\boldsymbol{j}[U, \boldsymbol{m}]$ depends on

[2]The anisotropic magnetoresistance (AMR) effect is a the phenomenon in which the electrical resistivity depends on the relative orientation between the magnetization direction and the charge-current direction. This effect leads to different resistivities for currents that are perpendicular ($\rho_\perp$) or parallel $\rho_\parallel$ to the magnetization. The AMR coefficient/efficiency is defined as $\frac{\Delta\rho}{\rho_0} = \frac{\rho_\parallel \rho_\perp}{\Delta\rho_0}$ where ρ_0 is the resistivity at zero field.

[3]In the following simulations we assume the AMR to be zero and consider a constant value for the conductivity ($\sigma = 5 \times 10^6 \mathrm{S/m}$).

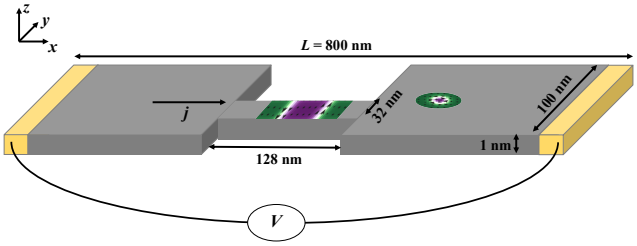

Figure 4.2: Sketch of the geometrical setup used in the micromagnetic simulations for the skyrmion(green-white disk) generation from a DW pair (green-purple rectangle inside the constriction) via "Blowing magnetic Bubbles" method.

the magnetization through the conductivity tensor $\boldsymbol{\sigma}[\boldsymbol{m}]$ given by the relation

$$\boldsymbol{j}[U, \boldsymbol{m}] = -\boldsymbol{\sigma}[U, \boldsymbol{m}] \cdot \boldsymbol{E}[U] \tag{4.1}$$

The applied voltage U generates a non-uniform electric field $\boldsymbol{E}$ near the constriction. The Poisson equation $\nabla^2\phi = 0$ is solved at each time step with the boundary conditions $\phi|_{left} = -\phi|_{right} = U$. The current density is obtained from $\boldsymbol{j} = -\hat{\sigma}\nabla\phi$. The spatial profile of the current density obtained for our geometry is shown in Fig. 4.3. The magnetization dynamics in the presence of STT are described by the Landau-Lifshitz-Gilbert (LLG) equation

$$\begin{aligned}\partial_t \boldsymbol{m} = &-\gamma\ (\boldsymbol{m} \times \boldsymbol{H}_{\text{eff}}) + \alpha\ (\boldsymbol{m} \times \partial_t \boldsymbol{m}) \\ &+ \zeta \boldsymbol{m} \times (\vec{j} \cdot \vec{\nabla})\boldsymbol{m} - \zeta\beta\, \boldsymbol{m} \times \Big(\boldsymbol{m} \times (\vec{j} \cdot \vec{\nabla})\boldsymbol{m}\Big)\end{aligned} \tag{4.2}$$

where $\boldsymbol{H}_{\text{eff}} = -\frac{1}{M_s}\delta_{\boldsymbol{m}}\mathcal{E}_{\text{in-pl}}[\boldsymbol{m}]$ is the effective magnetic field acting on the magnetization $\boldsymbol{m}$, α is the Gilbert damping constant, and γ denotes the gyromagnetic ratio. The interaction between spin-polarized currents and the magnetic texture is modeled by the adiabatic (3^{rd} term) and non-adiabatic spin-transfer torques (4^{th} term) [128]. Here, $\zeta = \gamma P\hbar/2eM_s$ is the charge-to-spin conversion factor in the adiabatic regime, P represents the electron spin polarization, β parameterizes the strength of the non-adiabatic torque. The effective magnetic field $\boldsymbol{H}_{\text{eff}}$ acting on the local magnetization includes the contribution from the exchange, DMI, PMA, stray fields, and the applied magnetic fields (see Eq. 3.3).

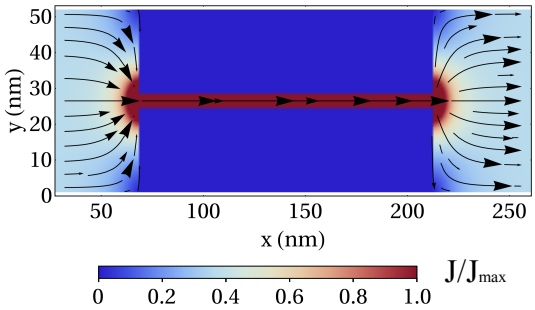

Figure 4.3: The spatial profile of the current density obtained through a self-consistent calculation with constant-voltage boundary conditions.The colorscale in the figure is normalized with respect to $J_{\max}$ where, $J_{\max} = 2\phi|_{\text{left}}/L$ denotes the maximum current injected into the sample of length L.

Snapshots of the skyrmion generation process at different time intervals are shown in Fig. 4.4 (left panel: m_x, and right panel: topological charge density ρ_{sky}). Applying voltage U across the contacts generates a spin-polarized current which begins to move the DW pair in the constriction. As the DW pair exits the constriction, the portion of the DW first exposed to the area outside the constriction begins to expand radially. Following this, as the second DW is expelled from the constriction, it detaches completely and transforms continuously into an in-plane skyrmion. The mechanism of in-plane skyrmion generation can be clearly understood by tracking the temporal evolution of the skyrmion charge Q calculated at every time step of the simulation by integrating the skyrmion charge density ρ_{sky} (see Fig. 4.5). We observe that the topological charge Q remains zero for the DW pair until it reaches the end of the channel (time t_{d0}). As the right DW begins to exit the channel, the Q increases until time t_{d1}, which corresponds to the left DW detaching from the constriction (see right panel of Fig. 4.4). As the left DW expands radially outside the constriction owing to the Magnus force, the skyrmion charge decreases monotonically until t_{d2}. Once the texture formed outside the channel completely detaches at time t_{sky}, it transforms smoothly into an in-plane skyrmion which yields in a sharp increase of Q until it reaches value of $Q \approx 1$. The corresponding snapshots of the magnetization are shown in Fig. 4.4.

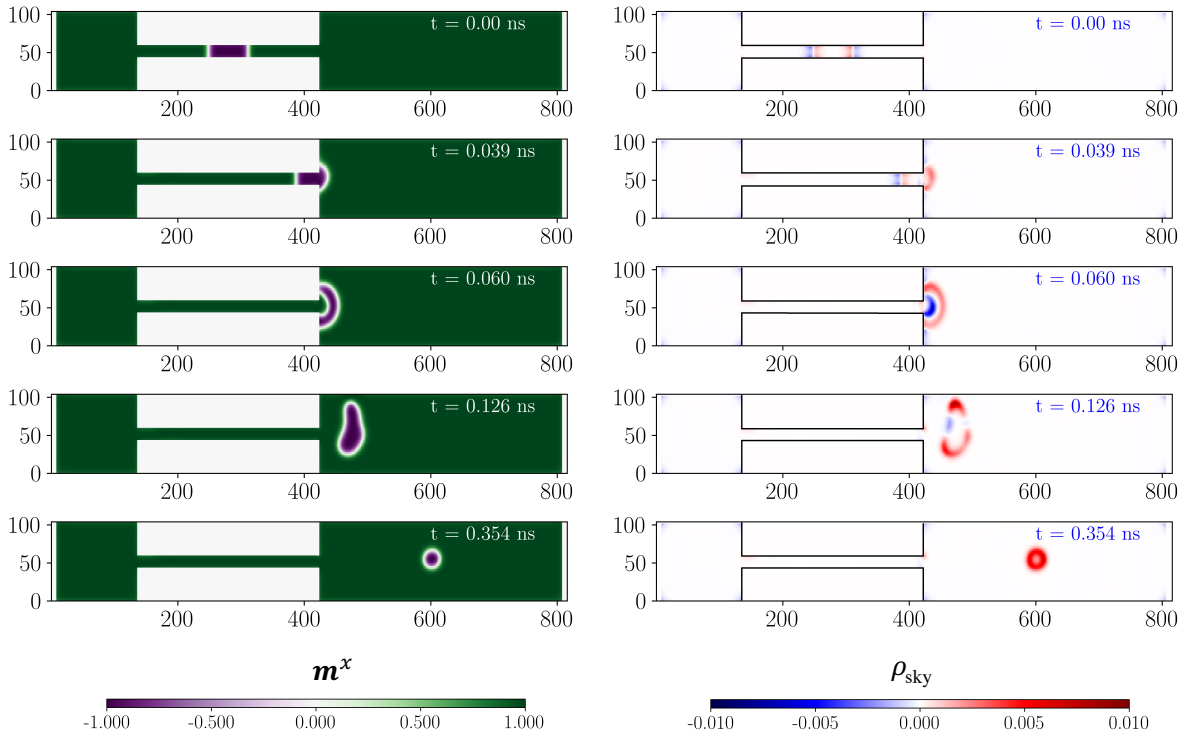

Figure 4.4: Generation of in-plane skyrmions via the current-driven motion of a DW pair through a narrow geometrical constriction. The left panel presents sequential snapshots of x-component of the magnetization, m_x, taken at five sequential times. On the right panel, the corresponding time evolution of the skyrmion charge density, ρ_{sky}, is shown for the magnetization texture depicted in the left panel. The color code represents the m_x component of the magnetization. [Figure and caption adapted from [82].]

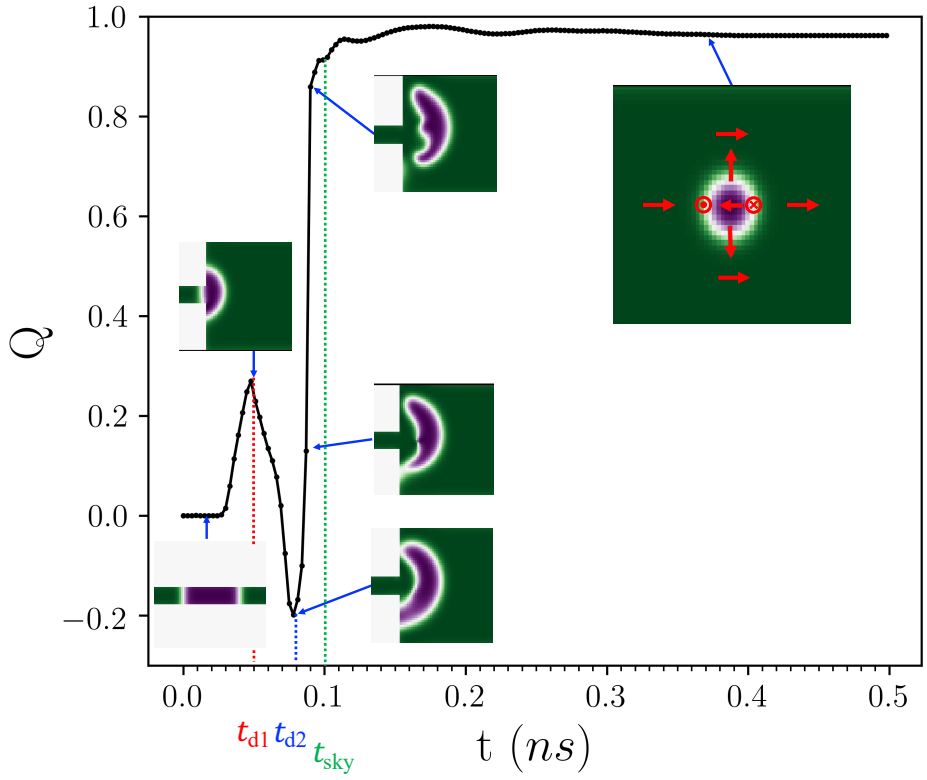

Figure 4.5: Temporal evolution of the topological charge for the production of in-plane skyrmions. In this simulation, corresponding to the geometry of Fig. 4.4, the values of the times t_{d1}, t_{d2} and t_{sky} (see Sec.4.2.2) are 0.04 ns, 0.08 ns and 0.17 ns respectively. The snapshots correspond to the magnetization at each of these times. [Figure and caption adapted from [82].]

4.3 Shedding via an inhomogeneity

In-plane skyrmions can also be generated by exploiting the interplay between homogeneous DC currents and magnetic impurities. Sitte *et al.*, theoretically predicted that DWs could be periodically produced in a magnetic nanowire via a mechanism physically relying on the static loss of stability [185]. This instability is induced by the interaction of spin-transfer torques and the pinning center. Later Everschor-Sitte *et al.*, [66] extended the mechanism to the periodic production of skyrmions by means of spatially inhomogeneous magnetization and homogeneous DC current [66]. It was also shown that the skyrmion-antiskyrmion pairs could be produced even in the absence of DMI. However, the presence of DMI stabilizes skyrmion/antiskyrmion depending on which is favored in the system. Using a similar mechanism, Büttner *et al.*, experimentally demonstrated a controllable nucleation of skyrmions by exploiting the defects on a magnetic racetrack using sub-nanosecond spin–orbit torque pulses [186]. By exploiting the same mechanism, we show that the in-plane skyrmions can be produced via an inhomogeneity akin to Néel case.

The simulation setup consists of a thin film with a pinning center creating a magnetic inhomogeneity as illustrated in Fig. 4.6. The magnetic inhomogeneity can be achieved experimentally by locally engineering the magnetic field, anisotropy, DMI, or other magnetic interactions. Here we create the pinning center by locally altering the magnetocrystalline anisotropy in a small region of the sample. Micromagnetic simulations were performed in MuMax3 [112] and MicroMagnum [111]. In our work, the simulated geometry is of dimensions $1024\times1000\times0.4$ nm^3 and with cells discretization $1\times1000\times0.4$ nm^3. The inhomogeneity is a cylinder with a radius 50 nm. The material parameters used for the simulations: the saturation magnetization $\mathrm{M_s} = 3\times10^5$A/m, the exchange constant $\mathrm{A} = 2.1\times10^{-11}$J/m, the perpendicular anisotropy constant $\mathrm{K} = 8.0\times10^4$J/m^3 and the DMI constant $\mathrm{D} = 1.2\times10^{-3}$J/m^2. The anisotropy at the pinning center is set along $\hat{z}$ direction and thus aligning magnetization inside the impurity along the z axis, and elsewhere, the anisotropy is along $\hat{x}$, modeling an in-plane magnet.

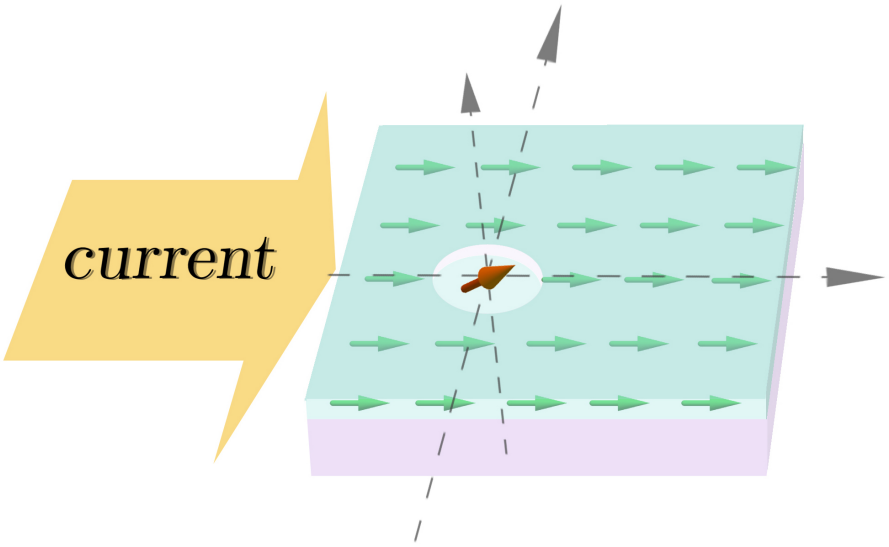

Figure 4.6: Geometrical setup for production of in-plane skyrmions via an inhomogeneity. The anisotropy in the thin film is along the $\hat{x}$ direction and the anisotropy in the pinning centre indicated by the small circular region is tilted out-of-plane.

4.3.1 Skyrmion anti-skyrmion shedding

The initial magnetic configuration is set to a uniform state along the easy x-axis, except at the pinning center where magnetization points along the z axis. The DC charge current is slowly ramped up, and the current induces tilting of the magnetization around the pinning center. As we increase the current, the non-uniform texture begins to expand and move away from the pinning center. Above a threshold current density j_c, the magnetic texture becomes unstable, and an in-plane skyrmion/antiskyrmion pair is shed off of the impurity. As the pair moves away from the pinning center, its evolution is influenced by the DMI. Since the system considered here optimally favors an in-pane skyrmion, antiskyrmion decays, followed by the emission of spin waves. Finally, the skyrmion is stabilized as it moves away from the impurity. A series of snapshots depicting the shedding process is shown in Fig. 4.7(a). It is to be noted here that the strength of critical current j_c is affected by the material parameters. Also, the value of the critical current for the shedding process is

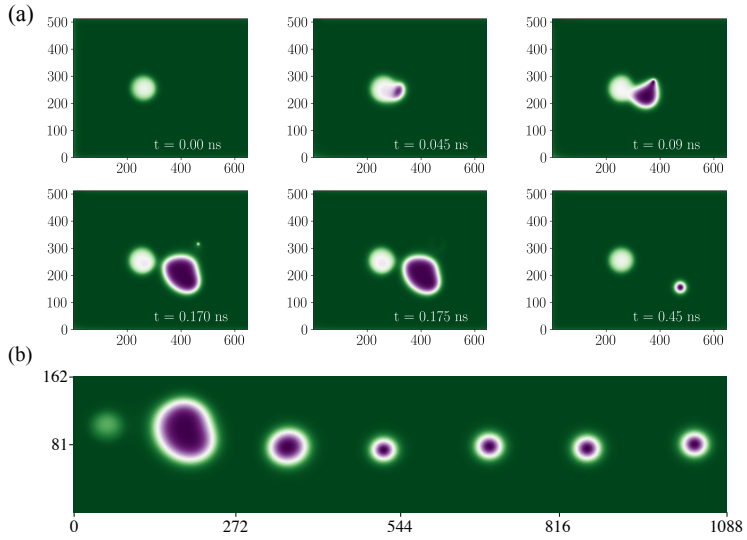

Figure 4.7: Shedding of in-plane skyrmions off of an inhomogeneity. (a) The shedding process is visualized through six sequential snapshots, indicating different stages of the process. These stages include the initial magnetic configuration, the onset of magnetic instability, its expansion across the sample, the formation of a skyrmion/antiskyrmion pair, the annihilation of the antiskyrmion, and the subsequent stabilization of the skyrmion. The full simulation size is 1024×1000 nm^2. (b) A racetrack configuration of in-plane skyrmions is produced using the shedding method. The color coding represents the m_x component of the magnetization. The simulation is performed on a sample size of 1526×1024 nm^2. [Figure and caption adapted from [82].]

less or approximately $j_c \lesssim 3.3 \cdot 10^{12}$ A/m^2 in our simulations [4]. Furthermore, in contrast to the Néel scenario studied in Everschor-Sitte *et al.*, [66], the out-of-plane anisotropy constant K_{inh} associated with the inhomogeneity domain has to be as large as K. This guarantees the shedding of in-plane skyrmions since stray fields favor large in-plane projections of the magnetization; this, in turn, yields larger values of the critical current for shedding.

4.3.2 Train of in-plane skyrmion

In the previous section, we observed that once the critical current j_c is reached, an in-plane skyrmion/antiskyrmion pair is shed from the inhomogeneity (Sec. 4.3.1).

[4] It is difficult to determine critical current density j_c since, the ramping up of the current up to critical value has to be done very slowly over longer period of time to ensure that no sudden torques due to DC currents is pumped into the system.

This leads the magnetization around the pinning center to be restored to its initial state and the shedding process is repeated. Consequently, it is possible to produce a train of in-plane skyrmions (Fig. 4.7(b)). This enables realization of the racetrack concept for in-plane skyrmions. Furthermore, the frequency of the shedding process depends on the applied current (above critical value). For the case of Néel skyrmions, it was shown in Everschor-Sitte *et al.*, [66] that the time period of the production of skyrmions near the critical current has a dependence $T \propto (j - j_c)^{-1/2}$. In contrast, in our work, we found that this dependence of frequency f on the critical current j_c is highly sensitive to the size of the impurity. The frequency dependence of in-plane skyrmion production on the critical current is shown in Fig. 4.8

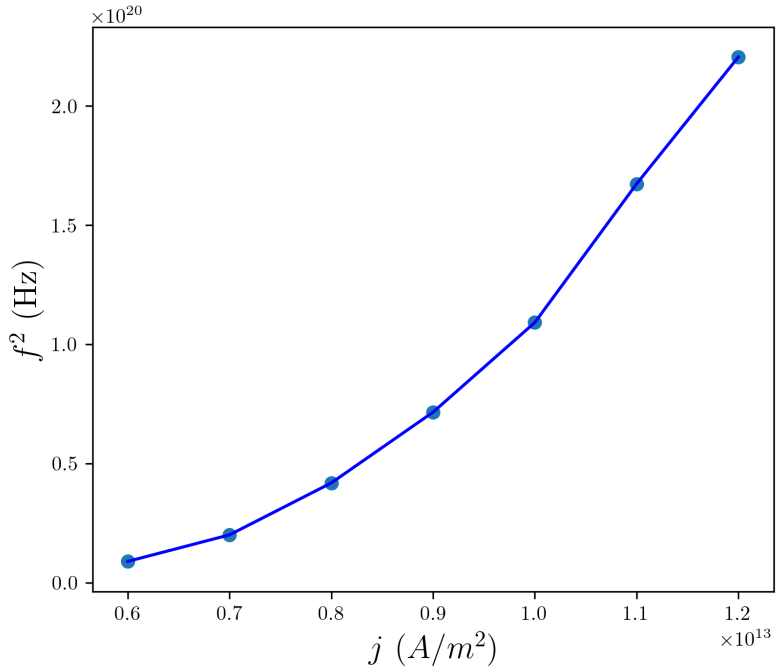

Figure 4.8: Frequency dependence of in-plane skyrmion production on the critical current j_c

4.4 Conclusion

In this chapter, we realised two different mechanisms to produce in-plane skyrmions, viz. blowing magnetic bubbles method (Sec. 4.2) and shedding

via an inhomogeneity (Sec. 4.3). Motivated by the recent experimental works on the production of Néel skyrmions using blowing magnetic bubbles method, we showed a similar implementation to produce in-plane skyrmions in thin-film in-plane magnets using micromagnetic simulations. The second method described the production of in-plane skyrmions via an inhomogeneity using the interplay between homogeneous DC currents and magnetic impurities. Finally, a proof of concept of a racetrack of in-plane skyrmions was shown (Sec. 4.3.2).


STANDS
EXIT
READ
WRITE
Skynéel
Bimero

Chapter 5

Current driven dynamics of in-plane skyrmions

In this chapter, skyrmion dynamics triggered by spin-orbit torques (SOT) and spin-transfer torques (STT) are investigated both analytically and numerically through micromagnetic simulations. Using Thiele analysis, we derive analytical formulas for the skyrmion Hall angle and the speed of skyrmions. We show that, under the influence of SOTs in-plane skyrmions move along the same spatial direction regardless of the in-plane orientation of the charge current in the thin film. This is in contrast to the behaviour of Néel skyrmions which change their direction of motion as the direction of charge current varies. Additionally, we demonstrate that the speed of the in-plane skyrmions along the racetrack depends linearly on the component of the current along the anisotropy axis. This gives us the possibility to tune the speed of in-plane skyrmions by changing the in-plane orientation of the current. These findings point towards the possibility of designing racetracks for in-plane skyrmions. Furthermore, we investigate the effect of dipolar interactions on the SOT-driven dynamics of skyrmions. Finally, we show that the dynamics of in-plane and Néel skyrmions are similar when driven by STTs.[1]

[1]The findings from this chapter are published in [82]

5.1 Introduction

On the road towards memory-based applications using skyrmions, a lot of theoretical and experimental works have been done recently on the current-driven dynamics of skyrmions. One in particular that has attracted a larger interest is skyrmion racetrack memory because of its potential application to future magnetic-storage devices [70, 74, 75]. Hence it is important to understand the mechanism of how skyrmions interact with currents. In this chapter, we are going to explore two different mechanisms to drive the skyrmions along a race track using spin torques induced by electric currents. (i) spin–orbit torques and (ii) spin-transfer torques. After the discovery of magnetic skyrmions in 2009 [40], the first observation that they can be driven by the electric current was shown in metallic B20 compounds, for example [61, 156, 187]. Since then, more works have investigated the STT induced dynamics of skyrmions [71, 157, 188, 189]. A large number of experimental and theoretical investigations on the SOT driven dynamics of Néel skyrmions have been done in recent years [44, 45, 65, 73, 76, 77, 190]. Using spin-orbit torques it was demonstrated in Pt/CoFeB/MgO multilayer that, individual skyrmions can be driven by short current pulses along a racetrack with velocities > 100 ms^{-1} [45]. A room-temperature skyrmion shift memory device was experimentally demonstrated using Ta/CoFeB/TaO$_x$ multilayer films[76]. Here they were able to generate individual skyrmions in a controllable fashion and also displace them using SOTs. Recently, real-time dynamics measurements have been done to observe the transverse motion of Néel skyrmions due to its topological charge, thus verifying the skyrmion Hall effect[73, 77].

Although a lot of investigations on the SOT driven dynamics of Néel skyrmions have been conducted over recent years, so far, the dynamics of in-plane skyrmions are yet to be explored in detail. In this chapter, we will investigate in detail the SOT and STT induced motion of skyrmions in in-plane chiral magnets and explore its benefits over that of Néel skyrmions. We will derive the Thiele equation for current-induced motion of skyrmions (both Néel and in-plane) and deduce analytical expressions for the skyrmion Hall angle and the velocities. Finally, these analytical results will be compared with micromagnetic simulations.

5.2 Spin-orbit torque dynamics

As already introduced in Sec.2.2.2, let us quickly recap the geometrical setup for SOT. We consider a bilayer consisting of a chiral magnet on top of heavy-metal layer, as depicted in Fig. 5.1(a). When the current flow in the heavy-metal (HM) layer is along $+\hat{x}$ direction (yellow arrow in the figure), due to Spin-Hall effect, a spin current with its polarisation $\boldsymbol{\sigma}$ (green arrow in the figure) along the $+\hat{y}$ direction would flow along the $+\hat{z}$ direction. This spin current induces field-like and damping-like torques on the magnetization (orange arrow in the figure) in the ferromagnetic layer (FM). Rewriting the LLG equation (2.24), describing the SOT driven dynamics of the magnetization $\boldsymbol{m}$,

$$\begin{aligned}\partial_t \boldsymbol{m} = &-\gamma\ (\boldsymbol{m} \times \boldsymbol{H}_{\text{eff}}) + \alpha\ (\boldsymbol{m} \times \partial_t \boldsymbol{m}) \\ &+ (\tau_{\text{FL}} + \tau_{\text{DL}} \boldsymbol{m}\times)(\hat{z} \times \boldsymbol{j}) \times \boldsymbol{m}\end{aligned} \tag{5.1}$$

where we have the precession, damping, field-like, and damping-like components of the SOT terms respectively.

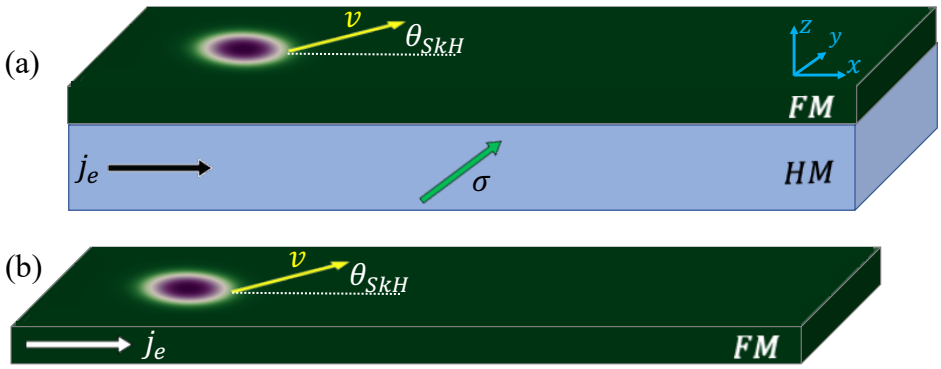

Figure 5.1: Geometries depicting current induced spin torques. (a) Spin-orbit torque: The bottom layer in blue represents the Heavy metal (HM) layer and the top layer shaded in green represents the ferromagnetic (FM) layer. The green color represents the direction of uniform magnetization along $\hat{x}$. Black and cyan arrows indicate the direction of electric current j_e, and the polarisation of the spin current σ with its polarisation in the HM. The yellow arrow represents the direction of skyrmion motion and the corresponding skyrmion hall angle θ_{SkH}. (b)Spin-transfer torque: In this case, there is only FM layer. The white arrow depicts the current in FM layer and the direction of skyrmion motion is represented by the yellow arrow.

5.2.1 Thiele analysis

The LLG equation (Eq.(5.1)) describing the SOT driven dynamics is a time-dependent nonlinear equation. A. A. Thiele found a simplification to the equation by projecting the LLG equation onto the relevant translational modes [191]. By assuming skyrmions behave as rigid spin textures (particle-like), their dynamics can be described by obtaining an equation for the motion of its center-of-mass. In this way, Thiele equation resembles Newton's equation for a particle - a dynamical force equation which is obtained from a torque equation (LLG).

To derive Thiele's equation, we begin by describing the skyrmion by its centre of mass coordinate $\boldsymbol{R} = (X, Y)$ moving with a drift velocity $\boldsymbol{v} = (v_x, v_y)$. Thus, due to its rigidity, we can write $\boldsymbol{m}(\boldsymbol{r}, t) = \boldsymbol{m}(\boldsymbol{r} - \boldsymbol{R}(t))$ and $\partial_t m_i = -v_j \ \partial m_i/\partial x_j$. Taking a cross product of $\boldsymbol{m}$ with LLG equation (Eq.(5.1)) from the left, and rewriting in the form:

$$\underbrace{-\gamma \boldsymbol{H}_{\text{eff}}}_{i} + \underbrace{\alpha \partial_t \boldsymbol{m}}_{ii} + \underbrace{\boldsymbol{m} \times \partial_t \boldsymbol{m}}_{iii} - \underbrace{\tau_{\text{FL}} \left[\boldsymbol{m} \times (\boldsymbol{\sigma} \times \boldsymbol{m})\right]}_{iv} + \underbrace{\tau_{\text{DL}} \left(\boldsymbol{m} \times \boldsymbol{\sigma}\right)}_{v} = 0 \quad (5.2)$$

where we have the (i) precession term, the (ii) damping term, (iii) kinetic term, the (iv) field-like SOT term, and the (v) damping-like SOT terms, respectively. Now, multiplying the above equation (Eq (5.2)) by $\partial m_i/\partial x_j$ followed by integrating over the volume yields the following Thiele equation [2]:

$$\boxed{\mathcal{G} \times \partial_t \boldsymbol{R} - \alpha \mathcal{D} \partial_t \boldsymbol{R} - \tau_{\text{FL}} \boldsymbol{F}_{\text{FL}} - \tau_{\text{DL}} \boldsymbol{F}_{\text{DL}} = 0} \quad (5.3)$$

where $\mathcal{G}$ is the gyrotropic tensor which produces the gyrotropic force perpendicular to the current, $\mathcal{D}$ is the dissipative tensor which describes the generalized drag force acting along the current, $\boldsymbol{F}_{\text{FL}}$ and $\boldsymbol{F}_{\text{DL}}$ are the effective forces arising from the field-like and damping-like components of SOT respectively. These forces are defined as follows

[2] For a detailed derivation of the Thiele equation please refer to Appendix-Thiele

$$\mathcal{G} = \hat{z} \int_{\mathcal{S}} d^2\boldsymbol{r} \;\; \boldsymbol{m} \cdot (\partial_i \boldsymbol{m} \times \partial_j \boldsymbol{m}) \tag{5.4}$$

$$\mathcal{D} = \frac{1}{2} \int_{\mathcal{S}} d^2\boldsymbol{r} \;\; \partial_k \boldsymbol{m} \cdot \partial_k \boldsymbol{m} \tag{5.5}$$

$$F_{\mathrm{FL},i} = \int_{\mathcal{S}} d^2\boldsymbol{r} \;\; (\hat{z} \times \boldsymbol{j}) \cdot \partial_i \boldsymbol{m} \tag{5.6}$$

$$F_{\mathrm{DL},i} = \int_{\mathcal{S}} d^2\boldsymbol{r} \;\; \boldsymbol{m} \cdot \big[(\hat{z} \times \boldsymbol{j}) \times \partial_i \boldsymbol{m}\big] \tag{5.7}$$

For a skyrmion with cylindrical symmetry, it can be shown that $\mathcal{G} = 4\pi Q\hat{z} = G\hat{z}$, where Q is the topological charge of the skyrmion (see Appendix-B. Hence, the Lorentz like force on the skyrmion due to its topological nature is responsible for the Skyrmion Hall effect (SHE) as described in Sec. 2.3.2. So for topologically trivial objects like the skyrmionium ($Q = 0$) there is no Hall-like motion [188, 192]. For a cylindrically-symmetric skyrmion, it can also be shown that the dissipative tensor $\mathcal{D}$ is diagonal, i.e. $\mathcal{D}_{xx} = \mathcal{D}_{xx} > 0$ and $\mathcal{D}_{yx} = \mathcal{D}_{xy} = 0$. This damping force arising from the Gilbert damping term is opposite and proportional to the velocity of the skyrmion.

Upon solving the coupled Thiele equations for the skyrmion velocities, we obtain

$$\partial_t X = v_x = \frac{GF_y + \alpha\mathcal{D}F_x}{G^2 + \alpha^2\mathcal{D}^2} \tag{5.8}$$

$$\partial_t Y = v_y = -\frac{GF_x - \alpha\mathcal{D}F_y}{G^2 + \alpha^2\mathcal{D}^2} \tag{5.9}$$

Let us consider the setup as shown in Fig.5.2 where the in-plane current $\boldsymbol{j}$ is injected into the thin film at an angle η w.r.t the x axis, and v is the direction of motion of the skyrmion (depicted by yellow arrow in the figure). The skyrmion Hall Angle (θ_{SkX})(Sec. 2.3.2), measured as the angle of the direction of motion of the skyrmion with respect to the current direction, is given by

$$\tan(\theta_{\mathrm{SkX}} + \eta) = \frac{\partial_t Y}{\partial_t X} = -\frac{GF_x - \alpha\mathcal{D}F_y}{\alpha\mathcal{D}F_x + GF_y} \tag{5.10}$$

where $F_x \equiv \tau_{\mathrm{FL}}F_{\mathrm{FL},x} + \tau_{\mathrm{DL}}F_{\mathrm{DL},x}$, $F_y \equiv \tau_{\mathrm{FL}}F_{\mathrm{FL},y} + \tau_{\mathrm{DL}}F_{\mathrm{DL},y}$ are the total forces

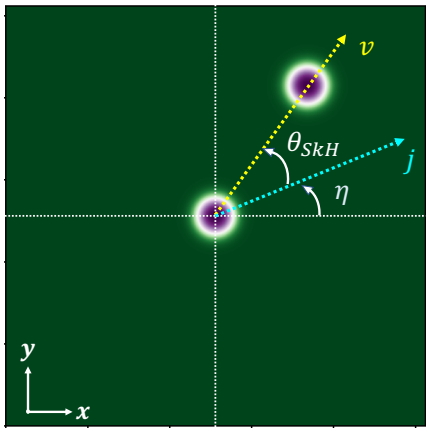

Figure 5.2: Figure depicting Skyrmion Hall effect. When the electric current $\boldsymbol{j}$ is injected at an angle η w.r.t the x-axis (cyan arrow), the skyrmion moves along the direction v (yellow arrow). The skyrmion Hall angle θ_{SkX} represents angle between the electric current ($\boldsymbol{j}$) and the skyrmion velocity (v).

along $\hat{x}$, $\hat{y}$- directions, respectively due to injected SOT current, and η is the angle between the injected current and the x axis, as depicted in Fig. 5.2. Before we look at the results from Thiele analysis for in-plane skyrmions, let us briefly look into the dynamics of Néel skyrmions.

Skyrmion Hall angle for Néel skyrmions

The expression for the Skyrmion Hall angle (θ_{SkX}) obtained in Eq. (5.10) can be simplified further by considering an ansatz to the skyrmion profile[3]. Considering a Néel skyrmion having a cylindrical symmetry, the magnetization varies only along the radial ($\boldsymbol{r}$) direction. Thus, parameterising the magnetization in the polar coordinate system (r, ϕ),

$$\boldsymbol{m}(\boldsymbol{r}) = (\sin\theta(r)\cos\phi, \sin\theta(r)\sin\phi, \cos\theta(r))^{\top} \tag{5.11}$$

$$\boldsymbol{r} = r(\cos\phi, \sin\phi) \tag{5.12}$$

with $\theta(r = 0) = \pi$ and $\theta(r = \infty) = 0$ and $^{\top}$ denoting the transpose operator. We now consider the rigid hard cutoff ansatz for Néel skyrmions, which is given

[3]The only assumption made for obtaining an expression for Skyrmion Hall angle in Eq. (5.10) was assuming the skyrmion shape is unchanged during its motion and, hence allowing us to express the dynamics in terms of its centre of mass.

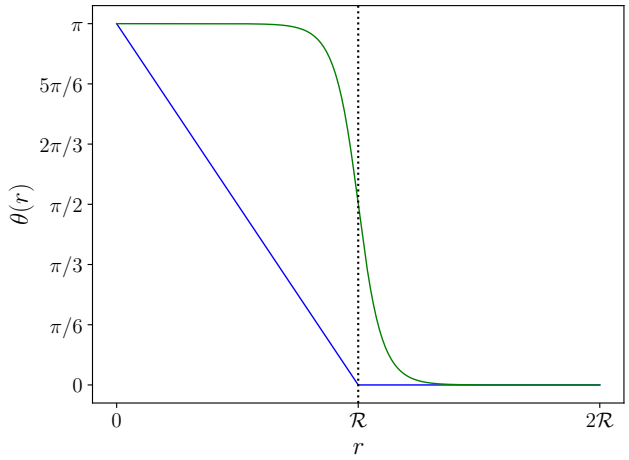

Figure 5.3: θ ansatz for skyrmion profile. Blue color represents the ansatz given by Eq.(5.13), green curve is the ansatz proposed in the work of Kravchuk *et al* [165] and the black vertical line representing the radius of the skyrmion ($\mathcal{R}$).

by

$$\theta(r) = \pi(1 - r/\mathcal{R})\Theta(\mathcal{R} - r) \tag{5.13}$$

where $\Theta(x)$ is the Heaviside theta function and $\mathcal{R}$ denotes the skyrmion radius. The theta-profile for a Néel skyrmion is shown in Fig. 5.3. By plugging the ansatz into Eqs. (B.9), (B.10), we obtain the following expression for the SOT current induced forces;

$$\begin{aligned} F_x &= \frac{\pi^2}{2} j\mathcal{R}\tau_{\mathrm{DL}} \cos\eta \\ F_y &= \frac{\pi^2}{2} j\mathcal{R}\tau_{\mathrm{DL}} \sin\eta \end{aligned} \tag{5.14}$$

From the above set of equations (Eq. (5.14)) it is clear that, the field-like component of the SOT has no influence on the skyrmion motion. The zero net force of the field-like component arises from the symmetry of field-like SOT term which can be understood using the following simple picture. The field from field-like SOT is along $\hat{z} \times \hat{j}$ (See Eq. (5.1)). For the sake of simplicity, assuming the current $\hat{j}$ is along $\hat{x}-$direction, then the resultant field is along $\hat{y}-$direction. Now for a Néel skyrmion, a field along $\hat{y}$ would result only in

tilting of the magnetization and no effect on its translational motion [193, 194]. However, this picture fails when the skyrmion shape is deformed and it looses cylindrical symmetry. In such a case, there will be non-zero force from the field-like SOT as well. This deformation can happen due to different reasons like, thermal noise, impurities/disorder, and very strong field-like components. The skyrmion Hall angle (θ_{SkX}) dependence due to skyrmion deformation was investigated in the works of Litzuis *et al* [73]. However, in our work, we will limit to rigid skyrmion texture. By plugging the Eq. (5.14) into Eq. (5.10), the skyrmion Hall angle for the spin-orbit dynamics of Néel skyrmions reads

$$\boxed{\tan\left(\theta_{\mathrm{SkX}}^{\mathrm{Néel}} + \eta\right) = \frac{\alpha\mathcal{D}\sin(\eta) - G\cos(\eta)}{\alpha\mathcal{D}\cos(\eta) + G\sin(\eta)},} \tag{5.15}$$

where the $\theta_{\mathrm{SkX}}^{\mathrm{Néel}}$ explicitly depends on the in-plane orientation of the injected current.[73, 74, 134]. This implies that, when the in-plane orientation of the injected current (η) is changed, the skyrmion now begins to move in a different direction than before. When the injected current is along the x-direction ($\eta = 0$), the skyrmion Hall angle $\theta_{\mathrm{SkX}}^{\mathrm{Néel}}$ reduces to $\arctan(-G/\alpha\mathcal{D})$, implying the skyrmion moves in the opposite direction of the applied current.

Skyrmion Hall angle for in-plane skyrmions

Similar to Néel skyrmions, the SOT driven behavior of in-plane skyrmions can be understood as well from Thiele analysis. We can obtain an expression for the skyrmion Hall angle θ_{SkX} by considering the same rigid cutoff ansatz to the skyrmion θ-profile as defined in Eq. (5.13). The magnetization of an in-plane skyrmion in the polar coordinate system can be parameterised as follows

$$\boldsymbol{m}(\boldsymbol{r}) = (-\cos\theta(r), \sin\theta(r)\cos\phi, \sin\theta(r)\sin\phi)^{\top} \tag{5.16}$$

$$\boldsymbol{r} = r(\cos\phi, \sin\phi) \tag{5.17}$$

By plugging the rigid-cutoff ansatz along with Eq. (5.17) into Eqs. (B.9), (B.10), we obtain the following expression for the SOT current induced forces

on an in-plane skyrmion

$$\begin{aligned} F_x &= \frac{\pi^2}{2} j\mathcal{R}\tau_{\mathrm{DL}} \cos\eta \\ F_y &= 0 \end{aligned} \tag{5.18}$$

The following remarks can be made from Eq. (5.18). (i) Similar to Néel

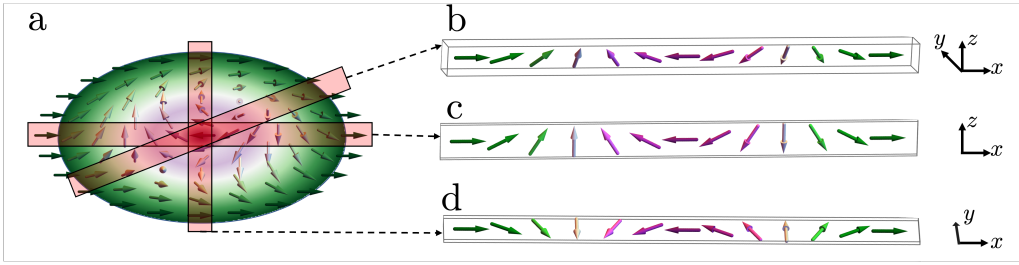

Figure 5.4: Character of domains walls in in-plane skyrmions. (a) A schematic illustration of an in-plane skyrmion is presented, showcasing three distinct cross-sections that exhibit different characteristics of the domain wall. These cross-sections, highlighted in pink, are further depicted in (b), (c), and (d) to provide their corresponding profiles. Along a cross-section parallel to $\hat{x}(\hat{(y)})$, the magnetization rotates in the $\hat{x}-\hat{z}$ $(\hat{x}-\hat{y})$ plane. In both of these profiles, a Néel wall character is observed. However along an arbitrary direction $\boldsymbol{r}$ within the $\hat{x}-\hat{y}$ plane, the domain wall profile exhibits a Bloch nature. This distinction leads to intriguing consequences in the current-driven motion using SOT.

skyrmions, the field-like component of SOT has no influence on the skyrmion motion due to the symmetry of the SOT. (ii) In contrast to Néel skyrmions, the cylindrical symmetry is lost for in-plane skyrmions in the presence of dipolar-dipolar interactions. Hence there will be non-zero force from field-like components of SOT for in-plane skyrmions. This effect was investigated in detail using micromagnetic simulations which will be discussed in the next section (Sec. 5.2.2). (iii) The symmetries of the in-plane skyrmion and SOT give rise to interesting influence of SOT on in-plane skyrmions. First, only the $\hat{x}$-component of the injected current (j_x) influences the SOT driven dynamics. (iv) Second, the significant difference from that of Néel skyrmions is that the damping-like field of SOT has a force component only along the x-direction. These two peculiarities (iii, iv) can be intuitively explained intuitively as illus-

trated in Fig. 5.4. A cross-section of an in-plane skyrmion along $\hat{x}$ is an Néel DW in the $\hat{x}-\hat{z}$ plane (Fig. 5.4(a) left). Similarly, a cross-sections along $\hat{y}$ is a in-plane Néel DW in the $\hat{x}-\hat{y}$ plane (Fig. 5.4(a) center). But along any other radial direction, we have a Bloch type features in the DW (Fig. 5.4(a) right). We know that the SOT does not move Bloch DW's as explained before (Sec. 2.2.2). Now, when the injected current is purely along $\hat{y}$-direction, i.e., $\eta = 0$, neither the $\hat{x}-\hat{z}$ DW nor the $\hat{x}-\hat{y}$ is influenced by the SOT, and hence it does not move as shown in Fig. 5.4(b). Hence, a non-zero x-component of the injected current is required to move the in-plane skyrmions. Since a Bloch DW can't be moved using SOT, the Bloch nature of the in-plane skyrmion remains uninfluenced. In addition, there is a fixed contribution to the Lorentz-like force which determines the direction of motion for in-plane skyrmions. This is evident by the fact that in-plane skyrmions exhibit an unidirectional SOT-driven motion regardless of the in-plane orientation of the injected current, which is also characterized by the following skyrmion Hall angle

$$\theta_{\mathrm{SkX}}^{\text{in-pl}} = -\left[\tan^{-1}\left(G/\alpha\mathcal{D}\right) + \eta\right] \tag{5.19}$$

From the above expression for Hall angle (Eq. ((5.19))) it is evident that, in contrast to Néel skyrmions, the skyrmion Hall angle for in-plane skyrmions $\theta_{\mathrm{SkX}}^{\text{in-pl}}$ varies linearly with the in-plane orientation of the injected current η, as shown in Fig.5.5(a) (▲ data points in the figure). In other words, $\theta_{\mathrm{SkX}}^{\text{in-pl}} + \eta$ is a constant, meaning that the in-plane skyrmions always move along the same spatial direction regardless of the in-plane orientation (η) of the charge current. Furthermore, the speed of in-plane skyrmions along the racetrack can be determined by plugging Eq. (5.17) and (5.13) into Eq. (5.9)

$$v = |\partial_t \boldsymbol{R}| = \frac{F_x}{\sqrt{(G^2 + \alpha^2\mathcal{D}^2)}} = \frac{\pi^2 j \mathcal{R} \tau_{\mathrm{DL}}}{2\sqrt{(G^2 + \alpha^2\mathcal{D}^2)}} \cos\eta \tag{5.20}$$

which depends only on the x-component of the applied current $\boldsymbol{j}$. The speed of the in-plane skyrmion will be maximum for currents parallel to the easy x-axis, and zero for currents transverse to it as shown in Fig. 5.5(b)(▲ data points in the figure). These findings point towards the possibility of designing

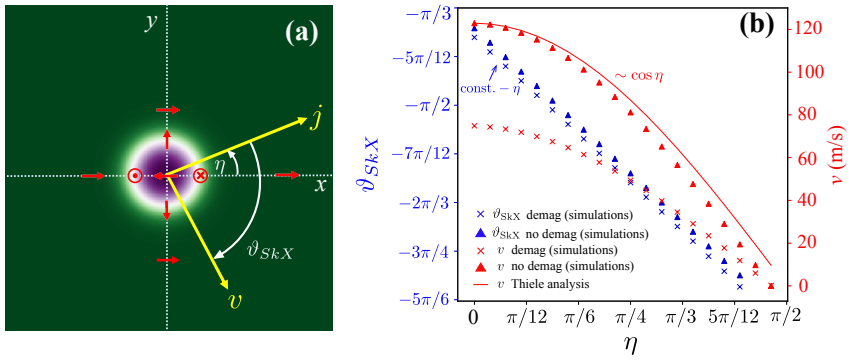

Figure 5.5: Skyrmion Hall effect for the in-plane configuration. (a) Geometry considered to define the skyrmion Hall angle θ_{SkX}. The electric current ($\boldsymbol{j}$) and the velocity (v) of the skyrmion are represented by yellow arrows, where η denotes the angle between the former and the x axis. The direction of magnetization at different points is indicated by red arrows. (b) Dependence of the skyrmion Hall angle (blue) and terminal speeds (red) on the direction of the applied charge current (defined by η). The skyrmion velocity has been calculated in the presence (crosses) or absence (triangles) of stray fields, and within the Thiele collective-coordinate approach disregarding stray fields as well (red line). [Figure and caption adapted from [82]]

racetracks for in-plane skyrmions along the direction $\tan^{-1}(G/\alpha\mathcal{D})$, and their speed could be tuned by adjusting the in-plane orientation of the injected current.

5.2.2 Micromagnetic simulations

We perform micromagnetic simulations to study the SOT driven dynamics of skyrmions and corroborate with analytical results obtained from Thiele analysis discussed in the previous section 5.2.1. All the simulations for the SOT dynamics are performed using the micromagnetic software package mumax^3 [112].

We simulate a thin film chiral in-plane magnet of dimensions $256 \times 256 \times 1$ nm^3. Initially, we compute an equilibrium magnetization configuration of the in-plane skyrmion by solving the LLG equation (with only damping term), until the energy is converged to a local minimum[4]. We choose the finite-difference mesh discretisation $1 \times 1 \times 1\times$ nm^3. The material parameters we

[4]For details on the micromagnetic framework please refer to Sec. (2.1.3)

use for these simulations in the absence of stray fields are[5]: Saturation magnetization $M_s = 580$ kA m^{-1}, Exchange energy constant $A = 15$ pJ m^{-1}, Uniaxial anisotropy constant $K = 500$ kJ m^3, and Dzyaloshinskii-Moriya energy constant $D = 3.0$ mJ m^{-2}.

Once the relaxed equilibrium configuration is reached, we drive the in-plane skyrmions using SOT. The SOT is generated by injecting an in-plane charge current $j = 1 \times 10^{12}$Am^2 in the thin film at an angle η w.r.t anisotropy axis. The strength of the damping-like SOT τ_{DL} has been derived from the formula [77] $\tau_{DL} = \gamma\hbar\theta_{SH}/2eM_s t$, with thickness of the film $t = 1$ nm and spin Hall angle $\theta_{SH} = 0.15$. The dynamics is simulated for 1 ns, and the magnetization data is recorded at uniform time steps of $\Delta t = 1$ ps. After that, we analyse the recorded magnetization data $\boldsymbol{m}(\boldsymbol{r}, t)$ to find the skyrmion trajectory, thereby evaluating the skyrmion Hall angle θ_{SkX} and the skyrmion velocity v. The tracking of skyrmion position during its motion is done in two steps: (i) Evaluating the domain wall contour i.e., $m_x = 0$ ($m_z = 0$) contour for in-plane (Néel) skyrmion at each time step, thereby (ii) calculating the centre of the contour (which is also the centre of the skyrmion $\boldsymbol{R}(X, Y)$). Finally, we calculate the skyrmion Hall angle by $\theta_{\mathrm{SkX}} = \arctan(\partial_t Y/\partial_t X) - \eta)$ and the velocity by $v = |\partial\boldsymbol{R}/\partial t|$. We perform these simulations for different values of the in-plane orientation of the charge current η which is varied from 0 to π and the skyrmion Hall angle is calculated in each case.

Micromagnetic simulations indicate that the in-plane skyrmions can be efficiently manipulated by SOT. The results of the micromagnetic simulations are displayed in Fig. 5.5. From the simulations, we again observe that the skyrmion Hall angle $\theta_{\mathrm{SkX}}^{\text{in-pl}}$ varies linearly with the orientation of the current η, meaning that the in-plane skyrmions always move along the same spatial direction regardless of the in-plane orientation (η) of the charge current as shown in the Fig. 5.5(a) (– line in the figure). This agrees with the Eq. (5.19) from Thiele analysis. Additionally, the speed of in-plane skyrmions measured from simulations varies linearly with the x-component of the current (– line in the Fig. 5.5(b)), which is in agreement with the analytical expression for v

[5]These parameters are typical values of a permalloy material. [134]

(Eq. 5.20). Thus, the results from micromagnetic simulations corroborate our analytical findings from Thiele analysis.

5.2.3 Effect of dipolar interactions

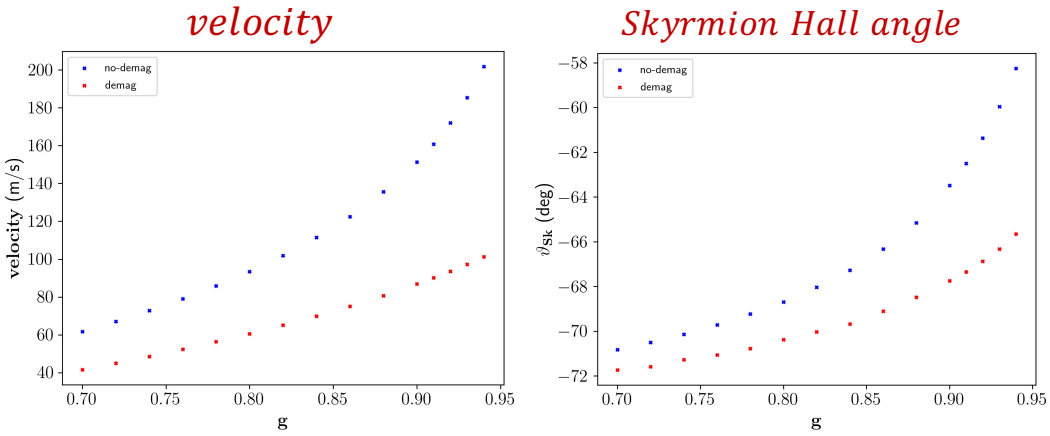

Figure 5.6: Effect of dipolar interactions on the skyrmion motion under SOT

As discussed in Sec. 3.4, the presence of dipolar interactions leads to a reduction of the size of in-plane skyrmions. Furthermore, it also breaks the cylindrical symmetry of in-plane skyrmions (see Fig. 3.7). This results in dissipative tensor $\mathcal{D}$ no more being diagonal, i.e., $\mathcal{D}_{xy}, \mathcal{D}_{yx} > 0$. The micromagnetic simulations show that the presence of dipolar interactions leads to a reduction of the speed for in-plane skyrmions, as illustrated from the ○ curves in Fig. 5.6.

5.3 Spin-transfer torque dynamics

As shown in the previous chapter. 4, spin-transfer torques can be used in the production of skyrmions and also in moving the skyrmions. In this section, we shall investigate in detail the skyrmion motion using spin-transfer torques. When a spin-polarised electric current is passed through a thin film of a chiral magnet, spin angular momentum between the spin of the conduction electron and the magnetization. Rewriting the LLG equation (Eq.(2.2.1)) describing

the STT driven dynamics of the magnetization $\boldsymbol{m}$,

$$\begin{aligned}\partial_t \boldsymbol{m} = &-\gamma\ (\boldsymbol{m} \times \boldsymbol{H}_{\text{eff}}) + \alpha\ (\boldsymbol{m} \times \partial_t \boldsymbol{m}) \\ &+ \zeta \boldsymbol{m} \times (\vec{j} \cdot \vec{\nabla})\boldsymbol{m} - \zeta\beta\, \boldsymbol{m} \times \Big(\boldsymbol{m} \times (\vec{j} \cdot \vec{\nabla})\boldsymbol{m}\Big)\end{aligned} \tag{5.21}$$

where the first terms correspond to the precession and damping terms respectively. The interaction between spin-polarized currents and the magnetic texture is modeled by the adiabatic (3^{rd} term) and non-adiabatic spin-transfer-torques (4^{th} term) [128]. Here, $\zeta = \gamma P\hbar/2eM_s$ is the charge-to-spin conversion factor in the adiabatic regime, P represents the electron spin polarization, β parameterizes the strength of the non-adiabatic torque.

By looking at the terms of the equation (5.21), we can make paint a simple physical picture of the behavior of the local magnetization under the influence of spin-polarized current. For the sake of simplicity let us consider that the current density $\boldsymbol{j}$ is a spatially uniform field along $\hat{x}$-direction and $\boldsymbol{j}$ is positive. Then the term $(\boldsymbol{j} \cdot \vec{\nabla})\boldsymbol{m}$ reduces to $j_x \partial_x \boldsymbol{m}$. Now the effect of adiabatic torque simplifies to adding velocity to $\boldsymbol{m}$ pushing it in the direction of $\boldsymbol{m} + \hat{x}$. Hence the magnetic texture (a skyrmion in this case) moves along the direction of the applied current. We know that a skyrmion exhibits Skyrmion Hall effect moving also along a transverse direction to that of applied current (see Sec.2.3.2). This can be accounted for by the non-adiabatic torque. Following the same analogy as before, for the case of non-adiabatic torque, the local field is now pointed along $j_x \partial_x \boldsymbol{m}$ direction and the resulting torque exerts a velocity perpendicular to the direction of spin current $\boldsymbol{j}$. It should be noted here that the Gilbert damping term also contributes a velocity along a direction $(\boldsymbol{m} \times \partial_t \boldsymbol{m})$ which is opposite to that of non-adiabatic torque [6]. The competition of these torques moves the skyrmion both along the direction of the applied current and transverse to it.

[6] If $\alpha = \beta$ then the transverse forces are balanced and the skyrmion moves only along the direction of applied current.

5.3.1 Thiele analysis

Following the method described in Sec.5.2.1, assuming that the skyrmions behave as rigid spin textures, the Thiele equation that captures the motion of skyrmions under the influence of STT:

$$\boxed{\mathcal{G}\partial_t \boldsymbol{R} - \alpha\mathcal{D}\partial_t \boldsymbol{R} + b_j F_1 \ \boldsymbol{j} + \beta b_j F_2 \ \boldsymbol{j} = 0} \tag{5.22}$$

where $\mathcal{G}$ is the gyrotropic tensor, $\mathcal{D}$ is the dissipative tensor, F_1 and F_2 are the effective forces arising from the adiabatic and non-adiabatic components of STT respectively. These forces are defined as follows:

$$\mathcal{G} = \int_{\mathcal{S}} d^2\boldsymbol{r} \ \ \boldsymbol{m} \cdot (\partial_i \boldsymbol{m} \times \partial_j \boldsymbol{m}) \tag{5.23}$$

$$\mathcal{D} = \int_{\mathcal{S}} d^2\boldsymbol{r} \ \partial_k \boldsymbol{m} \cdot \partial_k \boldsymbol{m} \tag{5.24}$$

$$F_1 = \int_{\mathcal{S}} d^2\boldsymbol{r} \ \ \boldsymbol{m} \cdot (\partial_i \boldsymbol{m} \times \partial_j \boldsymbol{m}) \tag{5.25}$$

$$F_2 = \int_{\mathcal{S}} d^2\boldsymbol{r} \ \partial_k \boldsymbol{m} \cdot \partial_k \boldsymbol{m} \tag{5.26}$$

When the non-adiabatic component of STT has the same strength as the Gilbert damping ($\beta = \alpha$), there is a cancellation of the Magnus force and the skyrmions move parallel to the direction of the spin polarised current.

Micromagnetic simulations

We perform micromagnetic simulations to study the STT driven dynamics of skyrmions using the micromagnetic software package mumax^3 [112]. We simulate a thin film chiral in-plane magnet of dimensions $256 \times 256 \times 1$ nm^3. We choose the finite-difference mesh discretisation $1 \times 1 \times 1\times$ nm^3. We use the same material parameters as that of SOT dynamics of skyrmions. We verify that both Néel and in-plane skyrmions can be moved using STT's and they exhibit skyrmion Hall effect. Since STT couples to the spatial gradient of the magnetization, the behaviour of Néel and in-plane skyrmions are similar

5.4 Conclusion

In this chapter, we explored the current-driven dynamics of skyrmions induced by spin-orbit torques and spin-transfer torques. Using Thiele analysis we derived an analytical expression for the skyrmion Hall angle and the skyrmion velocity. We found that the in-plane skyrmions and Néel skyrmions exhibit similar dynamics driven by spin transfer torques. The Thiele analysis results for in-plane skyrmions indicate that, under the influence of SOT the skyrmion Hall angle varies linearly with the in-plane orientation of the injected charge current indicating an uni-directional motion of the in-plane skyrmions in the chiral magnet. We also found that the velocity of the in-plane skyrmions is linear with x-component of the current which allows for control of the speed of in-plane skyrmions by changing the direction of charge current in the plane. These results indicate an advantage of in-plane skyrmions over Néel skyrmions for race-rack applications. Furthermore, we examine the effects of dipolar interactions on the drive of in-plane skyrmions. We also examine the dynamics using micromagnetic simulations which corroborate our analytical findings from Thiele analysis. Having studied the current driven dynamics, in the next chapter, we will address another important aspect of skyrmions, viz., the excitations of in-plane skyrmions.

Summary

At the time we started this research, a few experiments reported the observation of in-plane skyrmions in MnSi thin films [78, 79]. They were theoretically predicted to exist in thin films with in-plane anisotropy and stabilized by frustrated interactions [162]. Many questions were yet to be answered regarding their shape, the corresponding stabilizing mechanisms emerging in in-plane ferromagnets, the means of producing them, and their current-driven dynamics, to name a few. In the course of the thesis, we studied the topological properties of in-plane skyrmions and explored their potential to design racetrack memory devices.

In **Chapter 3**, we introduced a generic micromagnetic model to describe in-plane skyrmions. Equivalence between in-plane and out-of-plane models through a rotational transformation was discussed, and a comparative study with Néel skyrmions was done. Through micromagnetic simulations, we analyzed the similarities and differences between in-plane and Néel skyrmions in the presence and absence of stray fields. This analysis revealed that stray fields reduce the size of in-plane skyrmions in contrast to Néel skyrmions, where the size of the skyrmions increases in their presence. Furthermore, stray fields break the cylindrical symmetry of in-plane skyrmions. To explain this striking behavior of in-plane skyrmions in the presence of stray fields, a bi-axial anisotropy model was introduced. This model has been contrasted against standard micromagnetic simulations carried out in MuMax3, in which the complete stray fields are calculated. The properties of skyrmions as a

function of the ratio of the two anisotropies were analyzed, which allowed us to calculate the value of the stray field pointing out-of-plane. To understand better the nature of in-plane DMI that stabilizes the in-plane skyrmions, we performed symmetry analysis, looked at the compatible crystallographic space groups, and proposed material candidates for their observations. Symmetry analysis revealed that only the monoclinic point group m allows for in-plane DMI since the DMI tensor compatible with its symmetries in the thin-film limit contains contributions from both in-plane and Néel DMIs. Within the scope of this thesis, we focused on in-plane magnets within the monoclinic system Cm. In particular, we studied the stability of in-plane skyrmions across the phase diagram parameterized by the two DMI constants. The presence of both in-plane and Néel DMI breaks the cylindrical symmetry, leading to elliptical deformations of the skyrmion shape. However, the presence of Néel DMI enables the stabilization of in-plane skyrmions even at very low strengths of in-plane DMI, since it favors the stabilization of out-of-plane domain walls.

In **Chapter 4** two different mechanisms for the production of in-plane skyrmions in thin films were discussed. The first one is based on blowing magnetic bubbles through a geometric constriction. This mechanism involves the conversion of a domain-wall pair into an in-plane skyrmion at its end: the non-uniform current distribution exerts an inhomogeneous spin-transfer torque on the stripe domains as they exit the geometric constriction, resulting in their radial expansion. These radial-shaped domain-wall pairs form skyrmion bubbles when detaching from the constriction. This mechanism drew an intriguing analogy with the formation of soap bubbles when a soap film pinched off upon blowing air through a straw or a bubble wand. The second method sheds in-plane skyrmions from a magnetic inhomogeneity via the application of homogeneous DC current: when the magnetization of the impurity pinning center is perpendicular to the uniform magnetic background, the DC charge current induces tilting of the magnetization around the pinning center. With the increase of the current density, the non-uniform texture expands and, above a certain threshold current density j_c, this magnetic texture becomes unstable and an in-plane skyrmion/antiskyrmion pair is shed off of the impurity. Finally, the skyrmion is stabilized whereas the antiskyrmion collapses as it moves

away from the impurity. Analysis of the strength of critical current j_c and of the shedding frequency showed a non-linear dependence on the critical current affected by the size of the impurity. We also proposed the design of a racetrack for in-plane skyrmions based on this latter mechanism and showed its feasibility via micromagnetic simulations.

In **Chapter 5** we explored the current-driven dynamics of skyrmions induced by spin-orbit and spin-transfer torques. By considering a collective variable approach, we derived an analytical expression for the skyrmion Hall angle and the velocity of the skyrmions. We found that in-plane and Néel skyrmions exhibit similar dynamics driven by spin-transfer torques. However, under the influence of spin-orbit torques, Thiele analysis for in-plane skyrmions indicates that the skyrmion Hall angle varies linearly with the in-plane orientation of the injected charge current, suggesting the uni-directional motion of the in-plane skyrmions in the chiral magnet. We also found that the velocity of the in-plane skyrmions is linear with x-component of the current, which allows for control of the speed of in-plane skyrmions by changing the direction of charge current within the plane. These results make in-plane skyrmions more advantageous than Néel skyrmions for racetrack applications. Furthermore, we examined the effects of stray fields on the current-driven motion of in-plane skyrmions. In addition, we also checked these current-driven dynamics by means of micromagnetic simulations, which corroborated our analytical findings.

To conclude, thin film ferromagnetic platforms with in-plane anisotropy and in-plane DMI can stabilize chiral textures compatible with domain walls whose magnetization changes within the plane of the film. In this thesis, we have extensively studied the properties and stability of in-plane skyrmions in in-plane magnets. Furthermore, we demonstrated the production of in-plane skyrmions mediated by spin currents. Finally, we discussed the current-driven dynamics of in-plane skyrmions and their potential application for spin-based memory devices.

Appendix A

Axial asymmetry in Cm skyrmions

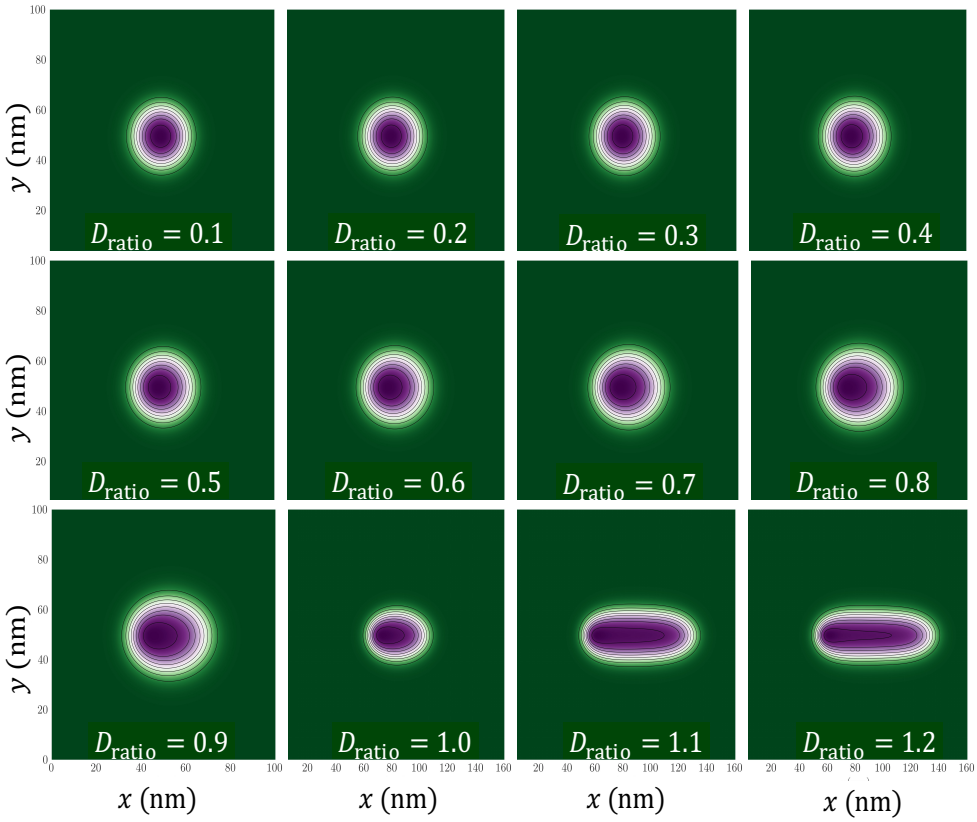

Figure A.1: Magnetization density plots for different values of D_{ratio} for a fixed value of $D_{\text{in-pl}}$. The in-plane skyrmions shown here were stabilized within the Cm model (see Sec.3.7). It can be seen from the contours that the cylindrical symmetry is broken for any nonzero value of $D_{\text{Néel}}$.

Appendix B

Thiele equation of motion

This appendix provides detailed steps involvled in calculating the various forces of the Thiele equation. To begin, we will apply the Thiele procedure to the LLG equation, resulting in the derivation of the general Thiele equation. Subsequently, we will derive the specific expressions for each force involved.

Thiele Equation of motion for SOT dynamics

Rewriting the LLG equation (2.24), describing the SOT driven dynamics of the magnetization $\boldsymbol{m}$,

$$\begin{aligned}\partial_t \boldsymbol{m} = &-\gamma\ (\boldsymbol{m} \times \boldsymbol{H}_{\text{eff}}) + \alpha\ (\boldsymbol{m} \times \partial_t \boldsymbol{m}) \\ &+ (\tau_{\text{FL}} + \tau_{\text{DL}} \boldsymbol{m}\times)(\hat{z} \times \boldsymbol{j}) \times \boldsymbol{m}\end{aligned} \tag{B.1}$$

where the first two terms represent the precession and damping terms, and the third and fourth terms represent the fieldlike and damping-like SOTs respectively. Here, the spin polarisation $\boldsymbol{\sigma} = (\hat{z} \times \boldsymbol{j})$ is along the $+\hat{y}$ direction. τ_{FL} and τ_{DL} parametrize the field-like and damping-like strengths of the SOT, respectively.

Thiele's key insight was that when a magnetization pattern undergoes a rigid motion without any deformations, the entire state of the magnetization can be effectively captured by the position of a single characteristic feature

within the pattern. To derive Thiele's equation for skyrmions, we begin by describing the skyrmion by its centre of mass coordinate $\boldsymbol{R} = (X, Y)$ moving with a drift velocity $\boldsymbol{v} = (v_x, v_y)$. Thus, due to its rigidity, we can write $\boldsymbol{m}(\boldsymbol{r}, t) = \boldsymbol{m}(\boldsymbol{r} - \boldsymbol{R}(t))$. The time derivative can be transformed into a spatial derivative as

$$\frac{\partial \boldsymbol{m}}{\partial t} = -\sum_i \dot{r}_i \frac{\partial \boldsymbol{m}}{\partial r_i} \;=\; -(\boldsymbol{v}\cdot\boldsymbol{\nabla})\,\boldsymbol{m} \tag{B.2}$$

To be concise, the spatial dependence of $\boldsymbol{m}$ will be omitted. Inserting the spatial derivative form back into LLG yields,

$$\begin{aligned} -(\boldsymbol{v}\cdot\boldsymbol{\nabla})\,\boldsymbol{m} = &-\gamma\,(\boldsymbol{m}\times\boldsymbol{H}_{\text{eff}}) \\ &-\alpha\,(\boldsymbol{m}\times(\boldsymbol{v}\cdot\boldsymbol{\nabla})\,\boldsymbol{m}) \\ &+(\tau_{\text{FL}}+\tau_{\text{DL}}\boldsymbol{m}\times)(\hat{z}\times\boldsymbol{j})\times\boldsymbol{m} \end{aligned} \tag{B.3}$$

Now the projection of the LLG equation onto the relevant translation modes is achieved in two steps. First, we take a cross product of $\boldsymbol{m}$ with LLG equation (Eq. (B.1)),

$$\begin{aligned} 0 = \boldsymbol{m}\times[(\boldsymbol{v}\cdot\boldsymbol{\nabla})\,\boldsymbol{m}] &-\gamma\;\boldsymbol{m}\times(\boldsymbol{m}\times\boldsymbol{H}_{\text{eff}}) \\ &-\alpha\;\boldsymbol{m}\times[(\boldsymbol{m}\times(\boldsymbol{v}\cdot\boldsymbol{\nabla})\,\boldsymbol{m})] \\ &+\tau_{\text{FL}}\;[\boldsymbol{m}\times(\boldsymbol{\sigma}\times\boldsymbol{m})] +\;\tau_{\text{DL}}\;(\boldsymbol{m}\times\boldsymbol{\sigma}) \end{aligned} \tag{B.4}$$

The next stop involves multiplying the above equation (Eq. B.4) by $\partial m_i/\partial x_j$ followed by integrating over the volume.

$$\begin{aligned} \int_{\mathcal{S}} d^2\boldsymbol{r}\;\;\gamma\,\frac{\partial m_i}{\partial x_j}\,\boldsymbol{H}_{\text{eff},i} = &-\int_{\mathcal{S}} d^2\boldsymbol{r}\;\;\boldsymbol{m}\cdot\left(\frac{\partial \boldsymbol{m}}{\partial x_j}\times\frac{\partial \boldsymbol{m}}{\partial x_i}\right)\dot{r}_i \\ &+\int_{\mathcal{S}} d^2\boldsymbol{r}\;\;\alpha\;\left(\frac{\partial \boldsymbol{m}}{\partial x_i}\cdot\frac{\partial \boldsymbol{m}}{\partial x_j}\right)\dot{r}_i \\ &+\int_{\mathcal{S}} d^2\boldsymbol{r}\;\;\tau_{\text{FL}}\,\frac{\partial m_i}{\partial x_j}\sigma_i \\ &+\int_{\mathcal{S}} d^2\boldsymbol{r}\;\;\tau_{\text{DL}}\left(\frac{\partial \boldsymbol{m}}{\partial x_j}\times\boldsymbol{m}\right)\sigma_i \end{aligned} \tag{B.5}$$

Rewriting the above equation in tensor form yields, the following expression

for Thiele equation:

$$\mathcal{G} \times \partial_t \boldsymbol{R} - \alpha \mathcal{D} \partial_t \boldsymbol{R} - \tau_{\mathrm{FL}} \boldsymbol{F}_{\mathrm{FL}} - \tau_{\mathrm{DL}} \boldsymbol{F}_{\mathrm{DL}} = 0 \tag{B.6}$$

where $\mathcal{G}$ is the gyrotropic tensor which produces the gyrotropic force perpendicular to the current, $\mathcal{D}$ is the dissipative tensor which describes the generalized drag force acting along the current, $\boldsymbol{F}_{\mathrm{FL}}$ and $\boldsymbol{F}_{\mathrm{DL}}$ are the effective forces arising from the field-like and damping-like components of SOT respectively. These forces are defined as follows

$$\mathcal{G} = \hat{z} \int_{\mathcal{S}} d^2\boldsymbol{r} \;\; \boldsymbol{m} \cdot (\partial_i \boldsymbol{m} \times \partial_j \boldsymbol{m}) \tag{B.7}$$

$$\mathcal{D} = \int_{\mathcal{S}} d^2\boldsymbol{r} \;\; \partial_i \boldsymbol{m} \cdot \partial_i \boldsymbol{m} \tag{B.8}$$

$$F_{\mathrm{FL},i} = \int_{\mathcal{S}} d^2\boldsymbol{r} \;\; (\hat{z} \times \boldsymbol{j}) \cdot \partial_i \boldsymbol{m} \tag{B.9}$$

$$F_{\mathrm{DL},i} = \int_{\mathcal{S}} d^2\boldsymbol{r} \;\; \boldsymbol{m} \cdot \big[(\hat{z} \times \boldsymbol{j}) \times \partial_i \boldsymbol{m}\big] \tag{B.10}$$

Appendix C

DMI tensor for the crystallographic point groups

In this appendix, the DMI tensors are presented for different space group symmetries, indicating which elements are zero and which elements are equivalent.

$C_i, C_{2h}, D_{2h}, C_{4h}, D_{4h}, C_{3i}, D_{3d}, C_{3h}, C_{6h}, D_{3h}, D_{6h}, T_h, T_d, O_h$ $\begin{pmatrix} 0 & 0 & 0 \\ 0 & 0 & 0 \\ 0 & 0 & 0 \\ 0 & 0 & 0 \\ 0 & 0 & 0 \\ 0 & 0 & 0 \\ 0 & 0 & 0 \\ 0 & 0 & 0 \\ 0 & 0 & 0 \end{pmatrix}$	C_1 $\begin{pmatrix} 0 & 0 & 0 \\ D_{xxy} & D_{xyy} & D_{xzy} \\ D_{xxz} & D_{xyz} & D_{xzz} \\ -D_{xyy} & -D_{xyy} & -D_{xzy} \\ 0 & 0 & 0 \\ D_{yxz} & D_{yyz} & D_{yzz} \\ -D_{xxz} & -D_{xyz} & -D_{xzz} \\ -D_{yxz} & -D_{yyz} & -D_{yzz} \\ 0 & 0 & 0 \end{pmatrix}$	C_2 $\begin{pmatrix} 0 & 0 & 0 \\ D_{xxy} & 0 & D_{xzy} \\ 0 & D_{xyz} & 0 \\ -D_{xxy} & 0 & -D_{xzy} \\ 0 & 0 & 0 \\ D_{yxz} & 0 & D_{yzz} \\ 0 & -D_{xyz} & 0 \\ -D_{yxz} & 0 & -D_{yzz} \\ 0 & 0 & 0 \end{pmatrix}$
C_s $\begin{pmatrix} 0 & 0 & 0 \\ 0 & D_{xyy} & 0 \\ D_{xxz} & 0 & D_{xzz} \\ 0 & -D_{xyy} & 0 \\ 0 & 0 & 0 \\ 0 & D_{yyz} & 0 \\ -D_{xxz} & 0 & -D_{xzz} \\ 0 & -D_{yyz} & 0 \\ 0 & 0 & 0 \end{pmatrix}$	D_2 $\begin{pmatrix} 0 & 0 & 0 \\ 0 & 0 & D_{xzy} \\ 0 & D_{xyz} & 0 \\ 0 & 0 & -D_{xzy} \\ 0 & 0 & 0 \\ D_{yxz} & 0 & 0 \\ 0 & -D_{xyz} & 0 \\ -D_{yxz} & 0 & 0 \\ 0 & 0 & 0 \end{pmatrix}$	C_{2v} $\begin{pmatrix} 0 & 0 & 0 \\ 0 & 0 & 0 \\ D_{xxz} & 0 & 0 \\ 0 & 0 & 0 \\ 0 & 0 & 0 \\ 0 & D_{yyz} & 0 \\ -D_{xxz} & 0 & 0 \\ 0 & -D_{yyz} & 0 \\ 0 & 0 & 0 \end{pmatrix}$

C_4, C_3, C_6	S_4	D_4, D_6
$\begin{pmatrix} 0 & 0 & 0 \\ 0 & 0 & D_{xzy} \\ D_{xxz} & D_{xyz} & 0 \\ 0 & 0 & -D_{xzy} \\ 0 & 0 & 0 \\ -D_{xyz} & D_{xxz} & 0 \\ -D_{xxz} & -D_{xyz} & 0 \\ D_{xyz} & -D_{xxz} & 0 \\ 0 & 0 & 0 \end{pmatrix}$	$\begin{pmatrix} 0 & 0 & 0 \\ 0 & 0 & 0 \\ D_{xxz} & D_{xyz} & 0 \\ 0 & 0 & 0 \\ 0 & 0 & 0 \\ D_{xyz} & -D_{xxz} & 0 \\ -D_{xxz} & -D_{xyz} & 0 \\ -D_{xyz} & D_{xxz} & 0 \\ 0 & 0 & 0 \end{pmatrix}$	$\begin{pmatrix} 0 & 0 & 0 \\ 0 & 0 & D_{xzy} \\ 0 & D_{xyz} & 0 \\ 0 & 0 & -D_{xzy} \\ 0 & 0 & 0 \\ -D_{xyz} & 0 & 0 \\ 0 & -D_{xyz} & 0 \\ D_{xyz} & 0 & 0 \\ 0 & 0 & 0 \end{pmatrix}$
$C_{4v}, D_3, C_{3v}, C_{6v}$	D_{2d}	T, O
$\begin{pmatrix} 0 & 0 & 0 \\ 0 & 0 & 0 \\ D_{xxz} & 0 & 0 \\ 0 & 0 & 0 \\ 0 & 0 & 0 \\ 0 & D_{xxz} & 0 \\ -D_{xxz} & 0 & 0 \\ 0 & -D_{xxz} & 0 \\ 0 & 0 & 0 \end{pmatrix}$	$\begin{pmatrix} 0 & 0 & 0 \\ 0 & 0 & 0 \\ 0 & D_{xyz} & 0 \\ 0 & 0 & 0 \\ 0 & 0 & 0 \\ D_{xyz} & 0 & 0 \\ 0 & -D_{xyz} & 0 \\ -D_{xyz} & 0 & 0 \\ 0 & 0 & 0 \end{pmatrix}$	$\begin{pmatrix} 0 & 0 & 0 \\ 0 & 0 & -D_{xyz} \\ 0 & D_{xyz} & 0 \\ 0 & 0 & D_{xyz} \\ 0 & 0 & 0 \\ -D_{xyz} & 0 & 0 \\ 0 & -D_{xyz} & 0 \\ D_{xyz} & 0 & 0 \\ 0 & 0 & 0 \end{pmatrix}$

Bibliography

[1] DeepL, "Deepl," 2020.

[2] F. Stockwell, *A History of Information Storage and Retrieval*. USA: McFarland, 2001.

[3] M. Hilbert and P. López, "The world's technological capacity to store, communicate, and compute information," *Science*, vol. 332, no. 6025, pp. 60–65, 2011.

[4] M. M. Vopson, "The world's data explained: how much we're producing and where it's all stored," 2021.

[5] A. Holst, "Amount of data created, consumed, and stored 2010-2025," 2021.

[6] IDC, "Idc's global datasphere forecast shows continued steady growth in the creation and consumption of data," 2020.

[7] K. Bhageshpur, "Data is the new oil – and that's a good thing," 2019.

[8] Wikipedia, "Apple M1 Pro and M1 Max — Wikipedia, the free encyclopedia," 2021.

[9] TSMC, "5nm technology," 2020.

[10] S. Davis, "Update: Tsmc's 5nm cmos technology platform," 2020.

[11] X. Lin, W. Yang, K. L. Wang, and W. Zhao, "Two-dimensional spintronics for low-power electronics," *Nature Electronics*, vol. 2, pp. 274–283, 2019.

[12] V. K. Joshi, "Spintronics: A contemporary review of emerging electronics devices," *Engineering Science and Technology, an International Journal*, vol. 19, 2016.

[13] M. M. Waldrop, "The chips are down for moore's law," *Nature*, vol. 530, 2016.

[14] N. X. Elegant, "The internet cloud has a dirty secret," 2019.

[15] A. Andrae, "Total consumer power consumption forecast," 2017.

[16] A. Andrae, "New perspectives on internet electricity use in 2030," *Engineering and Applied Science Letters*, vol. 3, pp. 19–31, 2020.

[17] P. Barla, V. K. Joshi, and S. Bhat, "Spintronic devices: a promising alternative to cmos devices," *Journal of Computational Electronics*, vol. 20, 2021.

[18] J. Puebla, J. Kim, K. Kondou, and Y. Otani, "Spintronic devices for energy-efficient data storage and energy harvesting," *Communications Materials*, vol. 1, 2020.

[19] E. Y. Vedmedenko, R. K. Kawakami, D. D. Sheka, P. Gambardella, A. Kirilyuk, A. Hirohata, C. Binek, O. Chubykalo-Fesenko, S. Sanvito, B. J. Kirby, J. Grollier, K. Everschor-Sitte, T. Kampfrath, C.-Y. You, and A. Berger, "The 2020 magnetism roadmap," *Journal of Physics D: Applied Physics*, vol. 53, p. 453001, 2020.

[20] V. K. Joshi, P. Barla, S. Bhat, and B. K. Kaushik, "From mtj device to hybrid cmos/mtj circuits: A review," *IEEE Access*, vol. 8, pp. 194105–194146, 2020.

[21] M. N. Francis, "The electrical conductivity of transition metals," *Proceedings of the Royal Society of London. Series A - Mathematical and Physical Sciences*, vol. 153, 1936.

[22] P. M. Tedrow and R. Meservey, "Spin-dependent tunneling into ferromagnetic nickel," *Physical Review Letters*, vol. 26, 1971.

[23] P. M. Tedrow and R. Meservey, "Spin polarization of electrons tunneling from films of Fe, Co, Ni, and Gd," *Physical Review B*, vol. 7, 1973.

[24] M. N. Baibich, J. M. Broto, A. Fert, F. N. Van Dau, F. Petroff, P. Etienne, G. Creuzet, A. Friederich, and J. Chazelas, "Giant magnetoresistance of (001)Fe/(001)Cr magnetic superlattices," *Physical Review Letters*, vol. 61, pp. 2472–2475, 1988.

[25] G. Binasch, P. Grünberg, F. Saurenbach, and W. Zinn, "Enhanced magnetoresistance in layered magnetic structures with antiferromagnetic interlayer exchange," *Physical Review B*, vol. 39, pp. 4828–4830, 1989.

[26] G. Brumfiel, "The physics prize inside the ipod," *Nature*, vol. 449, 2007.

[27] A. Fert, "Nobel lecture: Origin, development, and future of spintronics nobel lecture: Origin, development, and future of spintronics," *Reviews of Modern Physics*, vol. 80, 2008.

[28] P. A. Grünberg, "Nobel lecture: From spin waves to giant magnetoresistance and beyond: The 2007 nobel prize for physics was shared by albert fert and peter grünberg. this paper is the text of the address given in conjunction with the award," *Reviews of Modern Physics*, vol. 80, 2008.

[29] S. S. P. Parkin, N. More, and K. P. Roche, "Oscillations in exchange coupling and magnetoresistance in metallic superlattice structures: Co/Ru, Co/Cr, and Fe/Cr," *Physical Review Letters*, vol. 64, pp. 2304–2307, 1990.

[30] S. S. P. Parkin, R. Bhadra, and K. P. Roche, "Oscillatory magnetic exchange coupling through thin copper layers," *Physical Review Letters*, vol. 66, pp. 2152–2155, 1991.

[31] M. Julliere, "Tunneling between ferromagnetic films," *Physics Letters A*, vol. 54, 1975.

[32] J. S. Moodera, L. R. Kinder, T. M. Wong, and R. Meservey, "Large magnetoresistance at room temperature in ferromagnetic thin film tunnel junctions," *Physical Review Letters*, vol. 74, pp. 3273–3276, 1995.

[33] T. Miyazaki and N. Tezuka, "Giant magnetic tunneling effect in Fe/Al_2O_3/Fe junction," *Journal of Magnetism and Magnetic Materials*, vol. 139, 1995.

[34] I. Coorporation, "The application of spintronics," 2012.

[35] S. Mao, Y. Chen, F. Liu, X. Chen, B. Xu, P. Lu, M. Patwari, H. Xi, C. Chang, B. Miller, D. Menard, B. Pant, J. Loven, K. Duxstad, S. Li, Z. Zhang, A. Johnston, R. Lamberton, M. Gubbins, T. McLaughlin, J. Gadbois, J. Ding, B. Cross, S. Xue, and P. Ryan, "Commercial tmr heads for hard disk drives: characterization and extendibility at 300 $gbit^2$," *IEEE Transactions on Magnetics*, vol. 42, pp. 97–102, 2006.

[36] S. Mao, J. J. Nowak, E. S. Linville, H.-S. S. Chen, and S. S. Xue, "TMR head structure with conductive shunt," 2006.

[37] S. S. P. Parkin, "Shiftable magnetic shift register other publications and method of using the same," 2004.

[38] M. Hayashi, L. Thomas, R. Moriya, C. Rettner, and S. S. Parkin, "Current-controlled magnetic domain-wall nanowire shift register," *Science*, vol. 320, 2008.

[39] S. S. Parkin, M. Hayashi, and L. Thomas, "Magnetic domain-wall racetrack memory," *Science*, vol. 320, 2008.

[40] S. Mühlbauer, B. Binz, F. Jonietz, C. Pfleiderer, A. Rosch, A. Neubauer, R. Georgii, and P. Böni, "Skyrmion lattice in a chiral magnet," *Science*, vol. 323, no. 5916, pp. 915–919, 2009.

[41] A. Bogdanov and D. A. Yablonskii, "Thermodynamically stable "vortices" in magnetically ordered crystals. the mixed state of magnets," *Zh. Eksp. Teor. Fiz.*, vol. 95, pp. 178–182, 1989.

[42] A. Bogdanov and A. Hubert, "Thermodynamically stable magnetic vortex states in magnetic crystals," *Journal of Magnetism and Magnetic Materials*, vol. 138, pp. 255–269, 1994.

[43] Y. Tokunaga, X. Z. Yu, J. S. White, H. M. Rï¿½nnow, D. Morikawa, Y. Taguchi, and Y. Tokura, "A new class of chiral materials hosting magnetic skyrmions beyond room temperature," *Nature Communications*, vol. 6, p. 7638, 2015.

[44] W. Jiang, P. Upadhyaya, W. Zhang, G. Yu, M. B. Jungfleisch, F. Y. Fradin, J. E. Pearson, Y. Tserkovnyak, K. L. Wang, O. Heinonen, S. G. E. te Velthuis, and A. Hoffmann, "Blowing magnetic skyrmion bubbles," *Science*, vol. 349, no. 6245, pp. 283–286, 2015.

[45] S. Woo, K. Litzius, B. Krüger, M.-Y. Im, L. Caretta, K. Richter, M. Mann, A. Krone, R. M. Reeve, M. Weigand, P. Agrawal, I. Lemesh, M.-A. Mawass, P. Fischer, M. Kläui, and G. S. D. Beach, "Observation of room-temperature magnetic skyrmions and their current-driven dynamics in ultrathin metallic ferromagnets," *Nature Materials*, vol. 15, no. 5, pp. 501–506, 2016.

[46] W. Koshibae and N. Nagaosa, "Theory of antiskyrmions in magnets," *Nature Communications*, vol. 7, 2016.

[47] A. K. Nayak, V. Kumar, T. Ma, P. Werner, E. Pippel, R. Sahoo, F. Damay, U. K. Rößler, C. Felser, and S. S. Parkin, "Magnetic antiskyrmions above room temperature in tetragonal heusler materials," *Nature*, vol. 548, 2017.

[48] A. Ross, R. Lebrun, C. Ulloa, D. A. Grave, A. Kay, L. Baldrati, F. Kronast, S. Valencia, A. Rothschild, and M. Kläui, "Structural sensitivity of the spin hall magnetoresistance in antiferromagnetic thin films," *Physical Review B*, vol. 102, p. 94415, 2020.

[49] X. Zhang, Y. Zhou, and M. Ezawa, "Antiferromagnetic skyrmion: Stability, creation and manipulation," *Scientific Reports*, vol. 6, 2016.

[50] H. Velkov, O. Gomonay, M. Beens, G. Schwiete, A. Brataas, J. Sinova, and R. A. Duine, "Phenomenology of current-induced skyrmion motion in antiferromagnets," *New Journal of Physics*, vol. 18, 2016.

[51] T. Dohi, S. DuttaGupta, S. Fukami, and H. Ohno, "Formation and current-induced motion of synthetic antiferromagnetic skyrmion bubbles," *Nature communications*, vol. 10, no. 1, p. 5153, 2019.

[52] X. Z. Yu, Y. Tokunaga, Y. Kaneko, W. Z. Zhang, K. Kimoto, Y. Matsui, Y. Taguchi, and Y. Tokura, "Biskyrmion states and their current-driven motion in a layered manganite," *Nature Communications*, vol. 5, 2014.

[53] L. Peng, Y. Zhang, W. Wang, M. He, L. Li, B. Ding, J. Li, Y. Sun, X. G. Zhang, J. Cai, S. Wang, G. Wu, and B. Shen, "Real-space observation of nonvolatile zero-field biskyrmion lattice generation in mnniga magnet," *Nano Letters*, vol. 17, 2017.

[54] D. Foster, C. Kind, P. J. Ackerman, J. S. B. Tai, M. R. Dennis, and I. I. Smalyukh, "Two-dimensional skyrmion bags in liquid crystals and ferromagnets," *Nature Physics*, vol. 15, 2019.

[55] M. Ezawa, "Compact merons and skyrmions in thin chiral magnetic films," *Physical Review B*, vol. 83, 2011.

[56] F. P. Chmiel, N. W. Price, R. D. Johnson, A. D. Lamirand, J. Schad, G. V. D. Laan, D. T. Harris, J. Irwin, M. S. Rzchowski, C. B. Eom, and P. G. Radaelli, "Observation of magnetic vortex pairs at room temperature in a planar α-Fe_2O_3/Co heterostructure," *Nature Materials*, vol. 17, 2018.

[57] H. Jani, J. C. Lin, J. Chen, J. Harrison, F. Maccherozzi, J. Schad, S. Prakash, C. B. Eom, A. Ariando, T. Venkatesan, and P. G. Radaelli, "Antiferromagnetic half-skyrmions and bimerons at room temperature," *Nature*, vol. 590, 2021.

[58] M. Bhukta, T. Dohi, V. K. Bharadwaj, R. Zarzuela, M.-A. Syskaki, M. Foerster, M. A. Niño, J. Sinova, R. Frömter, and M. Kläui, "Ho-

mochiral antiferromagnetic merons, antimerons and bimerons realized in synthetic antiferromagnets," *arXiv preprint arXiv:2303.14853*, 2023.

[59] G. Chen, A. Mascaraque, A. T. N'Diaye, and A. K. Schmid, "Room temperature skyrmion ground state stabilized through interlayer exchange coupling," *Applied Physics Letters*, vol. 106, 2015.

[60] M. Hervé, B. Dupé, R. Lopes, M. Böttcher, M. D. Martins, T. Balashov, L. Gerhard, J. Sinova, and W. Wulfhekel, "Stabilizing spin spirals and isolated skyrmions at low magnetic field exploiting vanishing magnetic anisotropy," *Nature Communications*, vol. 9, 2018.

[61] F. Jonietz, S. Muhlbauer, C. Pfleiderer, A. Neubauer, W. Munzer, A. Bauer, T. Adams, R. Georgii, P. Boni, R. A. Duine, K. Everschor, M. Garst, and A. Rosch, "Spin Transfer Torques in MnSi at Ultralow Current Densities," *Science*, vol. 330, no. 6011, pp. 1648–1651, 2010.

[62] H. Y. Yuan and X. R. Wang, "Skyrmion creation and manipulation by nano-second current pulses," *Scientific Reports*, vol. 6, 2016.

[63] O. Heinonen, W. Jiang, H. Somaily, S. G. E. te Velthuis, and A. Hoffmann, "Generation of magnetic skyrmion bubbles by inhomogeneous spin Hall currents," *Physical Review B*, vol. 93, no. 9, p. 094407, 2016.

[64] F. Büttner, I. Lemesh, M. Schneider, B. Pfau, C. M. Günther, P. Hessing, J. Geilhufe, L. Caretta, D. Engel, B. Krüger, J. Viefhaus, S. Eisebitt, and G. S. D. Beach, "Field-free deterministic ultrafast creation of magnetic skyrmions by spin–orbit torques," *Nature Nanotechnology*, vol. 12, pp. 1040–1044, 2017.

[65] A. Hrabec, J. Sampaio, M. Belmeguenai, I. Gross, R. Weil, S. M. Chérif, A. Stashkevich, V. Jacques, A. Thiaville, and S. Rohart, "Current-induced skyrmion generation and dynamics in symmetric bilayers," *Nature Communications*, 2017.

[66] K. Everschor-Sitte, M. Sitte, T. Valet, A. Abanov, and J. Sinova, "Skyrmion production on demand by homogeneous DC currents," *New Journal of Physics*, 2017.

[67] W. Legrand, D. Maccariello, N. Reyren, K. Garcia, C. Moutafis, C. Moreau-Luchaire, S. Collin, K. Bouzehouane, V. Cros, and A. Fert, "Room-temperature current-induced generation and motion of sub-100 nm skyrmions," *Nano Letters*, vol. 17, 2017.

[68] M. Stier, W. Häusler, T. Posske, G. Gurski, and M. Thorwart, "Skyrmion–anti-skyrmion pair creation by in-plane currents," *Physical Review Letters*, vol. 118, p. 267203, 2017.

[69] S. Woo, K. M. Song, X. Zhang, M. Ezawa, Y. Zhou, X. Liu, M. Weigand, S. Finizio, J. Raabe, M. C. Park, K. Y. Lee, J. W. Choi, B. C. Min, H. C. Koo, and J. Chang, "Deterministic creation and deletion of a single magnetic skyrmion observed by direct time-resolved x-ray microscopy," *Nature Electronics*, vol. 1, 2018.

[70] A. Fert, V. Cros, and J. Sampaio, "Skyrmions on the track," *Nature Nanotechnology*, vol. 8, no. 3, pp. 152–156, 2013.

[71] J. Iwasaki, M. Mochizuki, and N. Nagaosa, "Universal current-velocity relation of skyrmion motion in chiral magnets," *Nature Communications*, vol. 4, p. 1463, 2013.

[72] X. Zhang, G. P. Zhao, H. Fangohr, J. P. Liu, W. X. Xia, J. Xia, and F. J. Morvan, "Skyrmion-skyrmion and skyrmion-edge repulsions in skyrmion-based racetrack memory," *Scientific Reports*, vol. 5, 2015.

[73] K. Litzius, I. Lemesh, B. Krüger, P. Bassirian, L. Caretta, K. Richter, F. Büttner, K. Sato, O. A. Tretiakov, J. Förster, R. M. Reeve, M. Weigand, I. Bykova, H. Stoll, G. Schütz, G. S. D. Beach, and M. Kläui, "Skyrmion hall effect revealed by direct time-resolved x-ray microscopy," *Nature Physics*, vol. 13, pp. 170–175, 2017.

[74] R. Tomasello, E. Martinez, R. Zivieri, L. Torres, M. Carpentieri, and G. Finocchio, "A strategy for the design of skyrmion racetrack memories," *Scientific Reports*, vol. 4, no. 1, p. 6784, 2015.

[75] J. Müller, "Magnetic skyrmions on a two-lane racetrack," *New Journal of Physics*, vol. 19, p. 025002, 2017.

[76] G. Yu, P. Upadhyaya, Q. Shao, H. Wu, G. Yin, X. Li, C. He, W. Jiang, X. Han, P. K. Amiri, and K. L. Wang, "Room-Temperature Skyrmion Shift Device for Memory Application," *Nano Letters*, vol. 17, no. 1, pp. 261–268, 2017.

[77] W. Jiang, X. Zhang, G. Yu, W. Zhang, X. Wang, M. Benjamin Jungfleisch, J. E. Pearson, X. Cheng, O. Heinonen, K. L. Wang, Y. Zhou, A. Hoffmann, and S. G. E. te Velthuis, "Direct observation of the skyrmion Hall effect," *Nature Physics*, vol. 13, no. 2, pp. 162–169, 2017.

[78] T. Yokouchi, N. Kanazawa, A. Tsukazaki, Y. Kozuka, A. Kikkawa, Y. Taguchi, M. Kawasaki, M. Ichikawa, F. Kagawa, and Y. Tokura, "Formation of in-plane skyrmions in epitaxial MnSi thin films as revealed by planar hall effect," *Journal of the Physical Society of Japan*, vol. 84, 2015.

[79] S. A. Meynell, M. N. Wilson, K. L. Krycka, B. J. Kirby, H. Fritzsche, and T. L. Monchesky, "Neutron study of in-plane skyrmions in MnSi thin films," *Physical Review B*, vol. 96, 2017.

[80] B. Göbel, A. Mook, J. Henk, I. Mertig, and O. A. Tretiakov, "Magnetic bimerons as skyrmion analogues in in-plane magnets," *Physical Review B*, vol. 99, 2019.

[81] T. Dohi, R. M. Reeve, and M. Kläui, "Thin film skyrmionics," *Annual Review of Condensed Matter Physics*, vol. 13, pp. 73–95, 2022.

[82] R. Zarzuela, V. K. Bharadwaj, K.-W. Kim, J. Sinova, and K. Everschor-Sitte, "Stability and dynamics of in-plane skyrmions in collinear ferromagnets," *Physical Review B*, vol. 101, no. 5, p. 054405, 2020.

[83] A. Soumyanarayanan, N. Reyren, A. Fert, and C. Panagopoulos, "Emergent phenomena induced by spin-orbit coupling at surfaces and interfaces," *Nature*, vol. 539, 2016.

[84] I. Dzyaloshinsky, "A thermodynamic theory of "weak" ferromagnetism of antiferromagnetics," *Journal of Physics and Chemistry of Solids*, vol. 4, pp. 241–255, 1958.

[85] T. Moriya, "Anisotropic superexchange interaction and weak ferromagnetism," *Physical Review*, vol. 120, pp. 91–98, 1960.

[86] T. Moriya, "New mechanism of anisotropic superexchange interaction," *Physical Review Letters*, vol. 4, 1960.

[87] X. Z. Yu, Y. Onose, N. Kanazawa, J. H. Park, J. H. Han, Y. Matsui, N. Nagaosa, and Y. Tokura, "Real-space observation of a two-dimensional skyrmion crystal," *Nature*, vol. 465, 2010.

[88] X. Z. Yu, N. Kanazawa, Y. Onose, K. Kimoto, W. Z. Zhang, S. Ishiwata, Y. Matsui, and Y. Tokura, "Near room-temperature formation of a skyrmion crystal in thin-films of the helimagnet FeGe," *Nature Materials*, vol. 10, 2011.

[89] A. Crépieux and C. Lacroix, "Dzyaloshinsky-moriya interactions induced by symmetry breaking at a surface," *Journal of Magnetism and Magnetic Materials*, vol. 182, 1998.

[90] M. Bode, M. Heide, K. V. Bergmann, P. Ferriani, S. Heinze, G. Bihlmayer, A. Kubetzka, O. Pietzsch, S. Blügel, and R. Wiesendanger, "Chiral magnetic order at surfaces driven by inversion asymmetry," *Nature*, vol. 447, 2007.

[91] A. N. Bogdanov and U. K. Rößler, "Chiral symmetry breaking in magnetic thin films and multilayers," *Physical Review Letters*, vol. 87, p. 037203, 2001.

[92] U. K. Rößler, A. N. Bogdanov, and C. Pfleiderer, "Spontaneous skyrmion ground states in magnetic metals," *Nature*, vol. 442, pp. 797–801, 2006.

[93] S. Rohart and A. Thiaville, "Skyrmion confinement in ultrathin film nanostructures in the presence of dzyaloshinskii-moriya interaction," *Physical Review B*, vol. 88, p. 184422, 2013.

[94] I. E. Dzyaloshinskii, "Theory of helicoidal structures in antiferromagnets. i. nonmetals," *Soviet Physics JETP*, vol. 19, p. 960, 1964.

[95] A. N. Bogdanov, U. K. Rößler, M. Wolf, and K. H. Müller, "Magnetic structures and reorientation transitions in noncentrosymmetric uniaxial antiferromagnets," *Physical Review B*, vol. 66, 2002.

[96] L. D. Landau and E. M. Lifshitz, *Course of theoretical physics. Vol. 5: Statistical physics*, vol. 6. 1968.

[97] S. V. Grigoriev, N. M. Potapova, S.-A. Siegfried, V. A. Dyadkin, E. V. Moskvin, V. Dmitriev, D. Menzel, C. D. Dewhurst, D. Chernyshov, R. A. Sadykov, L. N. Fomicheva, and A. V. Tsvyashchenko, "Chiral properties of structure and magnetism in $Mn_{1-x}Fe_xGe$ compounds: When the left and the right are fighting, who wins?," *Physical Review Letters*, vol. 110, p. 207201, 2013.

[98] S. Heinze, K. V. Bergmann, M. Menzel, J. Brede, A. Kubetzka, R. Wiesendanger, G. Bihlmayer, and S. Blügel, "Spontaneous atomic-scale magnetic skyrmion lattice in two dimensions," *Nature Physics*, vol. 7, 2011.

[99] S. Emori, U. Bauer, S. M. Ahn, E. Martinez, and G. S. Beach, "Current-driven dynamics of chiral ferromagnetic domain walls," *Nature Materials*, vol. 12, 2013.

[100] D. Khadka, S. Karayev, and S. X. Huang, "Dzyaloshinskii-moriya interaction in Pt/Co/Ir and Pt/Co/Ru multilayer films," *Journal of Applied Physics*, vol. 123, 2018.

[101] H. Yang, O. Boulle, V. Cros, A. Fert, and M. Chshiev, "Controlling dzyaloshinskii-moriya interaction via chirality dependent atomic-layer stacking, insulator capping and electric field," *Scientific Reports*, vol. 8, 2018.

[102] G. M. Wysin, "Demagnetization effects in thin magnets," 2015.

[103] A. Hubert and R. Schäfer, *Magnetic Domains:The Analysis of Magnetic Microstructures*. Springer Berlin, 1998.

[104] J. M. Coey, *Magnetism and magnetic materials*. Cambridge University Press, 2010.

[105] T. Koyama, D. Chiba, K. Ueda, K. Kondou, H. Tanigawa, S. Fukami, T. Suzuki, N. Ohshima, N. Ishiwata, Y. Nakatani, K. Kobayashi, and T. Ono, "Observation of the intrinsic pinning of a magnetic domain wall in a ferromagnetic nanowire," *Nature Materials*, vol. 10, 2011.

[106] M. D. Dejong and K. L. Livesey, "Analytic theory for the switch from bloch to Néel domain wall in nanowires with perpendicular anisotropy," *Physical Review B*, vol. 92, 2015.

[107] A. Thiaville, S. Rohart, Émilie Jué, V. Cros, and A. Fert, "Dynamics of dzyaloshinskii domain walls in ultrathin magnetic films," *Europhysics Letters*, vol. 100, 2012.

[108] M. Heide, G. Bihlmayer, and S. Blügel, "Dzyaloshinskii-moriya interaction accounting for the orientation of magnetic domains in ultrathin films: Fe/W$(_{110})$," *Physical Review B*, vol. 78, 2008.

[109] E. Lifshitz and L. Landau, "On the theory of dispersion of magnetic permeabilty in ferromagnetic bodies," *Physikalische Zeitschrift der Sowjetunion*, vol. 8, pp. 153–169, 1935.

[110] T. L. Gilbert, "A phenomenological theory of damping in ferromagnetic materials," *IEEE Transactions on Magnetics*, vol. 40, 2004.

[111] "MicroMagnum simulation package. http://micromagnum.informatik.uni-hamburg.de (2013) ."

[112] A. Vansteenkiste, J. Leliaert, M. Dvornik, M. Helsen, F. Garcia-Sanchez, and B. Van Waeyenberge, "The design and verification of MuMax3," *AIP Advances*, vol. 4, no. 10, p. 107133, 2014.

[113] M. J. Donahue and D. G. Porter, "Oommf: Object oriented micromagnetic framework. https://nanohub.org/resources/oommf," 2016.

[114] A. Brataas, A. D. Kent, and H. Ohno, "Current-induced torques in magnetic materials," *Nature Materials*, vol. 11, pp. 372–381, 2012.

[115] K. Everschor-Sitte, J. Masell, R. M. Reeve, and M. Kläui, "Perspective: Magnetic skyrmions—overview of recent progress in an active research field," *Journal of Applied Physics*, vol. 124, no. 24, p. 240901, 2018.

[116] L. Berger, "Emission of spin waves by a magnetic multilayer traversed by a current," *Physical Review B*, vol. 54, no. 13, pp. 9353–9358, 1996.

[117] J. Slonczewski, "Current-driven excitation of magnetic multilayers," *Journal of Magnetism and Magnetic Materials*, vol. 159, no. 1-2, pp. L1–L7, 1996.

[118] D. C. Ralph and M. D. Stiles, "Spin transfer torques," *Journal of Magnetism and Magnetic Materials*, vol. 320, pp. 1190–1216, 2008. Introduction to SST.

[119] A. D. Kent and D. C. Worledge, "A new spin on magnetic memories," *Nature Nanotechnology*, vol. 10, 2015.

[120] A. Kalitsov, M. Chshiev, I. Theodonis, N. Kioussis, and W. H. Butler, "Spin-transfer torque in magnetic tunnel junctions," *Physical Review B*, vol. 79, 2009.

[121] H. Kubota, A. Fukushima, K. Yakushiji, T. Nagahama, S. Yuasa, K. Ando, H. Maehara, Y. Nagamine, K. Tsunekawa, D. D. Djayaprawira, N. Watanabe, and Y. Suzuki, "Quantitative measurement of voltage dependence of spin-transfer torque in MgO-based magnetic tunnel junctions," *Nature Physics*, vol. 4, 2008.

[122] A. Thiaville, Y. Nakatani, J. Miltat, and Y. Suzuki, "Micromagnetic understanding of current-driven domain wall motion in patterned nanowires," *Europhysics Letters*, vol. 69, 2005.

[123] A. Yamaguchi, T. Ono, S. Nasu, K. Miyake, K. Mibu, and T. Shinjo, "Real-space observation of current-driven domain wall motion in submicron magnetic wires," *Physical Review Letters*, vol. 92, 2004.

[124] G. Tatara and H. Kohno, "Theory of current-driven domain wall motion: Spin transfer versus momentum transfer," *Physical Review Letters*, vol. 92, 2004.

[125] N. Vernier, D. A. Allwood, D. Atkinson, M. D. Cooke, and R. P. Cowburn, "Domain wall propagation in magnetic nanowires by spin-polarized current injection," *Europhysics Letters*, vol. 65, 2004.

[126] M. Kläui, C. A. Vaz, J. A. Bland, W. Wernsdorfer, G. Faini, E. Cambril, and L. J. Heyderman, "Domain wall motion induced by spin polarized currents in ferromagnetic ring structures," *Applied Physics Letters*, vol. 83, 2003.

[127] J. Grollier, P. Boulenc, V. Cros, A. Hamzić, A. Vaurès, A. Fert, and G. Faini, "Switching a spin valve back and forth by current-induced domain wall motion," *Applied Physics Letters*, vol. 83, 2003.

[128] S. Zhang and Z. Li, "Roles of Nonequilibrium Conduction Electrons on the Magnetization Dynamics of Ferromagnets," *Physical Review Letters*, vol. 93, no. 12, p. 127204, 2004.

[129] P. Gambardella and I. M. Miron, "Current-induced spin–orbit torques," *Philosophical Transactions of the Royal Society A: Mathematical, Physical and Engineering Sciences*, vol. 369, no. 1948, pp. 3175–3197, 2011.

[130] J. Sinova, S. O. Valenzuela, J. Wunderlich, C. Back, and T. Jungwirth, "Spin hall effects," *Reviews of Modern Physics*, vol. 87, pp. 1213–1260, 2015.

[131] J. Sinova and T. Jungwirth, "Surprises from the spin Hall effect," *Physics Today*, vol. 70, no. 7, pp. 38–42, 2017.

[132] A. Manchon, J. Železný, I. M. Miron, T. Jungwirth, J. Sinova, A. Thiaville, K. Garello, and P. Gambardella, "Current-induced spin-orbit torques in ferromagnetic and antiferromagnetic systems," *Reviews of Modern Physics*, vol. 91, no. 3, p. 035004, 2019.

[133] A. V. Khvalkovskiy, V. Cros, D. Apalkov, V. Nikitin, M. Krounbi, K. A. Zvezdin, A. Anane, J. Grollier, and A. Fert, "Matching domain-wall configuration and spin-orbit torques for efficient domain-wall motion," *Physical Review B*, vol. 87, no. 2, p. 020402, 2013.

[134] J. Sampaio, V. Cros, S. Rohart, A. Thiaville, and A. Fert, "Nucleation, stability and current-induced motion of isolated magnetic skyrmions in nanostructures," *Nature Nanotechnology*, vol. 8, no. 11, pp. 839–844, 2013.

[135] "A non-linear field theory," *Proceedings of the Royal Society of London. Series A. Mathematical and Physical Sciences*, vol. 260, 1961.

[136] T. H. Skyrme, "A unified field theory of mesons and baryons," *Nuclear Physics*, vol. 31, 1962.

[137] A. N. Bogdanov, U. K. Rößler, and A. A. Shestakov, "Skyrmions in nematic liquid crystals," *Physical Review E - Statistical Physics, Plasmas, Fluids, and Related Interdisciplinary Topics*, vol. 67, 2003.

[138] J. I. Fukuda and S. Žumer, "Quasi-two-dimensional skyrmion lattices in a chiral nematic liquid crystal," *Nature Communications*, vol. 2, 2011.

[139] U. A. Khawaja and H. Stoof, "Skyrmions in a ferromagnetic bose - einstein condensate," *Nature*, vol. 411, 2001.

[140] T. L. Ho, "Spinor bose condensates in optical traps," *Physical Review Letters*, vol. 81, 1998.

[141] J. H. Han, "Skyrmions in spinor bose-einstein condensates," 2017.

[142] S. L. Sondhi, A. Karlhede, S. A. Kivelson, and E. H. Rezayi, "Skyrmions and the crossover from the integer to fractional quantum hall effect at small zeeman energies," *Physical Review B*, vol. 47, 1993.

[143] S. E. Barrett, G. Dabbagh, L. N. Pfeiffer, K. W. West, and R. Tycko, "Optically pumped nmr evidence for finite-size skyrmions in gaas quantum wells near landau level filling ν=1," *Physical Review Letters*, vol. 74, 1995.

[144] Y. Tokura and N. Kanazawa, "Magnetic skyrmion materials," *Chemical Reviews*, vol. 121, 2021.

[145] N. Nagaosa and Y. Tokura, "Topological properties and dynamics of magnetic skyrmions," *Nature Nanotechnology*, vol. 8, 2013.

[146] A. Neubauer, C. Pfleiderer, B. Binz, A. Rosch, R. Ritz, P. G. Niklowitz, and P. Böni, "Topological hall effect in the a phase of MnSi," *Physical Review Letters*, vol. 102, 2009.

[147] W. Münzer, A. Neubauer, T. Adams, S. Mühlbauer, C. Franz, F. Jonietz, R. Georgii, P. Böni, B. Pedersen, M. Schmidt, A. Rosch, and C. Pfleiderer, "Skyrmion lattice in the doped semiconductor $Fe_{1-x}Co_xSi$," *Physical Review B*, vol. 81, 2010.

[148] T. Adams, S. Mühlbauer, A. Neubauer, W. Münzer, F. Jonietz, R. Georgii, B. Pedersen, P. Böni, A. Rosch, and C. Pfleiderer, "Skyrmion lattice domains in $Fe_{1-x}Co_xSi$," *Journal of Physics: Conference Series*, vol. 200, p. 032001, 2010.

[149] S. Seki, X. Z. Yu, S. Ishiwata, and Y. Tokura, "Observation of skyrmions in a multiferroic material," *Science*, vol. 336, 2012.

[150] S. X. Huang and C. L. Chien, "Extended skyrmion phase in epitaxial FeGe(111) thin films," *Physical Review Letters*, vol. 108, 2012.

[151] Y. Okamura, F. Kagawa, S. Seki, and Y. Tokura, "Transition to and from the skyrmion lattice phase by electric fields in a magnetoelectric compound," *Nature Communications*, vol. 7, 2016.

[152] S. L. Zhang, A. Bauer, D. M. Burn, P. Milde, E. Neuber, L. M. Eng, H. Berger, C. Pfleiderer, G. V. D. Laan, and T. Hesjedal, "Multidomain skyrmion lattice state in Cu_2OSeO_3," *Nano Letters*, vol. 16, 2016.

[153] N. Romming, C. Hanneken, M. Menzel, J. E. Bickel, B. Wolter, K. von Bergmann, A. Kubetzka, and R. Wiesendanger, "Writing and Deleting Single Magnetic Skyrmions," *Science*, vol. 341, no. 6146, pp. 636–639, 2013.

[154] O. Boulle, J. Vogel, H. Yang, S. Pizzini, D. de Souza Chaves, A. Locatelli, T. O. Menteş, A. Sala, L. D. Buda-Prejbeanu, O. Klein, M. Belmeguenai, Y. Roussigné, A. Stashkevich, S. M. Chérif, L. Aballe, M. Foerster,

M. Chshiev, S. Auffret, I. M. Miron, and G. Gaudin, "Room-temperature chiral magnetic skyrmions in ultrathin magnetic nanostructures," *Nature Nanotechnology*, vol. 11, no. 5, pp. 449–454, 2016.

[155] O. Boulle, G. Malinowski, and M. Kläui, "Current-induced domain wall motion in nanoscale ferromagnetic elements," *Materials Science and Engineering: R: Reports*, vol. 72, pp. 159–187, 2011.

[156] K. Everschor, M. Garst, R. A. Duine, and A. Rosch, "Current-induced rotational torques in the skyrmion lattice phase of chiral magnets," *Physical Review B*, vol. 84, no. 6, p. 064401, 2011.

[157] K. Everschor, *Current-induced dynamics of chiral magnetic structures*. PhD thesis, 2012.

[158] Y. Liu, H. Yan, M. Jia, H. Du, and A. Du, "Topological analysis of spin-torque driven magnetic skyrmion formation," *Applied Physics Letters*, vol. 109, no. 10, p. 102402, 2016.

[159] X. Z. Yu, W. Koshibae, Y. Tokunaga, K. Shibata, Y. Taguchi, N. Nagaosa, and Y. Tokura, "Transformation between meron and skyrmion topological spin textures in a chiral magnet," *Nature*, vol. 564, 2018.

[160] N. Gao, S. G. Je, M. Y. Im, J. W. Choi, M. Yang, Q. Li, T. Y. Wang, S. Lee, H. S. Han, K. S. Lee, W. Chao, C. Hwang, J. Li, and Z. Q. Qiu, "Creation and annihilation of topological meron pairs in in-plane magnetized films," *Nature Communications*, vol. 10, 2019.

[161] X. Li, L. Shen, Y. Bai, J. Wang, X. Zhang, J. Xia, M. Ezawa, O. A. Tretiakov, X. Xu, M. Mruczkiewicz, M. Krawczyk, Y. Xu, R. F. Evans, R. W. Chantrell, and Y. Zhou, "Bimeron clusters in chiral antiferromagnets," *npj Computational Materials*, vol. 6, 2020.

[162] Y. A. Kharkov, O. P. Sushkov, and M. Mostovoy, "Bound states of skyrmions and merons near the lifshitz point," *Physical Review Letters*, vol. 119, 2017.

[163] X. Zhang, J. Xia, L. Shen, M. Ezawa, O. A. Tretiakov, G. Zhao, X. Liu, and Y. Zhou, "Static and dynamic properties of bimerons in a frustrated ferromagnetic monolayer," *Physical Review B*, vol. 101, 2020.

[164] G. Chen, S. P. Kang, C. Ophus, A. T. N'Diaye, H. Y. Kwon, R. T. Qiu, C. Won, K. Liu, Y. Wu, and A. K. Schmid, "Out-of-plane chiral domain wall spin-structures in ultrathin in-plane magnets," *Nature Communications*, vol. 8, 2017.

[165] V. P. Kravchuk, D. D. Sheka, U. K. Rößler, J. Van Den Brink, and Y. Gaididei, "Spin eigenmodes of magnetic skyrmions and the problem of the effective skyrmion mass," *Physical Review B*, vol. 97, no. 6, p. 064403, 2018.

[166] L. Landau and E. Lifshitz, *Electrodynamics of Continuous Media, Course of Theoretical Physics*, vol. 8. Pergamon, 1984.

[167] R. C. Powell, *Symmetry, Group Theory, and the Physical Properties of Crystals*, vol. 824 of *Lecture Notes in Physics*. New York, NY: Springer New York, 2010.

[168] A. Jain, S. P. Ong, G. Hautier, W. Chen, W. D. Richards, S. Dacek, S. Cholia, D. Gunter, D. Skinner, G. Ceder, and K. a. Persson, "The Materials Project: A materials genome approach to accelerating materials innovation," *APL Materials*, vol. 1, no. 1, p. 011002, 2013.

[169] *Pearson's handbook of crystallographic data for intermetallic phases*, vol. 3. ASM International, Materials Park, OH,, 1996.

[170] "$Rb_6[Fe_2O_5]$ ($Rb_6Fe_2O_5$) crystal structure: Datasheet from pauling file multinaries edition 2012 in springermaterials."

[171] A. O. Leonov, T. L. Monchesky, N. Romming, A. Kubetzka, A. N. Bogdanov, and R. Wiesendanger, "The properties of isolated chiral skyrmions in thin magnetic films," *New Journal of Physics*, vol. 18, p. 065003, 2016.

[172] F. Büttner, I. Lemesh, and G. S. D. Beach, "Theory of isolated magnetic skyrmions: From fundamentals to room temperature applications," *Scientific Reports*, vol. 8, p. 4464, 2018.

[173] V. Flovik, A. Qaiumzadeh, A. K. Nandy, C. Heo, and T. Rasing, "Generation of single skyrmions by picosecond magnetic field pulses," *Physical Review B*, vol. 96, no. 14, p. 140411, 2017.

[174] N. Vidal-Silva, A. Riveros, F. Tejo, J. Escrig, and D. Altbir, "Controlling the nucleation and annihilation of skyrmions with magnetostatic interactions," *Applied Physics Letters*, vol. 115, p. 082405, 2019.

[175] L. Peng, R. Takagi, W. Koshibae, K. Shibata, K. Nakajima, T. hisa Arima, N. Nagaosa, S. Seki, X. Yu, and Y. Tokura, "Controlled transformation of skyrmions and antiskyrmions in a non-centrosymmetric magnet," *Nature Nanotechnology*, vol. 15, pp. 181–186, 2020.

[176] I. Lemesh, K. Litzius, M. Böttcher, P. Bassirian, N. Kerber, D. Heinze, J. Zázvorka, F. Büttner, L. Caretta, M. Mann, M. Weigand, S. Finizio, J. Raabe, M.-Y. Im, H. Stoll, G. Schütz, B. Dupé, M. Kläui, and G. S. D. Beach, "Magnetic Skyrmions: Current-Induced Skyrmion Generation through Morphological Thermal Transitions in Chiral Ferromagnetic Heterostructures ," *Advanced Materials*, vol. 30, no. 49, p. 1870372, 2018.

[177] Y. Zhou and M. Ezawa, "A reversible conversion between a skyrmion and a domain-wall pair in a junction geometry," *Nature Communications*, vol. 5, no. 1, p. 4652, 2014.

[178] G. Berruto, I. Madan, Y. Murooka, G. M. Vanacore, E. Pomarico, J. Rajeswari, R. Lamb, P. Huang, A. J. Kruchkov, Y. Togawa, T. LaGrange, D. McGrouther, H. M. Rønnow, and F. Carbone, "Laser-Induced Skyrmion Writing and Erasing in an Ultrafast Cryo-Lorentz Transmission Electron Microscope," *Physical Review Letters*, vol. 120, no. 11, p. 117201, 2018.

[179] O. P. Polyakov, I. A. Gonoskov, V. S. Stepanyuk, and E. K. U. Gross, "Generation of magnetic skyrmions by focused vortex laser pulses," *Journal of Applied Physics*, vol. 127, no. 7, p. 073904, 2020.

[180] S.-G. Je, P. Vallobra, T. Srivastava, J.-C. Rojas-Sánchez, T. H. Pham, M. Hehn, G. Malinowski, C. Baraduc, S. Auffret, G. Gaudin, S. Mangin, H. Béa, and O. Boulle, "Creation of Magnetic Skyrmion Bubble Lattices by Ultrafast Laser in Ultrathin Films," *Nano Letters*, vol. 18, no. 11, pp. 7362–7371, 2018.

[181] X. Zhang, Y. Zhou, K. Mee Song, T.-E. Park, J. Xia, M. Ezawa, X. Liu, W. Zhao, G. Zhao, and S. Woo, "Skyrmion-electronics: writing, deleting, reading and processing magnetic skyrmions toward spintronic applications," *Journal of Physics: Condensed Matter*, vol. 32, no. 14, p. 143001, 2020.

[182] C. Back, V. Cros, H. Ebert, K. Everschor-Sitte, A. Fert, M. Garst, T. Ma, S. Mankovsky, T. L. Monchesky, M. Mostovoy, N. Nagaosa, S. S. P. Parkin, C. Pfleiderer, N. Reyren, A. Rosch, Y. Taguchi, Y. Tokura, K. von Bergmann, and J. Zang, "The 2020 skyrmionics roadmap," *Journal of Physics D: Applied Physics*, vol. 53, no. 36, p. 363001, 2020.

[183] S.-Z. Lin, "Edge instability in a chiral stripe domain under an electric current and skyrmion generation," *Physical Review B*, vol. 94, no. 2, p. 020402, 2016.

[184] B. Krüger, *Current-Driven Magnetization Dynamics: Analytical Modeling and Numerical Simulation*. PhD thesis, Universität Hamburg, 2011.

[185] M. Sitte, K. Everschor-Sitte, T. Valet, D. R. Rodrigues, J. Sinova, and A. Abanov, "Current-driven periodic domain wall creation in ferromagnetic nanowires," *Physical Review B*, vol. 94, p. 064422, 2016.

[186] F. Büttner, I. Lemesh, M. Schneider, B. Pfau, C. M. Günther, P. Hessing, J. Geilhufe, L. Caretta, D. Engel, B. Krüger, J. Viefhaus, S. Eisebitt, and G. S. D. Beach, "Field-free deterministic ultrafast creation of magnetic skyrmions by spin–orbit torques," *Nature Nanotechnology*, vol. 12, pp. 1040–1044, 2017.

[187] K. Everschor, M. Garst, B. Binz, F. Jonietz, S. Mühlbauer, C. Pfleiderer, and A. Rosch, "Rotating skyrmion lattices by spin torques and field or temperature gradients," *Physical Review B*, vol. 86, no. 5, p. 054432, 2012.

[188] S. Komineas and N. Papanicolaou, "Skyrmion dynamics in chiral ferromagnets," *Physical Review B*, vol. 92, p. 064412, 2015.

[189] T. Schulz, R. Ritz, A. Bauer, M. Halder, M. Wagner, C. Franz, C. Pfleiderer, K. Everschor, M. Garst, and A. Rosch, "Emergent electrodynamics of skyrmions in a chiral magnet," *Nature Physics*, vol. 8, no. 4, pp. 301–304, 2012.

[190] K. Litzius, J. Leliaert, P. Bassirian, D. Rodrigues, S. Kromin, I. Lemesh, J. Zazvorka, K.-J. Lee, J. Mulkers, N. Kerber, *et al.*, "The role of temperature and drive current in skyrmion dynamics," *Nature Electronics*, vol. 3, no. 1, pp. 30–36, 2020.

[191] A. A. Thiele, "Steady-State Motion of Magnetic Domains," *Physical Review Letters*, vol. 30, no. 6, pp. 230–233, 1973.

[192] S. Komineas and N. Papanicolaou, "Skyrmion dynamics in chiral ferromagnets under spin-transfer torque," *Physical Review B*, vol. 92, p. 174405, 2015.

[193] U. Ritzmann, S. von Malottki, J.-V. Kim, S. Heinze, J. Sinova, and B. Dupé, "Trochoidal motion and pair generation in skyrmion and antiskyrmion dynamics under spin–orbit torques," *Nature Electronics*, vol. 1, no. 8, pp. 451–457, 2018.

[194] N. Romming, A. Kubetzka, C. Hanneken, K. V. Bergmann, and R. Wiesendanger, "Field-dependent size and shape of single magnetic skyrmions," *Physical Review Letters*, vol. 114, p. 177203, 2015.

List of Figures

List of Tables